THE UNIVERSITY OF QUEENSLAND

AUSTRALIA

A novel magnetic resonance technique to characterise grey matter microstructure in the human brain

Shahrzad Moinian

M.Sc. in Computer Science, B.Sc. in Computer Engineering

A thesis submitted for the degree of Doctor of Philosophy at

The University of Queensland in 2019

Queensland Brain Institute & Centre for Advanced Imaging

Abstract

Accurate characterisation of the microstructure of the human cerebral cortex is important for a number of applications. It guides anatomical parcellation, the functional correlates of which inform neurosurgical decision making. It also enables detection of subtle abnormalities such as focal cortical dysplasia (FCD), an important cause of epilepsy. Many studies have been conducted in this area over the past century using different techniques ranging from qualitative histological to quantitative *in vivo* Magnetic Resonance (MR) studies. However, achievement of precise whole-cortex microanatomical mapping has been hindered by the lack of a comprehensive mapping method that takes into account a wide range of microstructural (cytoarchitectonic and myeloarchitectonic) tissue properties.

To bridge this gap, I conducted my research with two main aims. First, I investigated the presence of information in the Magnetic Resonance Imaging (MRI) signal about tissue microstructure over and above MR relaxometry-based tissue properties (e.g. longitudinal relaxation time T1, effective transverse relaxation time $T2^*$), on which MR-based microstructural mapping methods are based. I proposed a novel quantitative framework that employs Magnetic Resonance Fingerprinting (MRF) and statistically characterises the MRF residuals, after accounting for the relaxometry-based tissue properties. I showed the presence of area-specific characteristics in the MRF residual signals from three cortical areas of individuals, suggesting that the framework could reveal more information about the microstructural variations between cortical areas. This method could especially be helpful where the information derived from the MR-relaxometry tissue properties is not sufficient for delineating the distinction between two cortical areas.

The second aim of my research was to propose an automated microanatomical mapping method for parcellating the cortex at the voxel level. I used the MRF residual analysis framework to characterise voxels from seven cortical areas. I then developed a feature-based supervised machine learning classification model that takes the statistical characterisation of each voxel MRF residual as its input feature vector. At the level of the individual subject, the average parcellation accuracy of the model was >80% for seven cortical areas. The proposed quantitative *in vivo* voxel-wise cortical parcellation method could be further expanded to cover the whole brain. The framework might also be used for purposes other than cortical parcellation, including accurate lesion detection and delineation in neurosurgery and staging of neurological diseases.

Declaration by author

This thesis is composed of my original work, and contains no material previously published or written by another person except where due reference has been made in the text. I have clearly stated the contribution by others to jointly-authored works that I have included in my thesis.

I have clearly stated the contribution of others to my thesis as a whole, including statistical assistance, survey design, data analysis, significant technical procedures, professional editorial advice, financial support and any other original research work used or reported in my thesis. The content of my thesis is the result of work I have carried out since the commencement of my higher degree by research candidature and does not include a substantial part of work that has been submitted to qualify for the award of any other degree or diploma in any university or other tertiary institution. I have clearly stated which parts of my thesis, if any, have been submitted to qualify for another award.

I acknowledge that an electronic copy of my thesis must be lodged with the University Library and, subject to the policy and procedures of The University of Queensland, the thesis be made available for research and study in accordance with the Copyright Act 1968 unless a period of embargo has been approved by the Dean of the Graduate School.

I acknowledge that copyright of all material contained in my thesis resides with the copyright holder(s) of that material. Where appropriate I have obtained copyright permission from the copyright holder to reproduce material in this thesis and have sought permission from co-authors for any jointly authored works included in the thesis.

Publications included in this thesis

Conference abstract

Shahrzad Moeiniyan Bagheri, Viktor Vegh, David Reutens, “Towards in-vivo voxel-wise parcellation of human brain cortex”. *International Society for Magnetic Resonance in Medicine (ISMRM)*, Montreal, Canada, 2019. (Incorporated as Appendix A)

Submitted manuscripts included in this thesis

Shahrzad Moinian, Viktor Vegh, Kieran O'Brien, David Reutens, “Human grey matter characterisation based on MR fingerprinting residual signals”. Submitted to *Neuroimage*. (Incorporated as Chapter 2)

Conference abstract

Shahrzad Moinian, Viktor Vegh, David Reutens, “In vivo voxel-wise parcellation of the human cerebral cortex using 3D MR fingerprinting (MRF) and supervised machine learning classification”. Submitted to *International Society for Magnetic Resonance in Medicine (ISMRM)*. (Incorporated as Chapter 4)

Other publications during candidature

Conference abstract

Shahrzad Moeiniyan Bagheri, Viktor Vegh, David Reutens, “Magnetic Resonance Fingerprinting (MRF) can reveal microstructural variations in the brain gray matter”. *International Society for Magnetic Resonance in Medicine (ISMRM)*, Paris, France, 2018.

Symposium

Shahrzad Moeiniyan Bagheri, Viktor Vegh, David Reutens, “Magnetic Resonance Fingerprinting and characterization of tissue microstructure in the human brain”. *The Centre for Advanced Imaging 4th annual Symposium*, Brisbane, Australia, 2017.

Contributions by others to the thesis

Prof David Reutens and A/Prof Viktor Vegh have made significant contributions to the conception and design of the project, validation of the results, and writing the conference abstracts and the manuscripts.

Chapter 2: Dr Kieran O'Brien contributed to the development and testing of the MRI sequence used in this chapter. He also contributed to the revision of the manuscript.

Chapter 3: Prof Markus Barth contributed to the development of the MRI sequence used in this chapter.

Ms Nicole Atcheson contributed to MRI data acquisition throughout this thesis.

Statement of parts of the thesis submitted to qualify for the award of another degree

No works submitted towards another degree have been included in this thesis.

Research Involving Human or Animal Subjects

The University of Queensland human ethics committee granted ethical approval for the studies performed in this thesis. Ethics approval number: 2005000502.

The ethics approval letter is provided in Appendix B.

Acknowledgements

I would like to express deepest gratitude to my supervisors Prof David Reutens and A/Prof Viktor Vegh for their constructive support and guidance throughout this journey. Thank you for trusting my abilities and make me realise what is it about science that I truly enjoy.

I have been fortunate to have worked with great collaborators and colleagues. I would like to thank Ms Nicole Atcheson, Mr Aiman Al Najjar and Ms Sarah Daniel for providing assistance with data collection, Dr Kieran O'Brien and Prof Markus Barth for the help with MRF sequence development and Dr Daniel Stäb for help with testing the MRF sequence on the scanner. I would also like to thank my fellow Reutens group members. Special thanks to Dr Steffen Bollmann and Mr Javier Urriola for the valuable discussions and help with learning new tools for data analysis.

I wish to thank my PhD thesis committee, Prof Markus Barth and A/Prof Kai-Hsiang Chuang, for their invaluable comments. A special thanks to Dr Lorine Wilkinson for her support during my PhD candidature and Mrs Lesley Green for organising meetings.

I am grateful to my husband and my parents for their love, support and encouragement. Thank you for your trust and belief in me.

Financial support

This research was supported by 1) The University of Queensland International Scholarship (UQI), and 2) Funding from Australian Research Council: ARC Discovery Project. DP140103593

Keywords

MRI, MR fingerprinting, human cortical parcellation, tissue microstructure, machine learning

Australian and New Zealand Standard Research Classifications (ANZSRC)

ANZSRC code: 110903, Central Nervous System, 60%

ANZSRC code: 029901, Biological Physics, 30%

ANZSRC code: 080109, Pattern Recognition and Data Mining, 10%

Fields of Research (FoR) Classification

FoR code: 1109, Neurosciences , 60%

FoR code: 0299, Other Physical Sciences, 30%

FoR code: 0801, Artificial Intelligence and Image Processing, 10%

Table of Contents

List of Figures

List of Tables

List of Abbreviations

2D	Two dimensional
3D	Three dimensional
7T	7.0 Tesla
AD	Alzheimer’s disease
AUC	Area under the curve
BA	Brodmann areas
BET	Brain extraction tool
bSSFP	Balanced steady state free precession
CSF	Cerebrospinal fluid
dMRI	Diffusion MRI
DOF	Degrees of freedom
DTI	Diffusion tensor imaging
EPG	Extended phase graphs
EPI	Echo-planar imaging
FA	Flip angle
FCD	Focal cortical dysplasia
FISP	Fast imaging with steady-state precession
FLIRT	FMRIB's linear image registration tool
fMRI	Functional MRI
FMRIB	Functional Magnetic Resonance Imaging of the Brain
FNIRT	FMRIB's nonlinear image registration tool
FSL	FMRIB software library
GLI	Gray level index
GM	Gray matter
GRAPPA	Generalized autocalibrating partially parallel acquisitions
KNN	K-nearest neighbours
L-SVM	Linear support vector machine
ML	Machine learning
MP2RAGE	Magnetization-prepared 2 rapid acquisition gradient echoes
MRF	Magnetic resonance fingerprinting
MRI	Magnetic resonance imaging
MT	Magnetisation transfer
MWF	Myelin water fraction
PD	Proton density
QSM	Quantitative susceptibility mapping
RBF-SVM	Radial basis function support vector machine
RF	Radio frequency
ROC	Receiver operating characteristic curve
ROI	Region-of-interest
SA2RAGE	Saturation-prepared with 2 rapid gradient echoes
SAR	Specific absorption rate
SNR	Signal-to-noise ratio
SPM	Statistical parametric mapping
SVM	Support vector machine
TE	Echo time
TR	Repetition time
WM	White matter

Chapter 1 Introduction

Early studies of the human cerebral cortex microanatomy, through invasive histological methods, have revealed the spatial heterogeneity of this important part of the brain [1]. Accordingly, human cortical parcellation, which aims to develop methods for identifying these distinct partitions of the cortex, has played an important role in understanding the organisation of the brain. Such studies have the potential to improve our understanding of i) the underlying microstructural characteristics of the brain functional units [2, 3], and ii) the microstructural pathology of different types of psychiatric and neurological disorders such as epilepsy, Alzheimer's disease (AD), focal cortical dysplasia (FCD), and multiple sclerosis (MS) [4-7].

The field of human cortical mapping has gone through major developments since the initial studies that were started at the beginning of the 19th century. Particularly, the advent of Magnetic Resonance Imaging (MRI) has revolutionised this field, as it allows non-invasive studies of the brain organisation in the living human brain [8].

In this dissertation, I present the findings of my PhD research, in which I investigated the development of a novel magnetic resonance technique to characterise grey matter microstructure in the human brain.

In this introductory chapter, I present a background to the field of human cortical mapping, starting by an overview of two main microstructural characterisation criteria (i.e. cyto- and myelo-architectonics). I then briefly describe the first observer-independent method of cortical characterisation [9], which was a major revolutionary transition from qualitative to quantitative methods towards reliable and reproducible cortical parcellation. Next, an overview of the MRI basics is provided, followed by the discussion of the major advances in quantitative MRI-based cortical mapping methods and their limitations that motivated the research presented in this thesis. Finally, a novel Magnetic Resonance (MR)-based tissue property quantification framework (i.e. Magnetic Resonance Fingerprinting (MRF) [10]) is described, and its capacity for resolving the major drawbacks of previous quantitative MRI cortical mapping methods is explained. Here, I explain why MRF was selected as the main component of the cortical characterisation research presented in this thesis.

At the end of this introductory chapter, three main aims of my PhD research are outlined. The findings from the investigation of each aim are presented in the following chapters.

1.1 HISTOLOGICAL CORTICAL MAPPING

Efforts in microarchitectonic mapping of the human cerebral cortex began over a century ago, using histological studies of post-mortem brains. These studies were mainly based on cytoarchitectonic and myeloarchitectonic features, taking into account the layered organisation (usually six layers) of the cortex and the unique characteristics of different cortical areas [11].

1.1.1 Cytoarchitectonics

In cytoarchitectonic mapping, the cerebral cortex is subdivided into distinct areas based on differences in the thickness of the cortex and its individual layers and the density, distribution, size and shape of neuronal cell bodies in each layer of the cortex [12]. As an example, Figure 1-1 illustrates the distinction in layered cytoarchitecture of primary motor cortex and occipital cortex in the human. Note the absence of layer *IV* (i.e. internal granular layer [11]) and the presence of giant pyramidal cells (Betz cells) in layer *V* of the primary motor cortex [13]. In the occipital cortex, the arrangement of small and large pyramidal cells in layer *III* (i.e. external pyramidal layer [11]) allows the subdivision of this layer into two sublayers (*IIIa* and *IIIb*) [14].

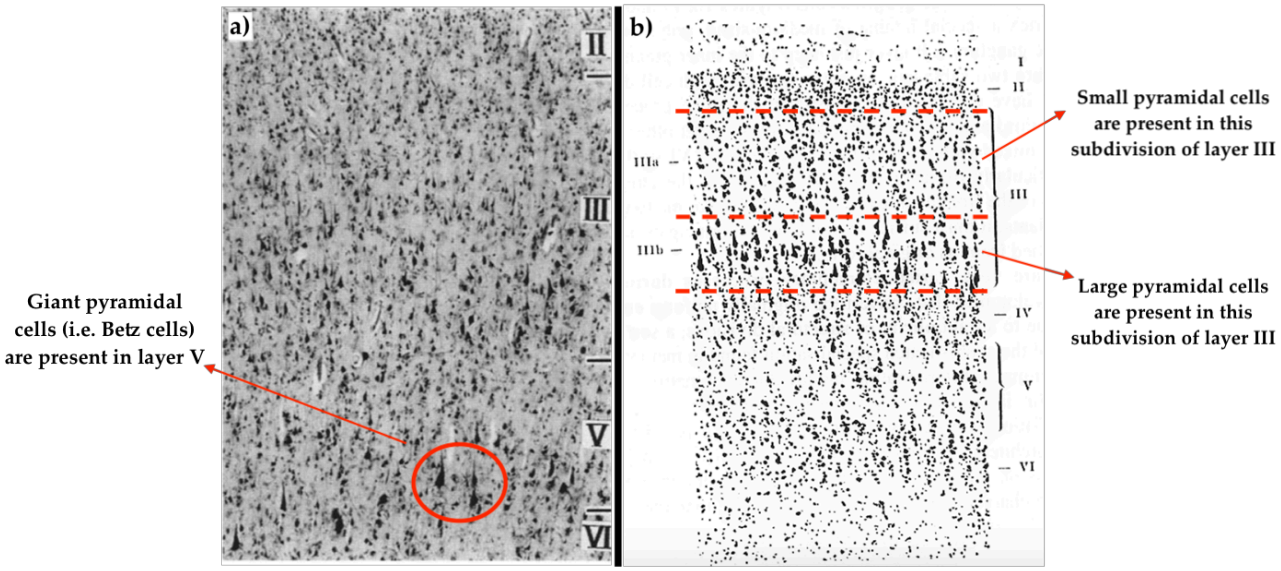

Figure 1-1 The cytoarchitecture of a) primary motor cortex (Source: [13]), and b) occipital cortex (Source: [14]) in adult human.

Brodmann [15], who was one of the pioneers of microanatomical cortical mapping, identified 52 cytoarchitectonically distinct subdivisions in the human cerebral cortex and published his cytoarchitectonic map of the human brain in 1909. Figure 1-2 depicts five other

cytoarchitectonic maps of the human cerebral cortex that have been published over the first half of the twentieth century. A comparison of these cortical maps reveals differences in terms of the number and boundary of identified cytoarchitectural subdivisions. For example, von Economo and Koskinas [16] supplemented Brodmann areas 44, 45, and 47 [15] by transitional areas $F_{F\Phi}$, F_F, and $F_{f\alpha}$ in the fronto-orbital cortex. Following the new ontology that they introduced, von Economo's and Koskinas' map [16] contains more cortical areas than Brodmann's cytoarchitectonic map [15]. Considerable differences are also observed between Brodmann's map and the Russian school's (Sarkisov, et al. [17]) map of the human cerebral cortex, although the latter employed Brodmann's cytoarchitectonic mapping approach as the basis for their studies. In later studies, Bailey [18] concluded that cytoarchitectonic characteristics are insufficient to differentiate between all areas of the cerebral cortex. They also argued that the Brodmann cortical mapping approach would lead to over-parcellation of the cerebral cortex and pointed out the observer-dependent cytoarchitectonic criteria used in the Brodmann parcellation scheme as one of the main problems of his cortical parcellation method. This in turn leads to non-reproducibility and subjectivity, which could explain the parcellation variations in the cytoarchitectonic maps of the cerebral cortex published by different researchers (Figure 1-2) [1]. Further, Lashley and Clark [19] argued that the limited number of brains studied by Brodmann and the followers of his approach could give rise to the problem of variability between different cortical maps.

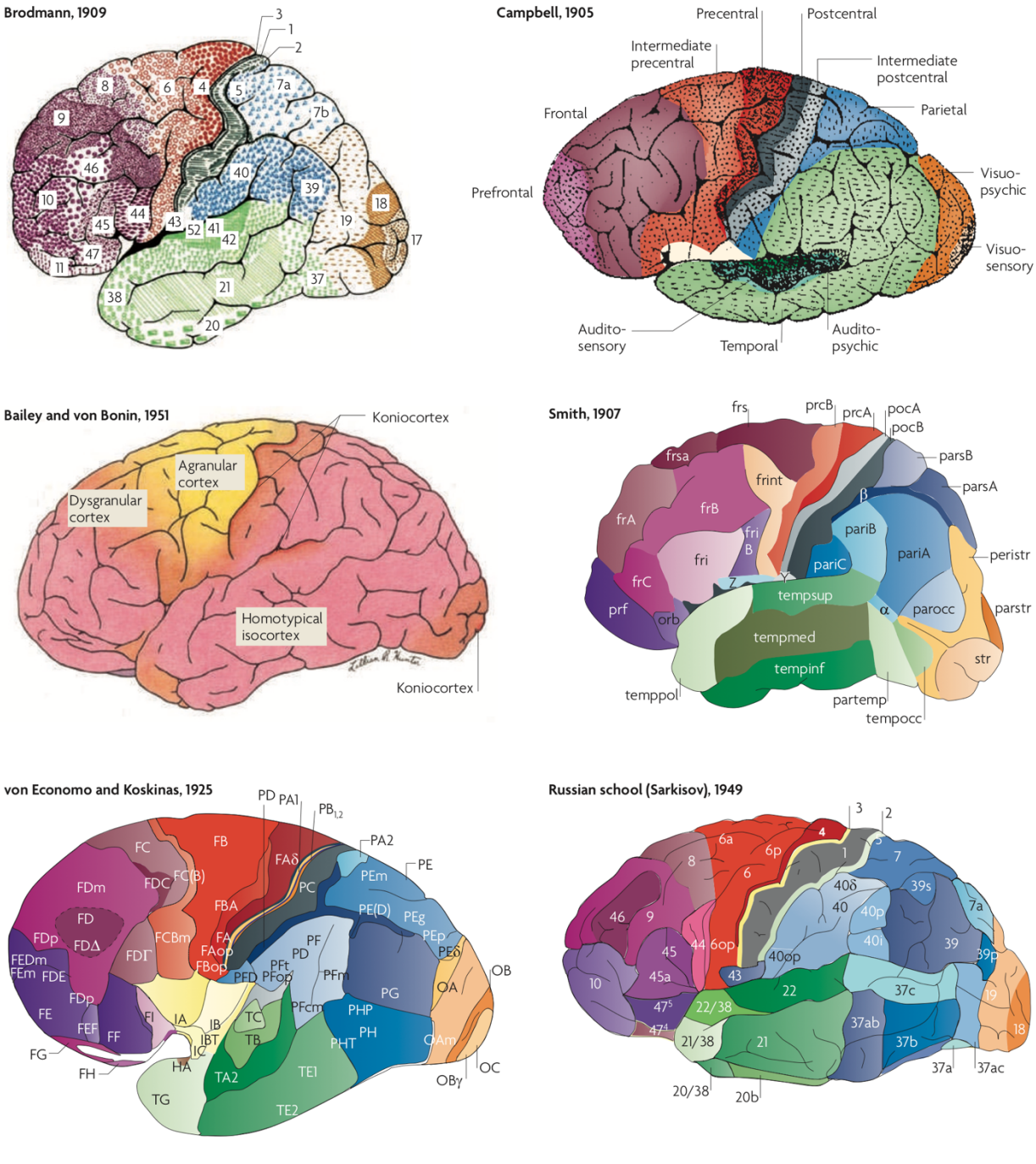

Figure 1-2 Cytoarchitectonic maps of the human cerebral cortex published by Brodmann [20], Campbell [21], Bailey [18], Smith [22], von Economo and Koskinas [16], and Sarkisov, et al. [17]. Similar colours represent similar cytoarchitectonic structures. Source: [1].

1.1.2 Myeloarchitectonics

Myeloarchitectonic mapping studies the differences in size, density, orientation relative to the cortical surface (tangentially, radially or obliquely oriented) of myelinated nerve fibres, organised in distinctive layers across the cerebral cortex [12]. Vogt and Vogt [23] initiated the studies of myeloarchitectural mapping of the cerebral cortex in 1898 by establishing one

of the largest research institutes in Germany, located in Berlin and focussing on the study of cerebral cortex structure and function [11].

The Vogts' work on myeloarchitectonic and functional parcellation of the cerebral cortex [24] inspired Brodmann's cytoarchitectural mapping studies [1] which were performed in collaboration with the Vogts. Unlike cytoarchitectonic studies, which were also performed by external researchers, the majority of the myeloarchitectonic studies of the human cerebral cortex were conducted in Vogts' institute [11]. The Vogts established a simple, well-designed systematic approach for preparing sections of the brain using Weigert staining of the sections and for analysing the myeloarchitecture of the cerebral cortex [11].

Vogt [25] defined two main criteria for analysing the myeloarchitectonic characteristics of the cerebral cortex based on the laminar arrangement of i) the tangential fibre bands (i.e. bistriate, unistriate, unitostriate, and astriate [11]), and ii) the radial fibre bundles (i.e. euradiate, supraradiate and infraradiate [11]), as depicted in Figure 1.3. Local variations in these myeloarchitectural characteristics between the neighbouring areas of the cerebral cortex defined areal boundaries. In terms of the architectural variations of the tangential fibres, in the bistriate type (Figure 1.3a), two clearly distinct tightly packed bands of tangential fibres (i.e. bands of Baillarger) are visible in layers *4* and *5b*. In contrast, in the unistriate type (Figure 1.3b), only the external band of Baillarger is identifiable in layer *4*. The intrastriate layer 5a, which is poor in fibres and thus separates the Baillarger stripes, is not present in the unitostriate type, consequently creating a single plexus (Figure 1.3c). In the astriate type (Figure 1.3d), layers 4-6 are not differentiable and are visible as a large concentrated fibre plexus. With regard to radial fibre bundles, the main discriminator is the length of the fibre bundles. The fibre bundles in the infraradiate type are very short and only reach to the internal stria layer 5b (Figure 1.3b). In contrast, the fibre bundles in the supraradiate type (Figure 1.3c), are very long and extend over the width of the cortex to zonal layer 1. The fibre bundles of the euradiate type (Figure 1.3a and d), are of an intermediate length, relative to the length of the bundles in the supraradiate and infraradiate types.

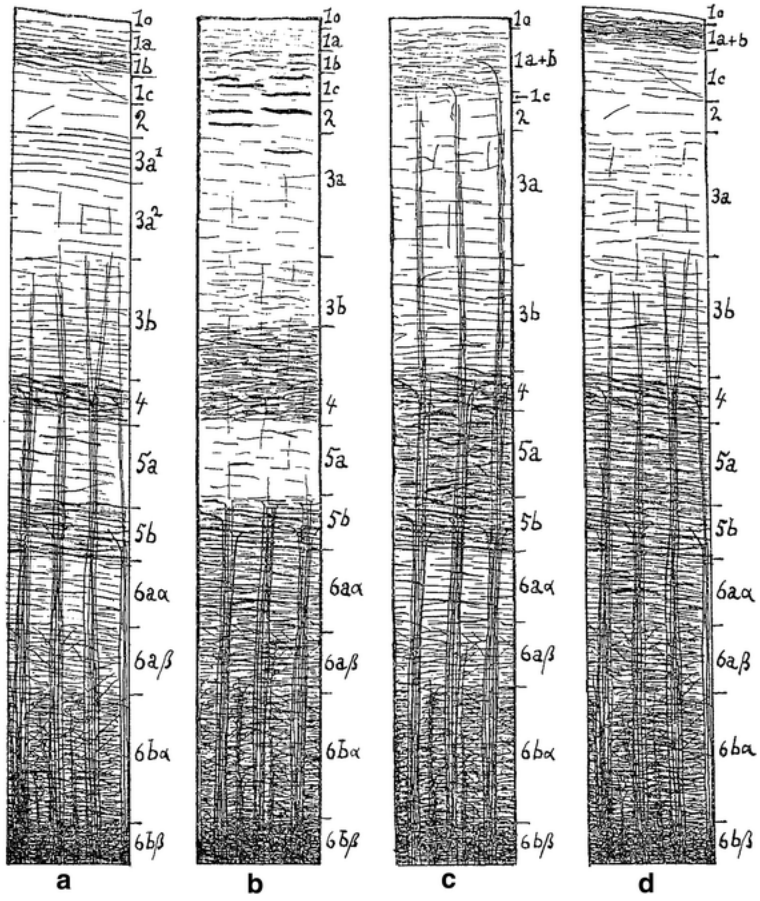

Figure 1.3 Vogt [25] identified four main types of lamination patterns of the tangential fibres: a) bistriate, b) unistriate, c) unitostriate, d) astriate, and three types of the radial fibre bundles arrangements: a,d) euradiate, b) infraradiate, c) supraradiate, in the cerebral cortex. Source: [11].

An example of the use of these criteria by Vogt [26], to make myeloarchitectural distinctions between three frontal areas (i.e. areas 17, 36 and 42) in the human cerebral cortex is illustrated in Figure 1.4. In area 17 the radial fibre bundles end in the intrastriate layer 5a, thus classifying this cortical area as of the infraradiate type. Area 36 is identified as a unistriate euradiate type, and area 42 is of the astriate type because of the densely packed fibres in layers 4-6.

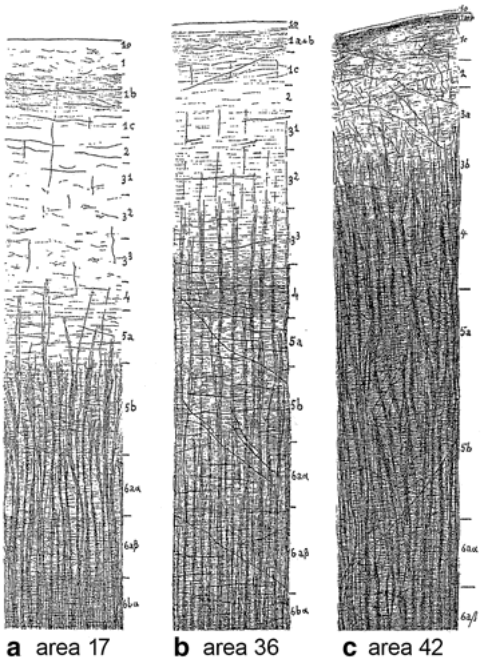

Figure 1.4 Myeloarchitectonic laminar variations between frontal cortical areas a) 17, b) 36, and c) 42, according to Vogt [26]. Source: [11].

The Vogts' myeloarchitectonic map contains a much larger number of microstructurally distinct cortical areas (i.e. 200 [24]) than Brodmann's cytoarchitectonic map [15]. This may be explained by the higher differentiability between the architecture of intracortical nerve fibres, which was considered by Vogts in their parcellation approach, enabling further subdivision of major cortical areas identified by Brodmann [27]. Despite these differences, Vogt and Vogt [23] noted that, similar to the layered arrangement of cytoarchitectural properties, myeloarchitectonic characteristics of the cerebral cortex are also arranged in a layered manner, as demonstrated in Figure 1.5. This suggests complementarity of cytoarchitectonic and myeloarchitectonic information for mapping the cerebral cortex [11]. Accordingly, the Vogts believed that it was possible to develop a multimodal microarchitectonic map of the human cerebral cortex based on the combination of cyto- and myeloarchitectural features [1].

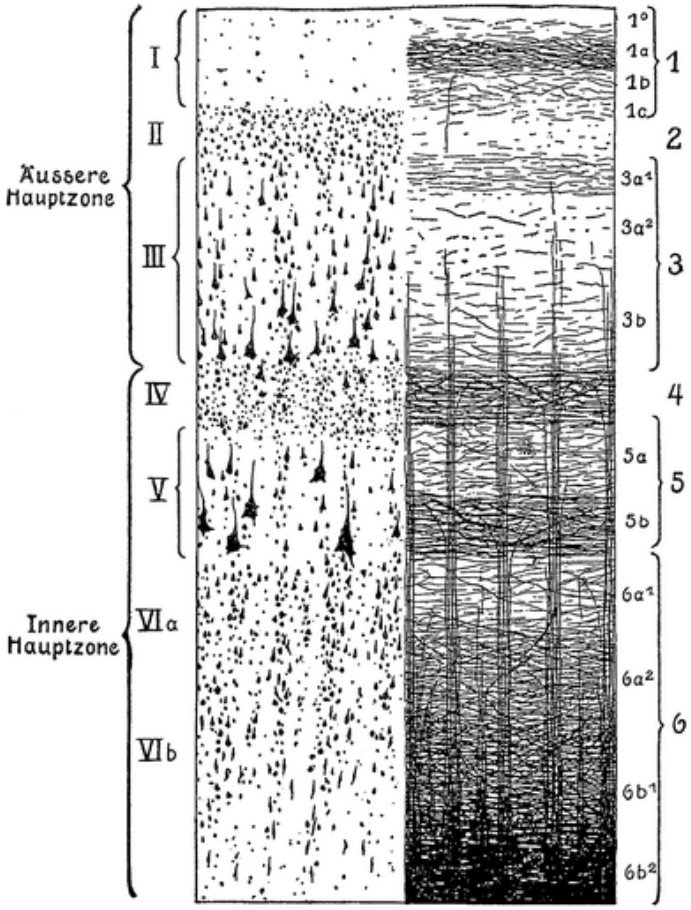

Figure 1.5 A schematic representation of the layered organisation of myeloarchitecture (right) and cytoarchitecture (left) of the cerebral cortex provided by Vogt and Vogt [23]. Source: [11].

Apart from the extensive myeloarchitectonic studies performed at the institute of the Vogts, other pioneering scientists including Campbell [21], Smith [22] and Kaes [28], to name a few, also published myeloarchitectural maps of the human cerebral cortex. Campbell [21] performed his microarchitectural studies with the ultimate aim of localising cerebral cortical functions. He analysed both cyto- and myeloarchitectural characteristics of three human cerebral hemispheres, and then added examinations of only white matter fibres for another three hemispheres to this study. Using this method, he identified 16 cortical areas. At the time (1905), his human cerebral cortex map was the only one describing the combined cyto and myeloarchitectonic features of cortical areas. Another myeloarchitectonic pioneer was Smith [22] who published his myeloarchitectural map of the human cerebral cortex in 1907. He used a simplified technique for his myeloarchitectonic investigations based on macroscopic characterisation of unstained sections of the cerebral cortex. His main parcellation criteria relied on variations in the degree of distinctness and the width of Baillarger stripes. Accordingly, he was able to create a detailed myeloarchitectonic map of the human cerebral cortex, delineating 50 different cortical areas. He strongly disagreed with the common belief that there was gradual change in microstructural features in the transition

from one cortical area to neighbouring areas in the cortex. Accordingly, he believed in the possibility of precise localisation of interareal boundaries. Kaes [28] also performed extensive myeloarchitectural studies between 1891 and 1904, aiming at providing concise myeloarchitectonic descriptions of the human cerebral cortex. To this end, his studies also involved quantitative measurements of myeloarchitectural properties, mainly focusing on the cortical depth and the width of each cortical layer. He published his myeloarchitectonic parcellation in 1907 [28], containing detailed descriptions, measurements and drawings of the myeloarchitectural features of 12 cortical areas of 45 postmortem human brains. However, one major component missing in his publication was the precise location of the cortical areas being investigated [11].

Despite the extensive efforts made by the Vogts to develop a systematic myeloarchitectonic parcellation scheme, and of others to provide detailed and precise description of the myeloarchitectural features, the resultant cortical maps were different in terms of the number and extent of the distinct areas that were identified [11]. This was also the case in the studies conducted by the followers of the Vogts' myeloarchitectonic parcellation scheme, such as Gerhardt [29] and Hopf [30]. Figure 1.6 illustrates the disagreement between the myeloarchitectonic maps produced by Vogt [31], Gerhardt [29] and Hopf [30], in terms of the spatial location of the boundaries between cortical areas [32]. Like the variations observed between different cytoarchitectonic maps (Figure 1-2), these disagreements are mainly due to the observer-dependent myeloarchitectonic mapping criteria used in different parcellation regimes [9, 11].

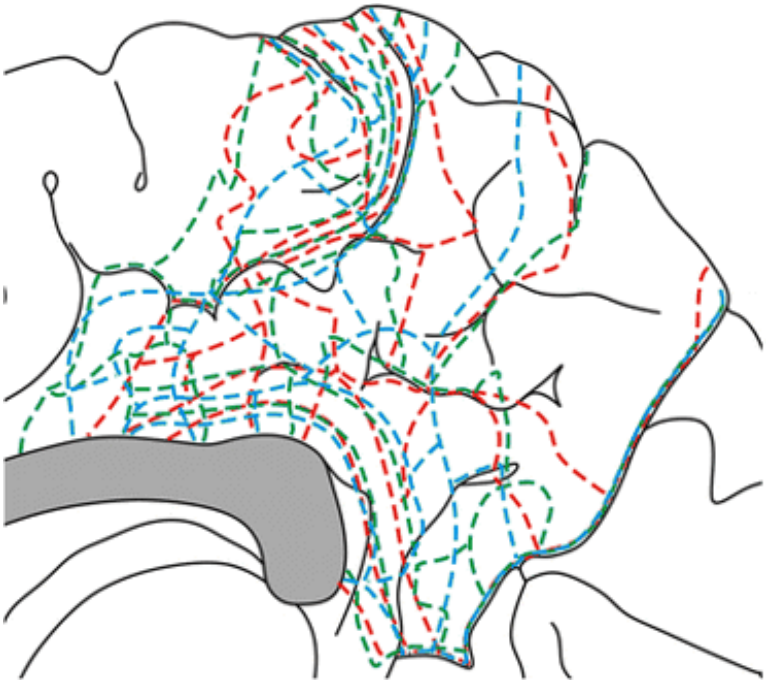

Figure 1.6 The myeloarchitectonic cortical boundaries of Vogt [31] (red dashed lines), Gerhardt [29] (green dashed lines) and Hopf [30] (blue dashed lines) are transformed (using computer-aided tools) to a standard reference brain template and superimposed on the template, showing the disagreement in myeloarchitectonic cortical boundaries between different areas [32]. Source: [32].

1.1.3 Limitations

Despite the extensive cyto- and myeloarchitectonic studies of the cerebral cortex using classical histological methods, several factors hinder their integration into modern neuroimaging applications. First, the described cortical mapping methods are not reproducible due to their observer-dependent qualitative mapping criteria and the absence of detailed parcellation criteria for some regions [9]. Second, the resultant maps did not take into account the inter-individual architectonic variations, because they are based on the study of a limited number of postmortem brains [1]. Third, the conventional histological microarchitectonic maps were in the form of two-dimensional drawings at the time of their publication, posing challenges for integration into modern volumetric neuroimaging data from individuals and for integration of different modalities of microarchitectonic maps (e.g. cyto and myeloarchitectural) into a single comprehensive multi-modal microstructural atlas of the whole cerebral cortex [1]. Although, more recently, Nieuwenhuys, et al. [32], for example, employed computer-aided tools to transform the myeloarchitectonic data available at the Vogts institute to a standard reference brain template, i) the basis of the resultant myeloarchitectonic map was still the qualitative observer-dependent data collected by the Vogts, and ii) the position of the microarchitectonic areas was only approximated through comparison of the macroscopic features of the standard brain template and drawings of the

myeloarchitectonic maps from the Vogts. Consequently, the need for developing quantitative observer-independent methods of microstructural mapping motivated further studies in this regard to solve the mentioned issues.

1.2 OBSERVER-INDEPENDENT HISTOLOGICAL MAPPING

To address the issues of classical histological microstructural mapping methods, Schleicher, et al. [9] developed a quantitative observer-independent microarchitectonic mapping method, using quantitative analysis of cell-body stained histological sections of postmortem brains. They used an automatic procedure to scan the cell-stained histological sections at microscopic spatial resolution of 25 μm, and subsequently created volume cell density profiles (perpendicular to the cortical surface) using gray level index (GLI) measurements along the cerebral cortex. The Mahalanobis distance was then measured between the neighbouring GLI profiles along the cortex, and the distance profiles were obtained accordingly. The positions of significant local maxima on the distance profiles were then identified as the potential locations of boundaries between two adjacent cortical areas. The approach was based on the previous histological findings suggesting that the presence of a unique laminar structure in each cortical area allowed adjacent areas to be distinguished.

Figure 1-7 depicts an overview of the observer-independent microstructural mapping method used in a subsequent study [33] to identify the microarchitectonic borders between the primary somatosensory area (Area 2 in Figure 1.7) and two of its neighbouring areas (i.e. the primary somatosensory (Area 1 in Figure 1.7) and the posterior parietal cortex (PPC)). Significant peak distance values can be identified at profile indices 34 and 75 (Figure 1-7b), delineating the location of the border between area 2 and 1 (indicated by the top arrow in Figure 1-7a,), and between area 2 and PPC (indicated by the bottom arrow in Figure 1-7a,), respectively.

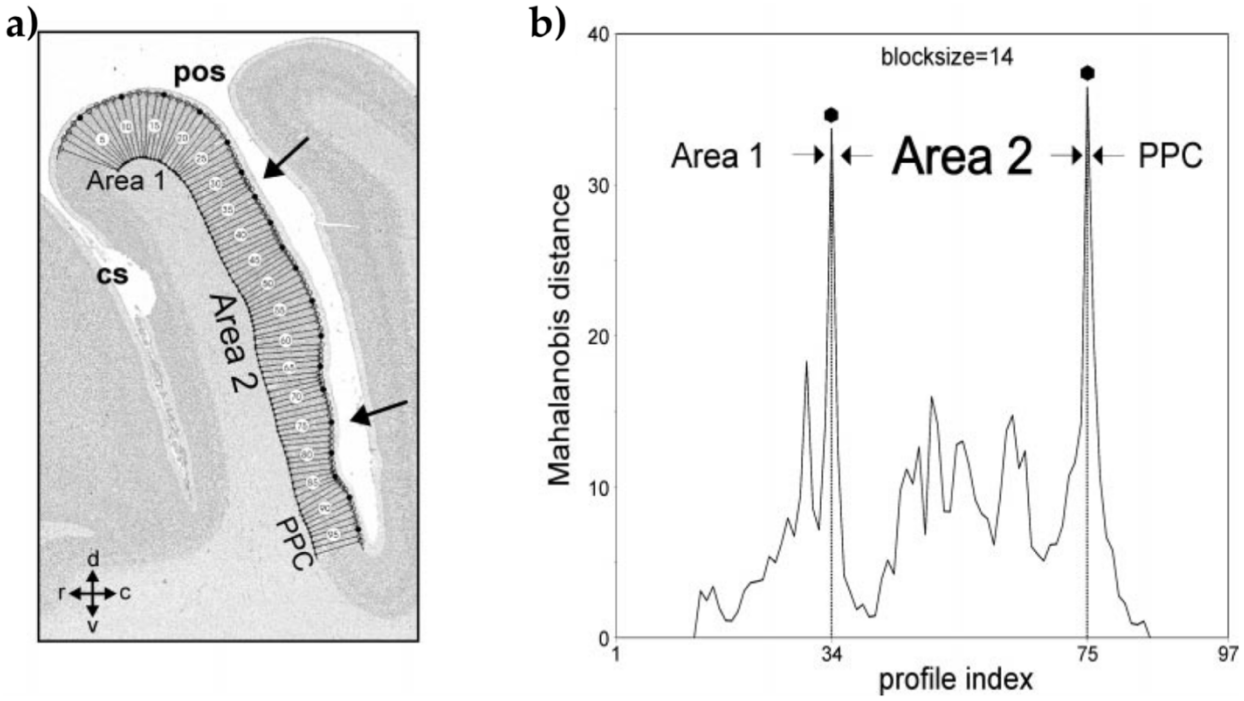

Figure 1-7 An overview of the quantitative observer-independent microarchitectonic mapping method. The GLI profiles were calculated along the cortex (a). The Mahalanobis distance profile was then calculated between the neighbouring GLI profiles, and the boundaries between area 2 and areas 1 and PPC were then identified based on the significant peak values (i.e. at profile index 34 and 75, respectively) on the distance profile (b). The corresponding boundary positions are marked by the black arrows in (a). Source: [33].

This was the first observer-independent study that laid the foundation for reproducibility and improved reliability in cortical parcellation through developing of a systematic quantitative approach [9]. Consequently, many of the above-mentioned problems with the classical histological microarchitectonic mapping methods were resolved [9, 34]. Reproducible and reliable border delineation was not possible using the previous subjective and qualitative methods, thus leading to inconsistency and disagreement between classical microarchitectonic maps in this regard, an example of which is illustrated in Figure 1.6. Furthermore, the use of the Schleicher's method led to reproducible subdivision of some previously defined cortical areas, which was helpful for increasing our understanding of the structure-function association in the cortex. For example, the primary motor cortex area (i.e. Brodmann area 4 [15]) had been unanimously defined as a single homogeneous cytoarchitectonic area in conventional microstructural studies [15]. However, using the Schleicher's observer-independent parcellation technique, Geyer, et al. [35] delineated two reproducible cytoarchitectonic subdivisions within this area (i.e. anterior area 4 and posterior area 4). Figure 1-8b shows the presence of a significant peak distance value at position 6240 μm from the bottom of the sulcus, between the peak values corresponding to the boundary of areas 3a (at position 1190 μm) and 6 (at position 14850 μm). Accordingly,

Geyer, et al. [35] concluded that the peak value at position 6240 μm indicated the presence of the border between two subdivisions of area 4. In this case, the importance of microstructural subdivision of a cortical area could be further realised in regard to the functional segregation of the primary motor cortex, as revealed in the same study by Geyer, et al. [35]. The primary motor area was previously known as a single homogenous functional area, despite some reports of the presence of double representations of arm and hand [36]. However, Geyer, et al. [35], showed that, for example, one representation of the fingers was in area 4a and the other representation was in area 4p. They also demonstrated that roughness discrimination activated area 4p, but not area 4a.

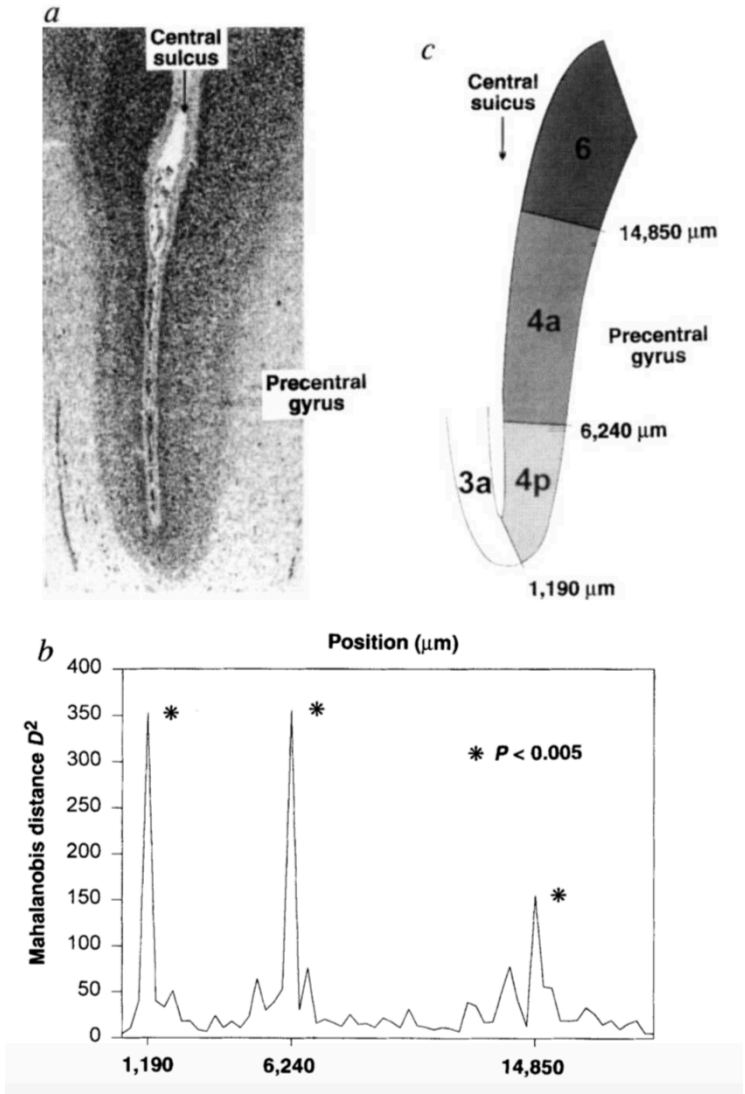

Figure 1-8 Delineation of two cytoarchitectonically distinct subdivisions (i.e. areas 4a and 4p) with the primary motor cortex (i.e. Brodmann area 4 [15]), using the Schleicher's [9] quantitative observer-independent microstructural parcellation technique. Source: [35].

Moreover, Schleicher, et al. [9] also developed an automated microscopic scanning procedure and software for extracting the GLI profiles along the cortex. Use of this automatic

scanning procedure facilitated microstructural cortical parcellation in a larger number of brains and a greater number of postmortem sections, compared to the limited cortical coverage and limited number of subjects examined in conventional mapping studies. Accordingly, the method was employed extensively in several following studies to also investigate the architectonic variability between different individuals and between the right and left hemispheres. Examples include the study of intersubject variability in Broca's region [37], in primary and secondary visual cortex [38], in somatosensory areas 2 [33], 3a, 3b and 1 [39], and investigating interhemispheric variability in the human parietal operculum [40].

Later, the microarchitectonic maps of individuals from these studies were transformed to a standard reference space, resulting in the creation of a comprehensive microarchitectonic atlas of the human cerebral cortex [41-43]. Such atlases enable group level examinations of the cortical structure-function associations (i.e. based on the comparisons made between the functional data from a group of living brains and the structural data from a group of postmortem brains integrated in the atlas). However, despite great advances in this regard, the inter-individual structural variability could not be resolved completely by using such atlases [1]. These atlases only provide probabilistic spatial location of the cortical areas, as they were generated using the averaged microarchitectural maps from a limited number of postmortem brains. Thus, *in vivo* cortical mapping methods were required to enable obtaining the structural and functional information from the same living individual.

1.3 IN VIVO CORTICAL MAPPING

Magnetic Resonance Imaging (MRI) has provided a non-invasive *in vivo* method for microstructural mapping of the human cerebral cortex at the individual level.

1.3.1 An Overview of MRI

MRI is mainly based on the behaviour of hydrogen nucleus (^{1}H), which is found in abundance in the human body (63% of atoms), when exposed to external magnetic fields. Each hydrogen nucleus consists of a single proton, which has electric charge, thus creating a magnetic dipole due to its net spin (intrinsic angular momentum) [44]. These magnetic dipoles are oriented randomly when there is no external magnetic field (Figure 1-9a). In MRI, an external static magnetic field (B_0) causes the dipoles of the sample to align parallel to the direction of B_0, creating a net magnetization within the sample (Figure 1-9b) [44].

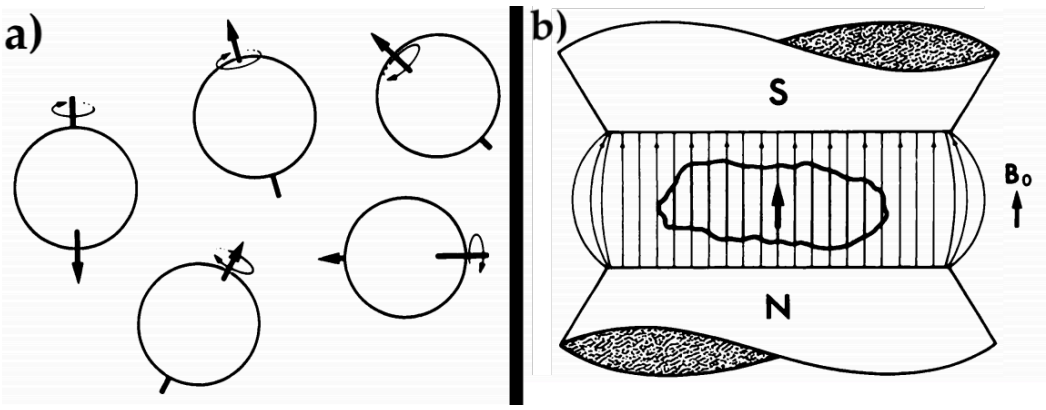

Figure 1-9 a) The nuclear spins are randomly oriented when there is no external magnetic field. b) The external static magnetic field B_0 generates a net magnetization within a sample. Source: [44].

The spins placed in the static B_0 field will continue their precession around an axis parallel to the B_0 direction, at the precession frequency of $\omega_0 = \gamma B_0$, where ω_0 is called the Larmor frequency and γ denotes the gyromagnetic ratio ($\gamma = 42.577e6\ Hz/T$) [45].

The net magnetization vector of the sample placed in the static B_0 field is calculated as the vector sum of the net magnetization of the spins aligned in the B_0 direction, and of those aligned opposite to the B_0 direction. At equilibrium, the net magnetization of the sample is aligned with the field, and thus cannot produce an MR signal, as it does not have a transverse component. To perturb the equilibrium, a short radiofrequency (RF) pulse is applied that generates a small magnetic field (B_1) for a very short period of time. As a result, a temporary effective magnetic field (B_{eff}) is created (where $\overrightarrow{B_{eff}} = \overrightarrow{B_0} + \overrightarrow{B_1}$.) that causes a torque in some spins, previously aligned with B_0, trying to align them in the B_{eff} direction. Consequently, the net magnetization vector of the spins is then tilted at an angle (i.e. the flip angle) relative to the B_0 direction (*Z*-axis) [44]. This process is called magnetization excitation and is illustrated in Figure 1-10.

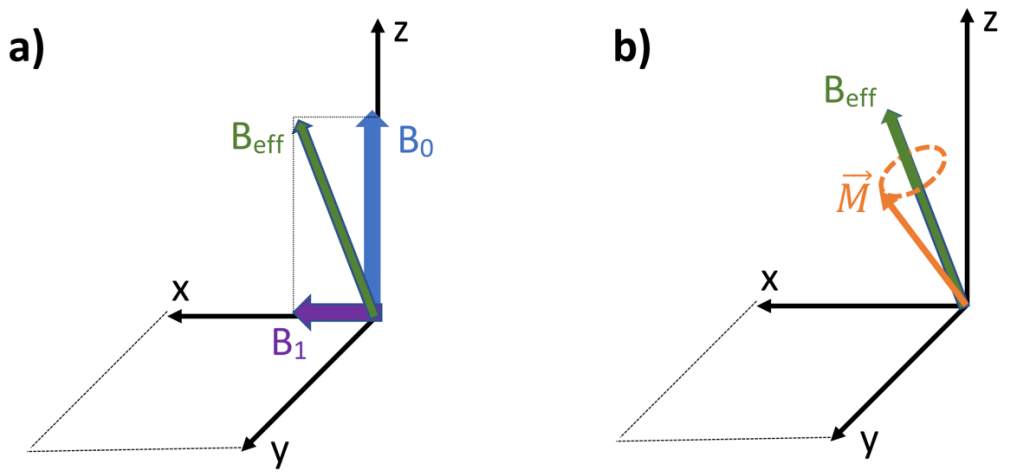

Figure 1-10 a) Applying a radiofrequency pulse along the X-axis adds a small magnetic field (B_1) in the X-axis direction, creating a new effective magnetic field (B_{eff}). b) Consequently, some spins are aligned in the B_{eff} direction, thus tilting the net magnetization vector ($\vec{M}$).

MR relaxometric properties

After the excitation, the spins tend to gradually return to the equilibrium state, due to the presence of the static B_0 field. The amount of time it takes for the spin magnetization to recover to its initial equilibrium state along the *Z*-axis is called the longitudinal relaxation time *T1* (spin-lattice relaxation) [45]. Additionally, the spin-spin relaxation process causes the spin magnetization to decay in the transverse plane (*X*-*Y* plane), which is perpendicular to the B_0 field direction. The transverse relaxation time *T2* characterises this process, which is also called spin dephasing [45]. Both T1 and T2 relaxation times are characteristics of different tissue types and are two main sources of contrast in MR imaging. For example, on T1-weighted MRI, fat tissue appears bright due to its fast longitudinal magnetization recovery to the B_0 direction. On the other hand, cerebrospinal fluid (CSF) appears dark, because of its slower longitudinal relaxation.

It should be noted that in the presence of magnetic field inhomogeneities (induced by instrument imperfections or magnetic susceptibility of the tissue), additional spin dephasing causes transverse relaxation to occur at a faster rate. In such cases, $T2^*$ is used to characterise the transverse relaxation process, where $T2^* < T2$ [45, 46].

1.3.2 Cortical Mapping Using MRI

Several MRI studies have demonstrated the capacity of MRI as a non-invasive probe of microscopic brain tissue components, promising to overcome the issues with classical histology-based mapping methods [47]. MRI allows the acquisition of 3D images of both the

structure and function of the same brain *in vivo*, facilitating the study of the brain structure-function associations.

MRI has been widely used for macro-anatomical imaging of the brain, revealing structures at the scale of 0.5 mm to 20 cm (e.g. measuring the thickness of the cerebral cortex [48], studying gender-related gyrification [49]). Further advances in MRI technology have pushed the limits of spatial resolution of MRI scans, enabling brain structures at the mesoscopic scale (0.1 – 0.5 mm [47]) to be imaged. Accordingly, a wide range of recent studies have exploited high resolution MRI image acquired on high-field MR scanners to, for example, characterise the myeloarchitectonic laminar structure of the cerebral cortex [50] and columnar cortical organisation [51, 52]. Nonetheless, direct characterisation of microscopic tissue components (e.g. myelin, axons, dendrites, glial cells) *in vivo* would require acquisition of higher resolution MR images (1 – 100 μm), which is not achievable using current MRI technology [47].

1.3.3 Quantitative MRI Microstructural Mapping

In conventional weighted MR imaging, the image contrast is weighted towards the MR parameter of interest (e.g. T1-weighted MRI). As a consequence of this, the contrast in weighted images is influenced by several factors and is not specific for tissue characteristics. For example, weighted MRI signal is affected by instrument characteristics and artefacts. In contrast, quantitative MRI methods provide a measurement of the MR parameter of interest (e.g. relaxation times, proton density (PD), magnetization transfer (MT), magnetic susceptibility and diffusion), and are thus reflective of the microstructural characteristics of the underlying tissue [53]. The advantages of employing quantitative MRI over traditional MRI methods for tissue characterisation are two-fold: i) reduced biases which result from instrument imperfections (e.g. transmit magnetic field inhomogeneity) and experimental protocol variations, and ii) improved specificity for particular microstructural characteristics [53].

At currently possible MRI resolutions, each voxel of the image contains several microscopic tissue components that contribute to the average MR signal measured from the voxel. Consequently, it is not feasible to directly measure the contribution of each microscopic component to the voxel-level MR parameter value. However, several studies have combined quantitative MRI techniques with biophysical models of the MR signal, to indirectly infer microstructural features of the tissue from voxel-level MR measurements [53].

Quantitative MR relaxometry for microstructural mapping

MR relaxometric properties have been widely used for microstructural mapping of the cerebral cortex because they are sensitive to several microarchitectonic characteristics [54].

Myelin affects the relaxation times (T1, T2, $T2^*$) of the water, because of the interactions between biomolecular components (e.g. lipids) in the myelin sheath and water molecules [55-57]. Water molecules trapped inside the myelin layers relax at a much higher rate, compared to intra- and extra-cellular water [58]. This effect can be used in quantitative microarchitectonic mapping methods to probe myelin density and distribution. For example, in [59] and [60] myelin water fraction (MWF) maps of the brain were created using the effect of myelin on T2 and T1.

Furthermore, the orientation of myelinated fibres has been shown to cause B_0 orientation dependence for T2 and $T2^*$ measurements [61, 62]. For example, Cohen-Adad, et al. [62] observed that $T2^*$ measurements of cortical areas with higher myelination exhibit larger B_0 orientation dependence. Consequently, this characteristic can be used to characterise the orientation of fibres in grey matter [62].

Paramagnetic (e.g. iron) and diamagnetic (e.g. myelin) microscopic tissue components are known to create local magnetic fields in the tissue. The induced magnetic field inhomogeneity affects $T2^*$ relaxation time as a result of the additional spin dephasing. Accordingly, this effect can be exploited to characterise iron and myelin concentration using quantitative $T2^*$ maps [63].

The described correlations between the microarchitectonic characteristics of tissue and voxel-level MR relaxometric measurements make it theoretically possible to employ quantitative MR relaxometry to infer the microstructural features of the cortex [47].

1.3.4 Multi-modal Quantitative MRI Microstructural Mapping

Despite the sensitivity of MR relaxometric measures to different microarchitectonic characteristics, these measurements also lack specificity. For example, higher concentration of both iron and myelin causes a decrease in T1 relaxation time. As a consequence of this, for voxels that contain both of these microscopic components, quantitative MR relaxometry cannot characterise the specific contributions of myelin and iron.

As a result, multi-modal quantitative MRI methods have been employed to resolve non-specificity issues [47, 53]. Figure 1-11 illustrates quantitative MRI methods developed to date to characterise the three main microscopic tissue components: myelin, iron and nerve fibres. This figure illustrates the concept of combining the complementary quantitative MRI modalities for more accurate microstructural characterisation.

Additionally, multi-modal MRI mapping methods aim at complementing the information from single modalities, to investigate the larger effect of a combination of microarchitectonic characteristics, on the MR signal [64].

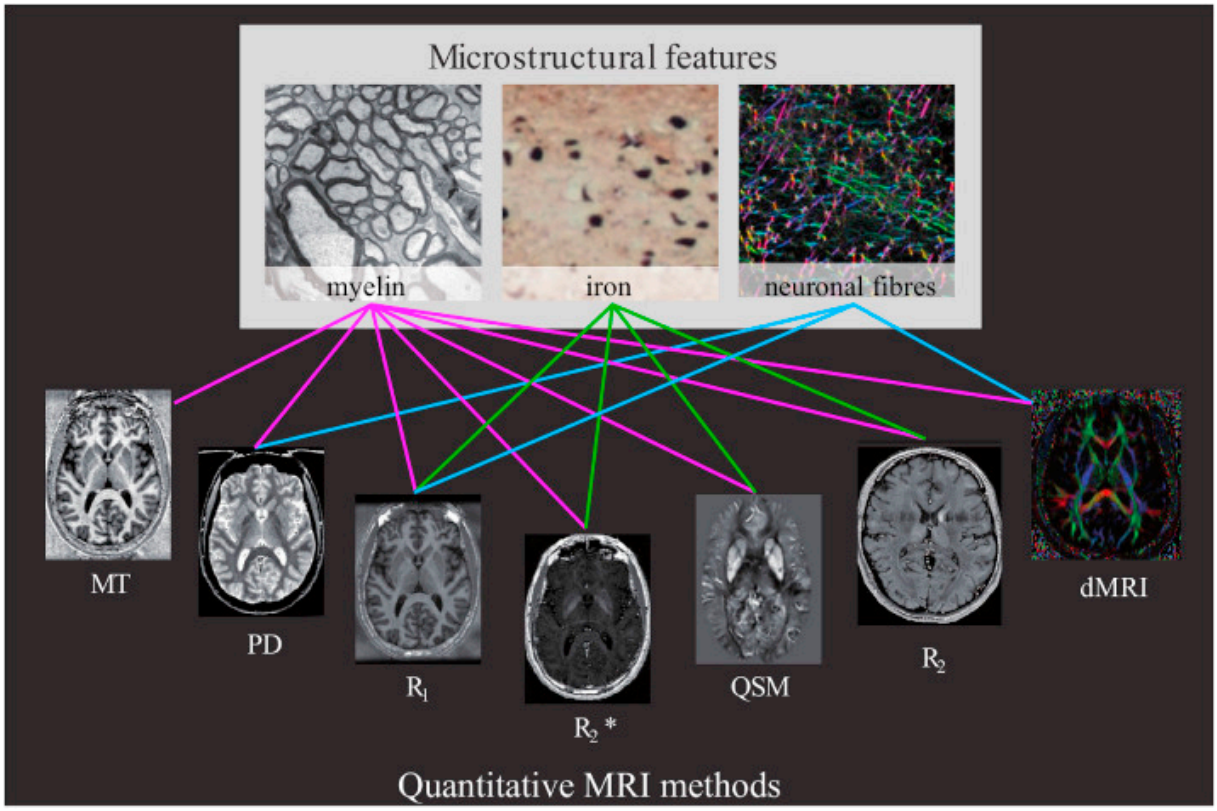

Figure 1-11 A summary of the quantitative MR modalities used in the literature for characterising three main microscopic tissue components: myelin, iron and neuronal fibres. Source: [47].

Despite the consensus on the efficacy of multi-modal quantitative MRI methods for microstructural mapping, these methods still suffer from long acquisition times and involve challenging and time-consuming data integration and complex data interpretation procedures [64]. Moreover, the multi-modal MRI methods developed to date, still have not been able to resolve the issue of lack of specificity throughout the cortex. This is mainly due to their limitation on the number of MR modalities that can feasibly be integrated together towards solving a problem [47].

1.4 MAGNETIC RESONANCE FINGERPRINTING (MRF)

Magnetic Resonance Fingerprinting (MRF) is a promising advance towards solving the issues with the previous multi-modal MRI cortical mapping methods. MRF provides a framework for fast and simultaneous quantification of multiple MR properties [10]. The key idea behind MRF is that it is a method for generating unique MR signal signatures (i.e. MR fingerprints) from particular tissue types (e.g. gray matter (GM), white matter (WM) and CSF). The MR fingerprints can then be subsequently matched with a precomputed database of MRF signal evolutions to extract tissue-specific information. To achieve this, the MRF framework in general consists of three main specifically designed components, as described in Figure 1-12.

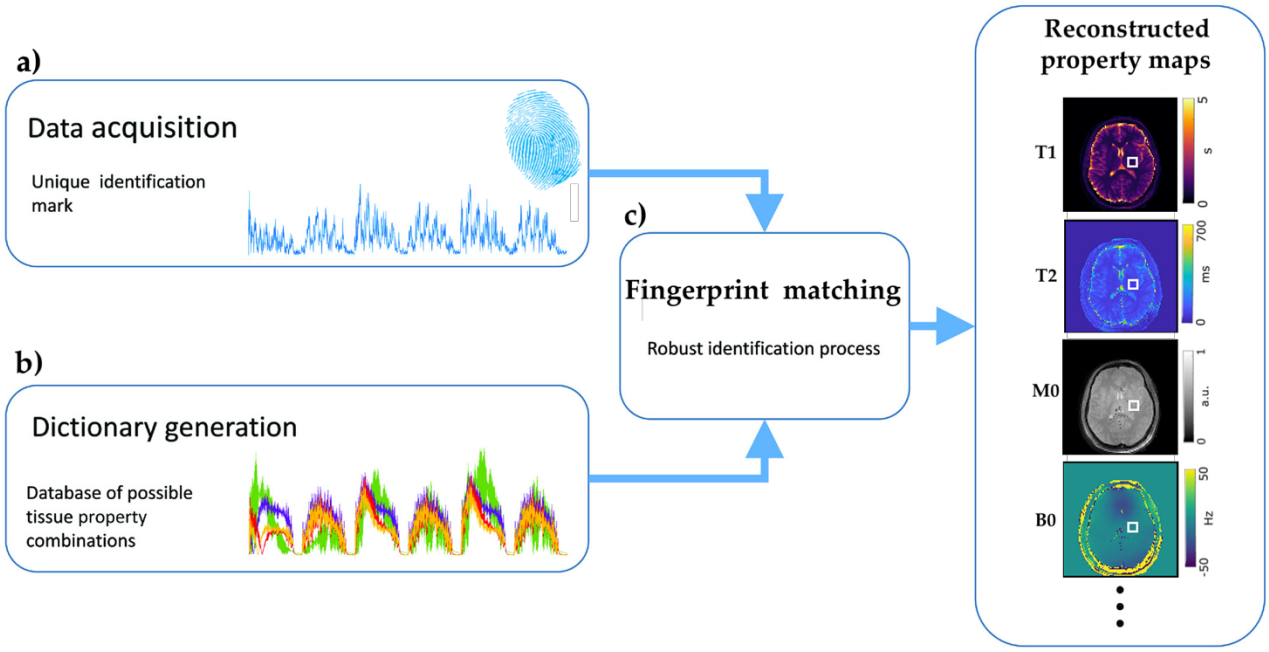

Figure 1-12 MRF framework consists of three main components: a) MRF data acquisition: unique MR fingerprint acquisition from particular tissue types, b) MRF dictionary generation: creating a database of simulated MRF signal evolutions for a specified range of properties of interest, and c) MR fingerprint matching: finding the best match for the acquired MR fingerprint, from the MRF dictionary. Source: adapted from [65].

1.4.1 MRF Data Acquisition

The first step in MRF is to acquire MRI signals that uniquely represent each distinct tissue type. To achieve this aim, an MRF sequence uses pseudo-randomised variation of the MRI acquisition parameters (e.g. flip angle (FA), repetition time (TR), echo time (TE), RF pulse phase, and k-space trajectory) at each signal acquisition step or data point. Figure 1-13 illustrates a schematic overview of a True Fast Imaging with Steady State Precession (TruFISP) MRF sequence.

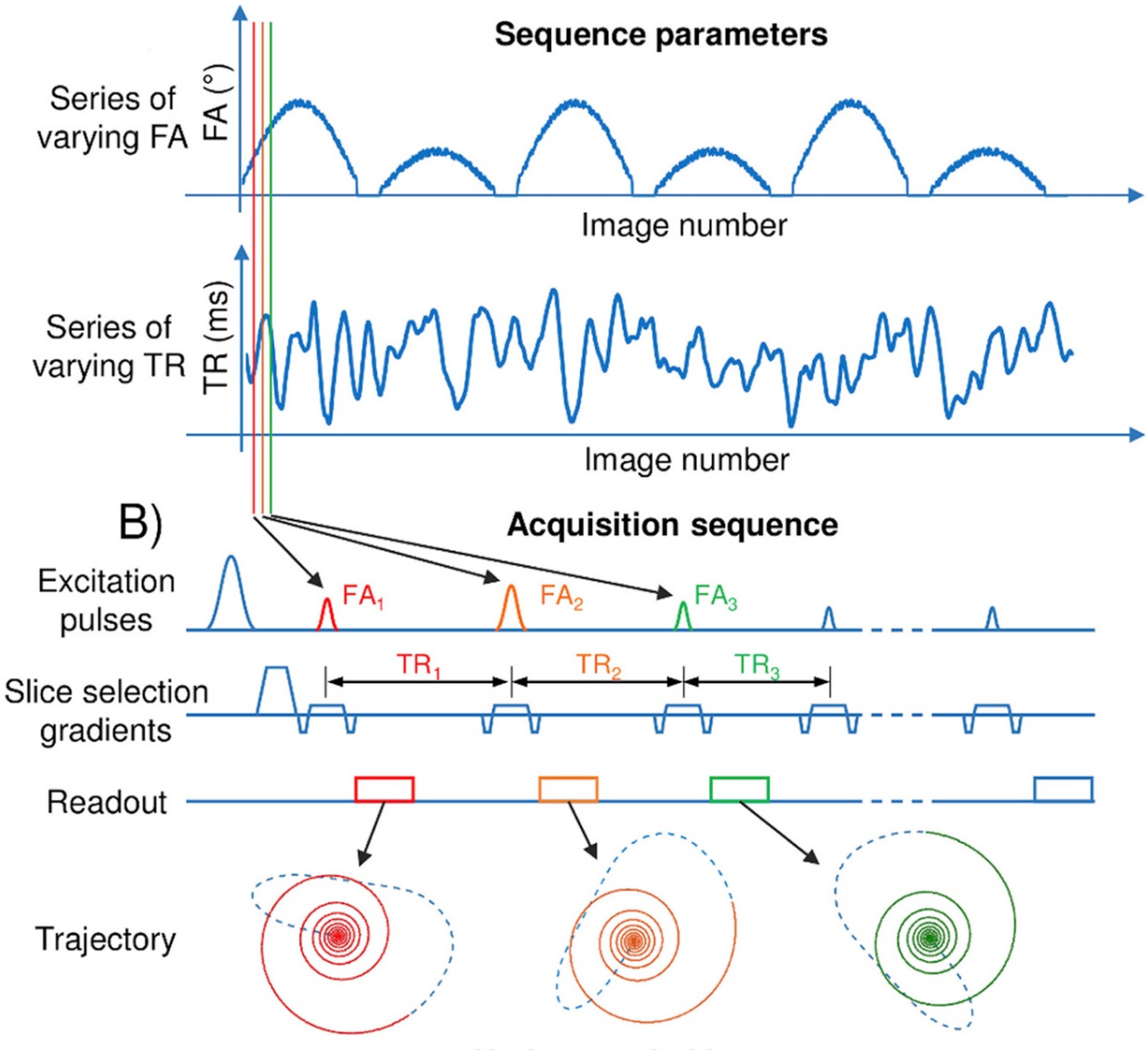

Figure 1-13 An example of an MRF pulse sequence diagram. Here, the flip angle (FA), repetition time (TR) and spiral k-space sampling trajectory parameters are varied at each acquisition repetition. Source: [66].

The MRF acquisition scheme is in contrast to conventional quantitative MRI sequences, in which only one acquisition parameter is changed at each acquisition repetition, and the magnetization recovers to the same initial state for the acquisition of all k-space data. A consequence of this is that conventional MRI sequences are capable of quantifying only a single tissue property within a long acquisition time [66]. Through variation of the acquisition parameters, the acquired MRF signal is sensitive to multiple tissue properties, thus providing a characteristic fingerprint for tissue types with different parameters.

One of the main features of the MRF framework is that it is not restricted to a specific type of MRI sequence or k-space sampling trajectory. Successful applications of balanced steady state free precession (bSSFP)-MRF [10], FISP-MRF [67], echo-planar imaging (EPI)-MRF

[68, 69], and quick echo splitting NMR (QUEST)-MRF [70] have been demonstrated in the literature for different purposes. Additionally, different types of k-space sampling strategies such as variable spiral density [10], radial [71] and cartesian [68, 69] readouts have been used in MRF studies.

1.4.2 MRF Dictionary Generation

MRF signatures acquired from each voxel are then matched to a dictionary of simulated MRF signal evolutions for different combinations of a range of tissue parameter values. Each dictionary entry consists of a specific set of parameter values and the simulation of spin magnetization evolution for a tissue with these property values. Figure 1-14 presents an overview of MRF dictionary generation process.

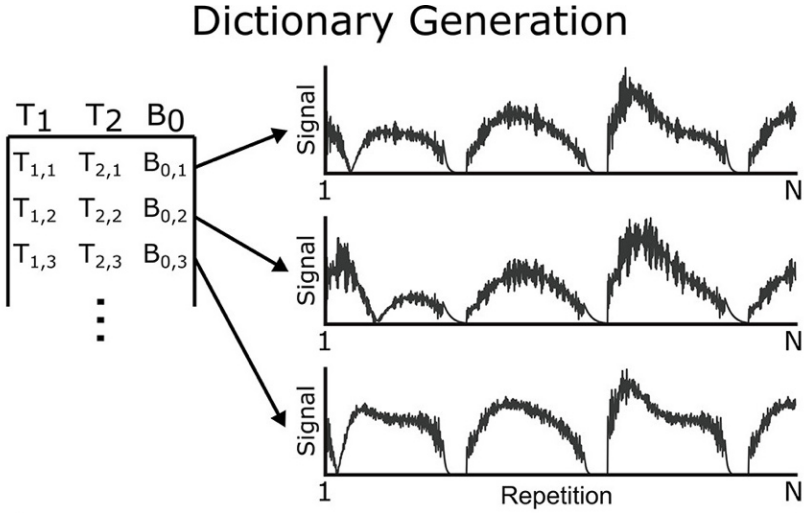

Figure 1-14 MRF dictionary generation involves simulating an MRF signal evolution of N repetitions for each possible combination of properties of interest (e.g. T1, T2, B_0) incorporated into the dictionary. Source: [72].

To simulate MRF signal evolution it is essential to employ an accurate signal model, as the model accuracy directly affects the MRF parameter quantification performance [65]. Bloch equations have been exploited as an accurate model of single isochromat and multiple isochromat magnetization behaviours in many MRF studies [10, 68, 69, 73]. However, some studies that used an MRF sequence with unbalanced gradients (e.g. FIST-MRF) have employed the extended phase graph (EPG) method [74] to increase the efficiency of multiple isochromat magnetization simulation [67, 71, 75, 76].

Several studies have demonstrated that usefulness of the MRF framework in quantifying a variety of parameters including T1, T2, proton density (M_0) [10, 77], off-resonance frequency (δf) [10, 77, 78], $T2^*$ [69, 77, 78], transmit magnetic field inhomogeneity ($B1^+$) [71, 79], brain

microvascular properties (e.g. cerebral blood volume, vessel diameter, and blood oxygen saturation) [80, 81] and perfusion properties (e.g. cerebral blood flow and bolus arrival time) [82], through the design of appropriate MRF sequences and dictionaries. It should be noted, however, that the incorporation of a larger number of parameters of interest in the MRF dictionary increases dictionary size, which can, in turn, degrade the efficiency of MRF parameter map reconstruction. Another factor that controls dictionary size, and thus reconstruction efficiency, is the step size between dictionary entry parameter values (i.e. dictionary resolution). Dictionary resolution affects the precision of MRF parameter quantification [67]. Therefore, when creating a dictionary, it is necessary to seek a trade-off between the desired level of time efficiency and precision, depending on the application [65].

1.4.3 Fingerprint Matching

MRF parameter map reconstruction involves a pattern recognition process, during which the best matching signal simulation from the dictionary is found for the MRF signature measured per voxel. Subsequently, the parameter values of the corresponding dictionary entry will be taken as the properties that best describe the tissue underlying each voxel.

Several pattern matching algorithms have been employed for MRF mapping, each providing a different level of quantification accuracy and efficiency depending on their degree of robustness to noise and k-space undersampling artefacts [65]. Figure 1-15 illustrates a simple template matching process that calculates the inner product of the measured MRF signal per voxel and the dictionary signal simulations. The dictionary entry simulation with the highest inner product is selected as the best dictionary match for the voxel fingerprint.

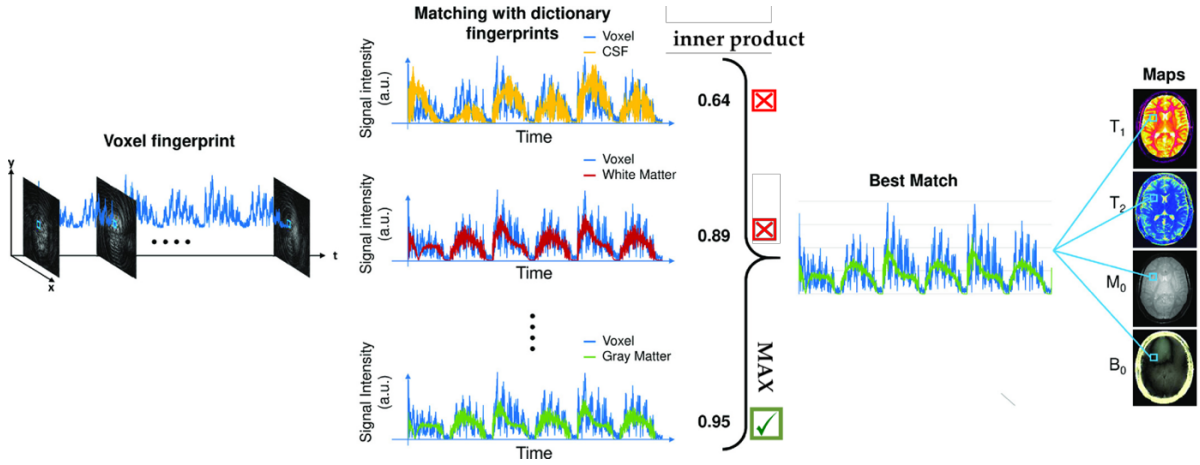

Figure 1-15 A pattern recognition algorithm searches through the simulated MRF signals in the dictionary to find the best match for the acquired MR fingerprint per voxel, and reconstructs the tissue property maps accordingly. Here, the maximum inner product between the voxel fingerprint and the MRF signal simulations is selected as the best match. Source: adapted from [65].

Inner product fingerprint matching has demonstrated robustness to noise, k-space undersampling artefacts, and artefacts due to subject movement during the latter part of the acquisition [65]. These characteristics have made inner product fingerprint matching a suitable pattern recognition approach for may MRF applications [10, 67-69]. Nevertheless, due to time-inefficiency, inner product matching is not optimal for clinical applications that require rapid parameter map reconstruction. To improve reconstruction efficiency in such applications, other pattern matching algorithms have been developed including singular value decomposition (SVD)-based time dimension compression [83], group matching [84], and low rank approximation [85].

1.4.4 Applications of MRF

The generalisability and flexibility of MRF framework in data acquisition, data postprocessing and image reconstruction, in addition to its high performance and efficiency in quantifying a variety of MR-related parameters have led to successful application of MRF in a diverse range of settings. Table 1.1 provides an overview of clinical brain MR imaging applications of MRF.

Table 1.1 Overview of MRF applications in brain MR imaging. Source: [72].

Application	Method Used	Performance	Considerations
Healthy Brain [86]	bSSFP-MRF [10]	"Identified age-related changes."	"Limited volume coverage. "
Pediatric Brain Development [87]	SSFP-MRF [67] and T2-prep modules [88]	"Performed without sedation. Changes in tissue properties and myelin water fraction with growth."	"Limited volume coverage. Validation of myelin water fraction needed."
Brain Tumours [89]	bSSFP-MRF [10]	"Differentiated low grade gliomas from metastases and healthy tissue."	"No statistical significance in grading solid neuronal tumours. Limited volume coverage."
Multiple Sclerosis (MS) [68]	Slice-interleaved MRF [68]	MS lesions were clearly identified on the resultant T1, $T2^*$ and proton density maps.	Optimisation of sequence acquisition parameters is required for enhanced parameter mapping accuracy and efficiency.
Epilepsy [90, 91]	3D MRF [73] or Sliding Window [92] SSFP-MRF [67]	"Better able to identify lesions in less time than existing methods."	"Nature of disease could require higher resolution."
Moyamoya [82]	ASL bSFFP-MRF [10, 93]	"Joint hemodynamic and relaxation maps, allowing for improved model fit. Observed differences between healthy and diseased tissue."	"Requires further sequence optimization for improved fitting. Sensitive to the choice of model."

In addition to brain imaging, MRF has also been employed in a wide range of other MRI applications including breast [94], cardiac [95], musculoskeletal [96] and abdominal [97] imaging. However, the application of MRF to cortical parcellation has hardly been investigated. A recent study has only explored variation of the MR relaxometric parameters (T1, T2) values, derived from MRF mapping, in a limited number of cortical areas [77].

1.5 APPLICATION OF MACHINE LEARNING IN BRAIN MAPPING

Machine learning (ML) algorithms have proved their efficacy and effectiveness in neuroimaging applications such as brain mapping. Supervised learning algorithms rely on the prior knowledge presented to them as a training set, to learn a statistical model that associates the characterised data samples (i.e. feature vectors) with output parameters of interest. An appropriately trained estimator will be able to then predict the value of

parameters of interest for newly observed data samples, which are characterised using the same features as in the training set [98]. On the other hand, unsupervised learning algorithms group the data samples into distinct clusters, such that the similarity between the samples of each cluster is higher than the similarity between the samples of different clusters [98].

Several diffusion MRI (dMRI) studies have benefited from machine learning methods for microstructural characterisation of the brain white matter (WM) [99]. Inferring microstructural tissue properties from dMRI signals is usually challenged by the choice of optimal models. Supervised machine learning algorithms have provided efficient methods for mitigating this problem. For example, Nedjati-Gilani, et al. [100] exploited random forest regression [101] to develop a statistical model for predicting axon radius, intrinsic diffusivity, intra-axonal volume fraction and intracellular water residence time, based on a set of features extracted from dMRI signals. Another dMRI-based study [102] used a Bayesian estimator [103], aiming to extract micro-level characteristics of the brain WM, independent of its mesoscopic organization effect (e.g. crossing WM fibres). A machine learning-based fibre tractography study have also used random forest classification to learn fibre directions based on the features derived from the raw diffusion-weighted MR signal intensities [104].

Machine learning techniques have also been applied to functional MRI (fMRI) studies. For instance, in [105] graph theory-based clustering was employed to show the feasibility of parcellating the whole cerebral cortex into functional subunits, using functional connectivity data acquired from resting-state fMRI (rs-fMRI). Another functional connectivity study [106] developed a spatially constrained spectral clustering technique and parcellated whole-brain rs-fMRI data into regions that have spatial coherence and homogeneous functional connectivity.

Another cortical parcellation study employed multi-layer perceptron (MLP) classification to develop an automated method for identifying 180 cortical areas (including 97 new areas) in individuals [107]. The training data in this study contained multiple MRI modalities, aiming to improve the precision of localising cortical boundaries. They included structural images (T1- and T2-weighted MRI) for extracting measures of cortical thickness and myelin content, task fMRI for cortical function, and rs-fMRI for functional connectivity of cortical areas. Consequently, the study benefitted from highly efficient data analysis potential of the MLP classification algorithm to accurately learn complex relationships between the large amount of data incorporated into the parcellation process.

These examples demonstrate the great potential of machine learning algorithms in efficiently solving computationally expensive problem of mapping different properties of the brain. Supervised classification algorithms, when trained on well-engineered feature vectors, can achieve high prediction accuracy performance in such applications.

1.6 RESEARCH SIGNIFICANCE AND AIMS

The overall goal of this PhD is to develop a new MRI method for identifying intracortical distinctions of microstructural tissue characteristics *in vivo*. Multi-modal quantitative MRI mapping methods have been employed, and demonstrated great promise in relation to increased sensitivity and specificity, which in turn result in more accurate tissue characterisation. However, lack of a comprehensive multi-modal mapping method that takes into account a wide range of microstructural (cytoarchitectonic and myeloarchitectonic) tissue properties, has been a major hurdle for achievement of precise whole-cortex microanatomical mapping. It is anticipated that the MR fingerprinting-based cortical characterisation framework described in this PhD project will lay a foundation for future developments to study the human cerebral cortex microstructure over and above the most commonly used MR relaxometry-based mapping methods.

To achieve the overall goal of this PhD, I followed the following three specific aims:

Aim 1: To investigate the presence of microstructural information in the MRF signals, complementary to the MR relaxometry-based microarchitectonic information

This was investigated as described in Chapter 2. A new quantitative method was developed based on Magnetic Resonance Fingerprinting (MRF) to i) eliminate the effect of MR relaxometry properties from the MRI signals (i.e. MRF residual signals), and b) statistically characterise the MRF residual signals generated from each area.

Aim 2: To investigate the feasibility of extending the spatial coverage of the MRF residual analysis framework.

This was investigated as described in Chapter 3. A 3D echo-planar imaging (EPI)-MRF sequence was employed to investigate the applicability of the MRF residual analysis framework (developed in Chapter 2) on the MR data obtained from a 3D volume imaging acquisition, as opposed to the single-slice (2D) acquisition performed in Chapter 2.

Aim 3: To investigate the feasibility of developing an automated *in vivo* voxel-wise microarchitectonic cortical parcellation method.

This was investigated as described in Chapter 4. Machine learning supervised classification algorithms were employed to propose an automated microanatomical mapping method for parcellating the cortex at the voxel level, using the information present in the MRF residual signals.

Chapter 2 Human grey matter characterisation based on MR fingerprinting residual signals

Shahrzad Moinian, Viktor Vegh, Kieran O'Brien, David Reutens, “Human grey matter characterisation based on MR fingerprinting residual signals”. Submitted to *Neuroimage*.

The above manuscript is incorporated in this thesis as Chapter 2.

I have made a substantive contribution to the authorship of the manuscript:

- Conception and design of the project.
- Analysis and interpretation of the data on which the manuscript is based.
- Drafting significant parts of the manuscript and critically reviewing it so as to contribute to the interpretation.

As the first author, I have participated in conceptualisation, experiment design, MR sequence development and testing, implementation of the data analysis scripts, data acquisition, data analysis and interpretation.

2.1 ABSTRACT

The importance of creating accurate anatomical maps of the human brain has motivated the development of observer-independent, reproducible *in vivo* mapping methods that account for inter-individual variations. However, a multi-parametric approach with whole brain coverage accounting for the combined effects of diverse microscopic tissue properties (i.e. cyto and myeloarchitectural features) has not been developed to date. To bridge this gap, we introduce a statistical residual analysis framework, which makes use of unique tissue-specific MR fingerprinting signals after adjusting for T1 and $T2^*$ effects. We used a 7T Siemens MR scanner to acquire MRF signals and quantitative $B1^+$ maps of the regions of interest. MRF dictionary matching was performed between MRF signals and simulated MRF profiles from a MRF dictionary, which was generated using a range of T1, $T2^*$, and $B1^+$ values. MRF signal residuals were then calculated as the difference between the actual and best matched MRF signal evolutions per region of interest. To compare the MRF residuals between regions of interest, we used normalised autocorrelation as a statistical characterisation method. In the three specific cortical areas (i.e. primary motor cortex, primary somatosensory cortex and premotor cortex) of six female participants, the residual analysis approach consistently showed inter-areal dissimilarity profiles in agreement with histology-based microstructural studies, indicating the MRF signal residuals contain information on tissue microstructure. Our MRF residual analysis framework enabled us to identify the microstructural variations between the cortical areas of interest based on the information that is complementary to MR relaxometry-based (i.e. T1, $T2^*$) information, which has been most commonly used for microarchitectonic characterisation of the human brain cortex. As the proposed analysis framework is directly applicable to the MR images of individuals, it may potentially be used to examine microanatomical variability between individuals in a population. The framework may also have potential for automated voxel-wise microanatomical parcellation of the entire cerebral cortex.

2.2 INTRODUCTION

Parcellation of the human cerebral cortex has been of major interest in neuroscience since initial histological studies at the beginning of the 19th century [15, 16, 25, 30]. Accurate delineation of regions of the cerebral cortex in individuals has an important role in neurosurgical treatment planning. Precise characterisation of regional variations in tissue microstructure may also aid the detection of pathology [5, 6, 108] and lead to increased understanding of structure-function correlations in the brain [2, 3].

A key drawback of classical cortical maps based on histology is non-reproducibility due to reliance on subjective, qualitative criteria to define cortical areas. To tackle this problem, Schleicher, et al. [9] introduced the first quantitative histology-based method. The method was a transition from qualitative to quantitative microstructural mapping, which has been utilised in several large-scale histological studies of cortical microstructural mapping [38, 39, 109]. However, because these studies are based on data from a limited number of post-mortem brains, inter-individual microstructural variations could not be addressed.

Whilst MR imaging technology facilitates the development of *in vivo* quantitative methods for microstructural mapping in individuals, the achievable voxel size hampers direct imaging of microstructural components (e.g. neuronal cell bodies, myelin and axons) on the order of tens of micrometres. As a result, quantitative MR-based microstructural mapping methods try to find the association between the voxel-level quantitative MR measures and the underlying variation in microstructure [47, 64]. A robust method to achieve this has been to utilise mathematical models to estimate microstructural features (e.g. fibre orientation, myelin density and cortical depth) from quantitative MR properties [47, 53, 62, 110, 111]. Quantitative MR relaxometry measurements such as T1, T2, and $T2^*$ are most commonly used [112], due to the high sensitivity of MR relaxometry measurements to variations in tissue microstructural features such as fibre orientation [62], myelin density [113, 114] and cortical depth [114]. While relaxometric methods are show promise as tools for microstructural analysis, more recently the specificity of MR relaxometry measurements for microscopic features has been questioned [47, 53, 64]. For example, a decrease in the value of T1 in a T1 map could be caused by higher myelination or greater iron concentration an issue that is present for regions such as primary motor cortex, primary somatosensory cortex and primary visual cortex [115]. As such, information complementary to relaxometry-based measures are required to improve the accuracy of microscopic tissue characterisation.

Multi-contrast quantitative MRI methods have the potential to provide an appropriate avenue for mapping tissue microstructural variations across the human cerebral cortex. Several studies have shown that complementary information about microstructural properties can be derived from different MR modalities such as Quantitative Susceptibility Mapping (QSM) [116], Magnetization Transfer imaging (MT) [117] and Diffusion Tensor Imaging (DTI) [118]. The combination of complementary quantitative MR parameters that are sensitive to different microstructural components could allow more specific characterisation of the cortical tissue microstructure [47, 64] than is possible with relaxometric measurements alone. For the example above in which T1 and $T2^*$ provides overlapping information about iron and myelin content, the addition of information obtained from the opposing effect of myelin (diamagnetic susceptibility induces negative frequency shift) versus iron (paramagnetic susceptibility induces positive frequency shift) on QSM could allow more accurate characterisation of cortical areas where the influences of both iron and myelin content are present [115, 116].

Despite improvements in quantitative multi-modal MR-based methods, their successful application to microstructural parameterisation in individuals remains a challenge [47, 64]. The best strategy for multi-contrast data acquisition and subsequent integration and interpretation of information from different modalities are still debated. Besides these issues, the most established multi-modal MR-based cortical mapping methods developed to date only exploit a limited number of MR modalities and are designed to show specificity and sensitivity to a limited number of microstructural characteristics, thus neglecting the effect of other microscopic components [47]. As a consequence, the wider applicability of the resultant multi-modal models throughout the cortex may be limited. To the best of our knowledge no *in vivo* quantitative method has been developed that characterises the combined effect of all microscopic tissue components on the MR signal across the cortex.

Magnetic Resonance Fingerprinting (MRF) is a multi-parametric method that potentially addresses the above-mentioned challenges [64]. This novel quantitative MR imaging method was first introduced by Ma, et al. [10] in 2013. As its name implies, the approach relies on generating unique MR signals (known as fingerprints) from different tissue types through pseudo-randomised variation of the acquisition parameters (e.g. repetition time, flip angle and echo time). These fingerprints can then be used in a pattern matching process to retrieve voxel-level MR tissue properties (e.g. T1, $T2^*$, off-resonance frequency and proton density) from a database of precomputed signal evolutions. The acquisition strategy of MRF allows simultaneous quantification of multiple tissue properties through a single scan and is

the key to resolving the existing issues with other multi-modal MRI methods. Previous studies have exploited used MRF in a variety of clinical applications including detecting and characterising brain tumours [89, 119] and identifying epileptic [90] and multiple sclerosis [68] lesions. The application of MRF in cortical parcellation has also been recently explored [120] but only utilises MR relaxometry measurements derived from the MR fingerprinting pipeline. To date, the utility of MR fingerprinting in characterising tissue microstructural variations based on the information complementary to the MR relaxometry quantification has not been investigated and is the purpose of our study.

Unlike existing MR-based multi-modal microarchitectonic characterisation methods, instead of focusing on understanding the isolated effects of a limited number of microstructural tissue components on the MR signal, we aimed to develop a method that can take into account the combined effect of the ensemble of components. To achieve this, we adapted the MR fingerprinting framework to remove MR relaxation effects from the MR signals (here called MRF signal residuals). The residuals provide us with a basis for examining the remaining non-relaxometry information in the MR signals as a whole and exploring their association with the microstructural feature variation across the cortex.

2.3 METHODS

2.3.1 Subjects

Six female volunteers participated in an hour-long 7T MR scan session. Participants were healthy individuals aged 30 ± 3 years with no history of neurological disease. All participants were provided with an overview of the experiment and signed a written consent prior to the scan. The scan protocol was approved by the local ethics committee, and was conducted at the Centre for Advanced Imaging, The University of Queensland. Each participant underwent three scans for T1-weighted anatomical image acquisition, transmit magnetic field ($B1^+$) mapping and MRF acquisitions.

Cortical areas

We targeted three areas with known level of microstructural dissimilarity to each other, as widely agreed in previous observer-independent microstructural studies [39, 62, 121]. We selected two areas with a high degree of microarchitectonic dissimilarity, and the third with features intermediate to the other two areas. Accordingly, we chose primary somatosensory

cortex (area 2) and anterior primary motor cortex (area 4a) because of their reportedly high cytoarchitectural [39] and myeloarchitectonic [121] dissimilarity. Additionally, premotor cortex (area 6) was chosen because of its intermediate myeloarchitectural dissimilarity to area 2 and 4a [62, 121]. For example, on average, area 6 has been reported to be less heavily myelinated than area 4a, and more heavily myelinated than area 2 [121].

We extracted the binary masks of these three areas from the Juelich cyto and myeloarchitectonic histological atlas of the human brain [41, 122], integrated in the FMRIB Software Library (FSL) for brain imaging data analysis [123]. MRF signal evolutions and $B1^+$ values were extracted from each voxel in the three cortical areas, using the procedure explained in section 2.3.3.

2.3.2 MRI Acquisition

All MRI scans were conducted using a 7T whole-body MRI research scanner (Siemens Healthcare, Erlangen, Germany) with a 32-channel head coil (Nova Medical, Wilmington, Massachusetts). To minimise susceptibility effects, we performed B0 shimming at the beginning of each scan session.

$B1^+$ map

To account for the effect of transmit magnetic field (B1+) inhomogeneity in high-field MRI we acquired a whole-brain B1+ map. A 3D Saturation-prepared with 2 Rapid Gradient Echoes (SA2RAGE) sequence [124] was utilised with the following parameters: TR = 2400 ms, TE = 0.95 ms, FA1/2 = 6°/10°, voxel size = 4 × 4 × 4 mm, and matrix size = 48 × 58 × 64.

T1-weighted anatomical image

T1-weighted anatomical images were acquired to create individual's grey matter mask, co-register $B1^+$ maps with the MRF images, and transform Juelich atlas masks of the selected cortical areas from the MNI-152 space to the MRF space. We acquired T1-weighted anatomical image of each participant using a prototype 3D Magnetization Prepared 2 Rapid Acquisition Gradient Echoes (MP2RAGE) sequence [125] with the following parameters: repetition time (TR) = 6000 ms, echo time (TE) = 3.97 ms, inversion time TI1/2 = 800 ms/2700 ms, flip angle FA1/2 = 4°/5°, voxel size = 1 × 1 × 1 mm, and matrix size = 222 × 240 × 144.

MRF acquisition

The MRF signal measurements were acquired using a 2D MRF pulse sequence developed in-house, based on a 2D single-shot Echo-planar Imaging (EPI [126]) readout, with the following parameters: Number of repetitions = 1000, TR = 80-90 ms, FA = 0-80°, TE = 24 ms, Radio Frequency (RF) pulse phase = alternating between 0° and 180° every second frame, Partial Fourier Phase = 6/8, voxel size = 1 × 1 mm, and matrix size = 200 × 200. We used Generalized autocalibrating partially parallel acquisitions (GRAPPA) parallel imaging [127] (with acceleration factor =3 and reference lines = 36) and Fat Saturation technique, respectively to increase in-plain resolution and reduction of common artefacts observed in EPI sequences at high field scanners. The suggested pseudo-randomised patterns in [10] for flip angle and repetition time variations were used, but with a different range of values for TR considering the EPI sequence limitations on the minimum possible echo time at high field. These patterns and range of values are illustrated in Figure 2-1.

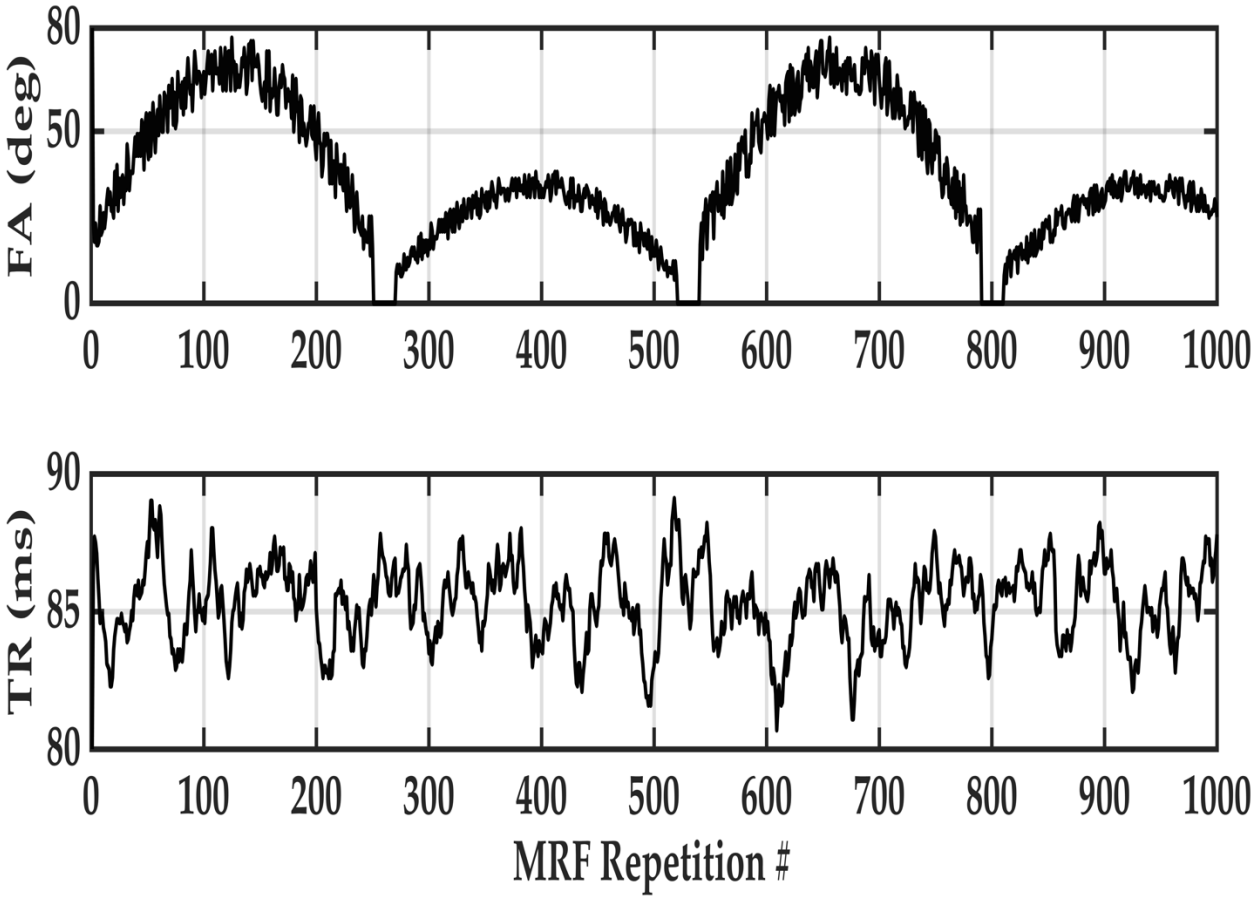

Figure 2-1. The pseudo-randomised patterns used to acquire and simulate 1000 MRF image frames. The flip angles (FA) range from 0 to 80 degrees and follow a sinusoidal pattern. The repetition time (TR) values are generated using a Perlin noise pattern [128] and vary between 80 and 90 ms.

Due to the acquisition time limitations imposed by the 2D sequence being used, for MRF measurements we acquired six 2D slices to cover the cortical regions of interest for this study. To deal with the low signal-to-noise ratio (SNR), commonly observed in EPI sequences, each MRF slice acquisition was performed three times. Figure 2-2 depicts the position of the six 2D MRF slices acquired from one participant, overlaid on top of the three cortical areas of interest, and the MP2RAGE anatomical image of the individual.

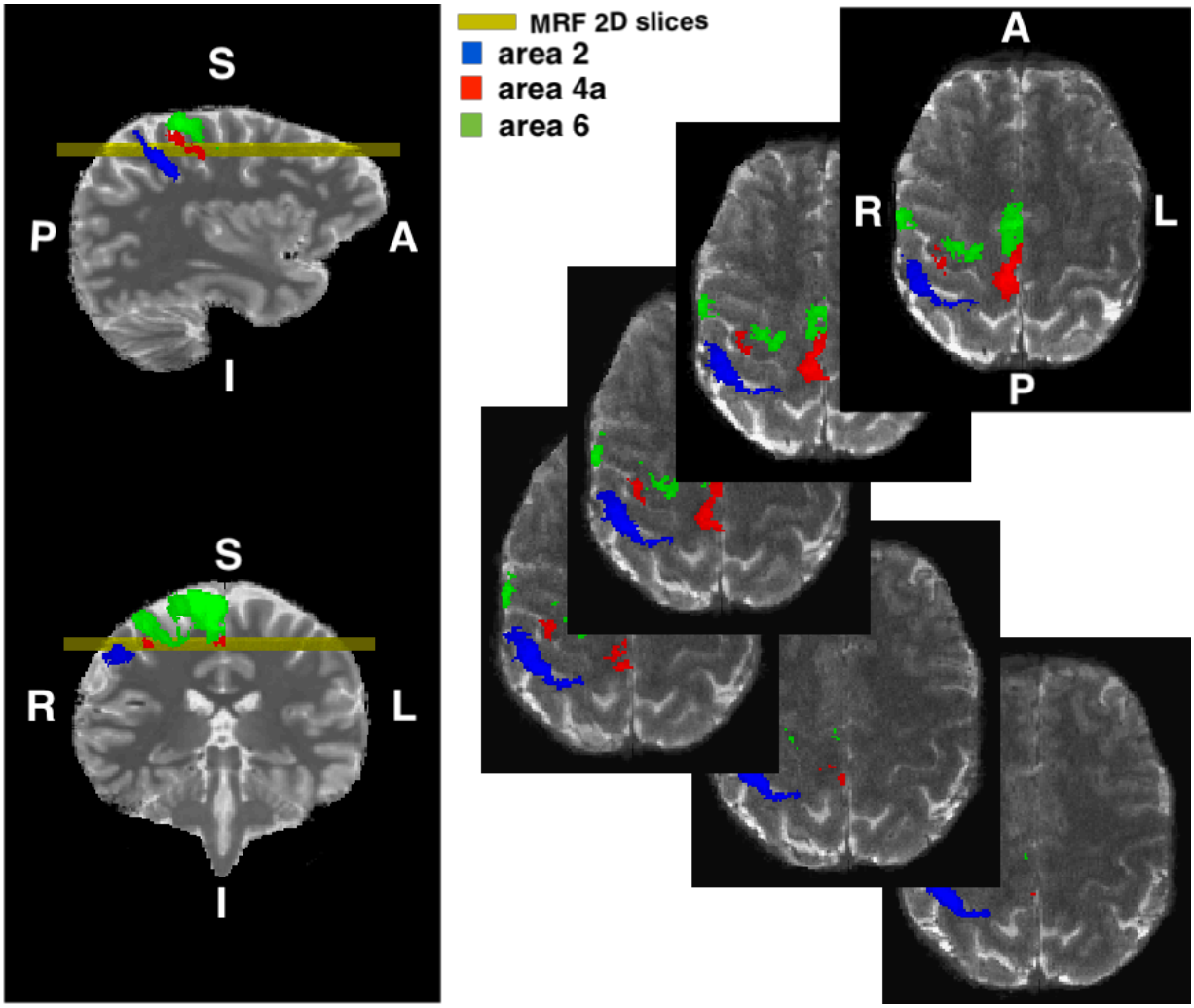

Figure 2-2. The binary masks of target cortical area 6 (green), area 4a (red) and area 2 (blue) are extracted from Juelich Histological atlas of human brain. The six MRF 2D slices (yellow) are overlaid on the MP2RAGE anatomical image of a participant.

2.3.3 Image Processing

For each participant, we first performed brain tissue extraction of all images, using FSL Brain Extraction Tool (BET) [129]. We linearly co-registered (using 2D FMRIB's Linear Image Registration Tool (FLIRT) with 6 degrees of freedom (DOF) [130, 131]) and then averaged 2D MRF images of the three repetitions for each slice. Next, the brain-extracted MP2RAGE and SA2RAGE images were co-registered with the averaged 2D MRF images, using FSL

FLIRT with 6 DOF. We then performed a two-level non-linear registration, using FNIRT [132], to transform the binary masks of the Juelich histological atlas target areas, from the MNI-152 standard space to the MRF native space. Finally, we used the transformed binary masks to extract MRF signal evolutions and $B1^+$ values per voxel from the selected cortical areas (in MATLAB and Statistics Toolbox Release 2015a, The MathWorks, Inc., Natick, Massachusetts, United States).

To account for interindividual differences when using the atlas probability masks of the cortical areas, we only included the voxels that intersect with the grey matter ribbon of the individual and we set the threshold on probability values to be >60% when creating the atlas masks. The individual's grey matter tissue was extracted from the MP2RAGE T1-weighted image, using the Statistical Parametric Mapping (SPM12) segmentation software (http://www.fil.ion.ucl.ac.uk/spm) [133]. To account for the partial volume effect, we then excluded the voxels below the threshold of 90% from the resultant probabilistic grey matter tissue segmentation, and accordingly created a binary mask of the individual's grey matter.

2.3.4 MRF Dictionary Matching

MRF dictionary matching is the process of retrieving tissue properties of interest for each voxel through matching the voxel's MRF signal to a dictionary of precomputed MRF signal profiles. The tissue properties and the range of parameter values contained in the MRF dictionary may vary for different applications.

Here, we generated an MRF dictionary containing T1 and $T2^*$ relaxometry properties within the following range: T1= 100 ms – 5 s (in steps of 10 ms, 20 ms, 30 ms , 40 ms and 50 ms for 100 ms – 1s, 1s – 2 s, 2s – 3s, 3s – 4s, and 4 s – 5 s, respectively; $T2^*$= 10 – 400 ms (in steps of 2 ms, 3 ms, 5 ms and 10 ms for 10-20 ms, 20-40 ms, 40-200 ms, and 200-400 ms, respectively). Additionally, to account for the effect of $B1^+$ inhomogeneity on MRF signals, we followed the approach proposed in [79] and added $B1^+$ values ranging from 0.4 to 1.4 in steps of 0.05 to the dictionary parameters.

The MRF signal profile for the set of parameter values at each dictionary entry was generated in MATLAB R2015a, using the Bloch equations simulation of the transverse and longitudinal magnetizations in the rotating frame of reference [45]. The $B1^+$ value of each dictionary entry was multiplied by the nominal flip angles (Figure 2-1) to calculate the actual flip angles for the MRF signal simulations [79].

We used inner product to identify the closest match for each voxel's MRF signal signature among the simulated signal profiles in the dictionary. For increasing the efficiency of the pattern matching process, the SA2RAGE $B1^+$ value of the voxel was used to select the subset of dictionary entries with equal B1+ values [79]. The dictionary entry with the maximum inner product was selected as the best MRF signal simulation for the voxel of interest.

2.3.5 MRF Residuals

Our MRF residual analysis framework is illustrated in Figure 2-3. Here, we added a MRF residual signal calculation, followed by a statistical residual analysis process, after the dictionary matching step.

The best fitted MRF signal simulation obtained from the MRF dictionary matching step provided the best representation of the influence of T1 and T2* properties of the voxel's underlying tissue on the MRF signal. Accordingly, in line with the aim of the present study, we subtracted the best fitted MRF signal simulation from the acquired MRF signature, allowing us to eliminate the effect of T1 and $T2^*$ relaxometry properties from the MRF signal and examine the remaining signal (here called the MRF residual). Consequently, for each voxel, we define $MRF_{residual}$ as the difference between the acquired MRF signal evolution ($MRF_{acquired}$) and the simulated MRF profile ($MRF_{simulated}$) from the dictionary:

$$\mathrm{MRF}_{residual} = \mathrm{MRF}_{acquired} - \mathrm{MRF}_{simulated}$$

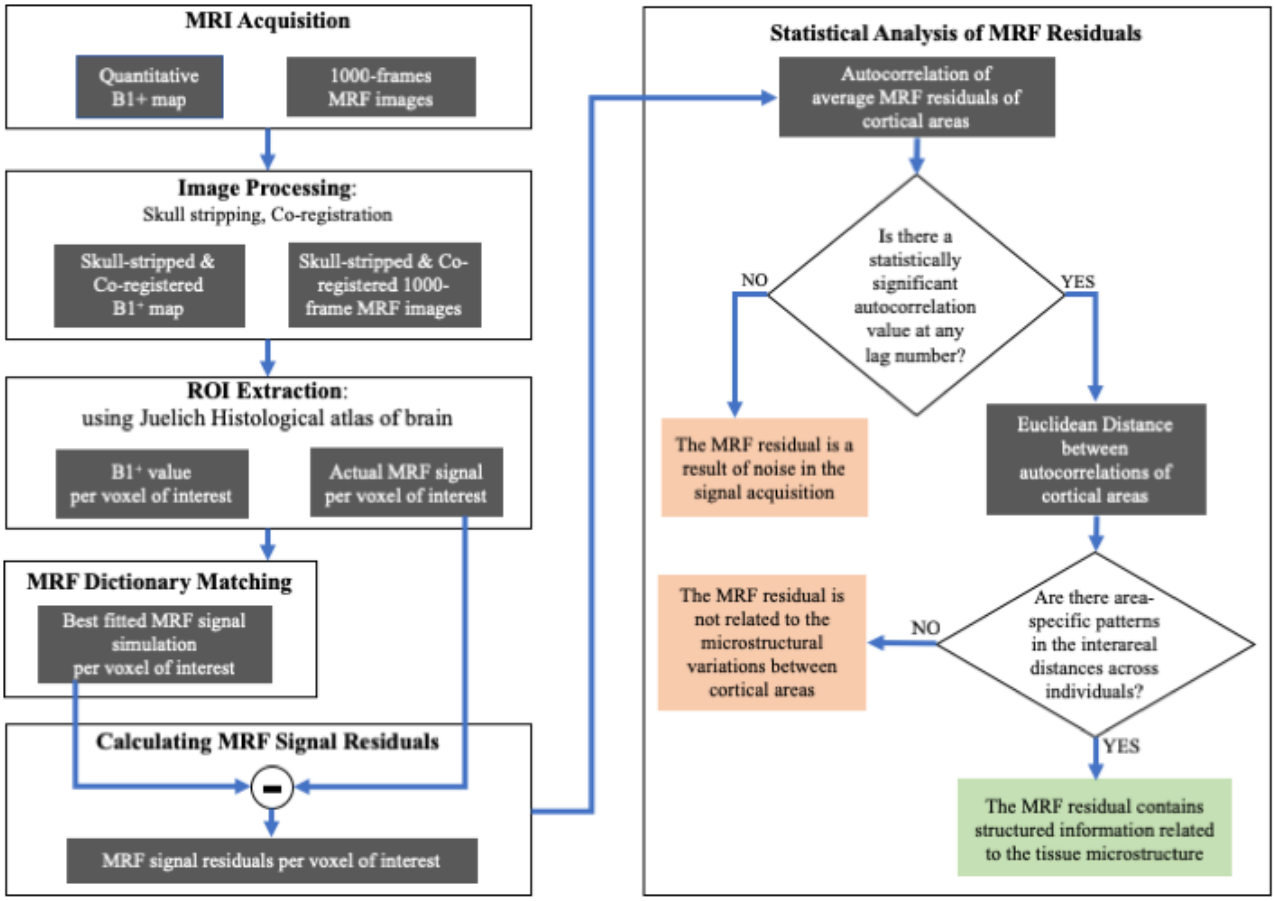

Figure 2-3. The framework for the analysis of residuals of simulated and acquired MRF signals, to investigate the sensitivity of MRF residuals to microstructural variations between three cortical areas.

2.3.6 Statistical Analysis of the MRF Residuals

The purpose of this final step in our proposed framework was to statistically characterise the MRF signals after accounting for the effect of T1 and $T2^*$ relaxometry parameters, enabling statistical comparison of the MRF residuals between different cortical areas.

We examined the residuals for two main characteristics. We first performed a white noise test on the MRF residuals to investigate the presence of unexplained structure in the MRF signals. We then tested whether the non-noise residuals had characteristics that were systematically related to the cortical areas of interest.

White noise test

An essential requirement of a well-established model that explains all the fundamental aspects of the actual process is that the residuals have characteristics of white noise i.e. the residual values should be independently distributed around a mean value of 0, meaning no correlation between the values. Hence, we compared the distribution of autocorrelation values of its residuals with a white noise distribution [134]. Autocorrelation measures the

correlation coefficient between a signal and a shifted version of itself at the specified lag number. In this work, we used Normalised autocorrelation to ensure a uniform range of coefficient values when comparing autocorrelations of different cortical areas. Normalised autocorrelation values vary between -1 to +1, indicating the highest negative and positive correlations, respectively. This value is always +1 at lag 0, indicating that the signal is identical to itself.

We then compared the distribution of the autocorrelations of the MRF residuals and Gaussian white noise (with 95% confidence intervals). This allowed us to qualitatively test if the MRF residuals are significantly different from a white noise process. If a process is white noise, then its autocorrelations should 1) be randomly distributed around the mean value of 0, and 2) fall within the confidence interval boundaries. If the autocorrelations of an MRF residual signal exceeded these confidence intervals at one or more lags (here termed significant autocorrelations), we concluded that the residual was not solely the result of random noise present in the MRF signal.

Interareal dissimilarity measurement

We explored the presence of area-specific structures in the MRF residual signals by investigating how well the residuals of the MRF signal from each cortical area (after accounting for T1 and $T2^*$ effects) could be separated. We employed autocorrelation, a robust statistical measure for the analysis of noisy time series similarity. As [134] discussed, a similar profile of autocorrelations suggests that their associated time series are from similar underlying processes. Euclidean distance was used as a metric to assess the dissimilarity in autocorrelations profiles [134]. The Euclidean distance (ED) between autocorrelations of area *X* and area *Y* was defined as

$$ED_{XY} = \sqrt{\sum_{i=1}^{n} (a_{Xi} - a_{Yi})^2} \quad (1)$$

where a_{Xi} and a_{Yi} denote the autocorrelation of MRF residuals from area *X* and area *Y* at lag *i*, respectively and *n* represents the total number of lags. The larger the distance value, the more dissimilar the shape of the autocorrelations of the two residuals, reflecting a greater dissimilarity between the two areas. A Euclidean distance of *0* identifies two identical areas.

Statistical inference

Randomness in the residuals

To evaluate whether the difference between the normalised MRF residuals and white noise was statistically significant, we performed Wald-Wolfowitz runs test [135]. This is a nonparametric randomness test that efficiently detects higher-order autocorrelation in a residual signal [136]. The runs test statistic is based on the number of consecutive residual values that preserve the same sign, known as a *run*. The *runs* test statistic calculated for a large sample (i.e. number of time points > 10) of white noise has a standard normal distribution. This allowed us to test the null hypothesis of randomness in the MRF residuals, against the alternative hypothesis of autocorrelated residual values.

Significant areal dissimilarity

To examine if the difference between the cortical areas was statistically significant, we performed the Wilcoxon signed rank test [137] on the Euclidean distance values (ED_{XY}). This is a nonparametric test for paired observations and is used when a normal distribution cannot be assumed for the populations. Using this test, we evaluated whether the dissimilarity between areas *X* and *Y* (measured as ED_{XY}) was significantly different from the dissimilarity between areas *X* and *Z* (measured as ED_{XZ}). Here, the null hypothesis was that $ED_{XY} - ED_{XZ}$ had a distribution with median of 0.

2.4 RESULTS

2.4.1 Comparison of MRF Residuals and White Noise

Figure 2-4 illustrates results of the qualitative white noise test performed on MRF residuals of the three cortical areas of interest, for two example participants. The normalised autocorrelations of area 4a, area 6 and area 2 exceed the 95% confidence intervals of a Gaussian white noise autocorrelation distribution at approximately half the total number of lags. This demonstrates significant correlation between MRF residual values of each cortical area at those lags, suggesting that the MRF residuals are significantly different from a white noise process for both participants. Similar observations were made for the MRF residuals of the other four participants.

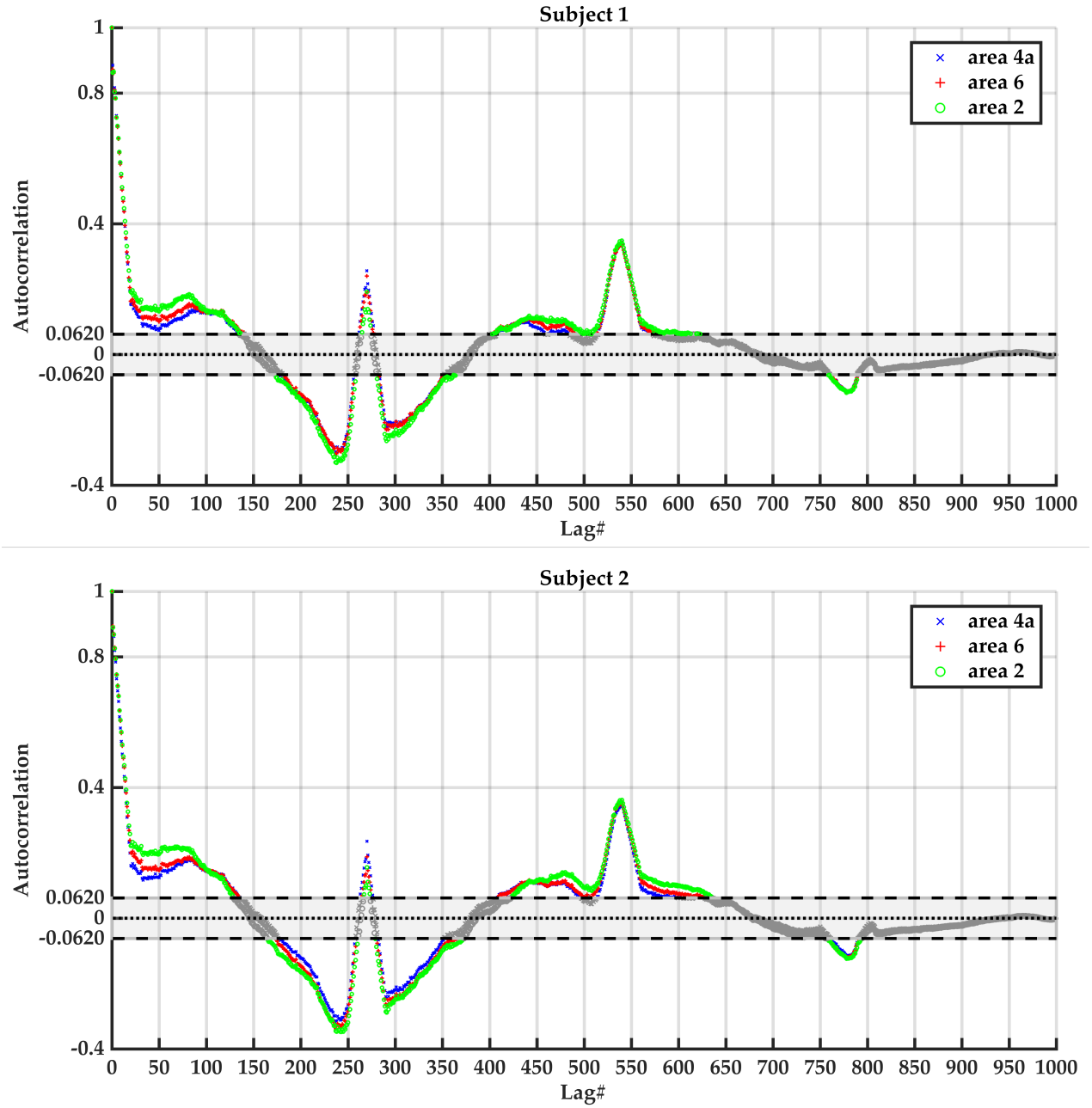

Figure 2-4 Normalised autocorrelation of the MRF residuals of area 4a (blue), area 6 (red) and area 2 (green) overlaid on the 95% confidence intervals (±0.062) of a Gaussian white noise autocorrelation distribution. Autocorrelation values that fall between the 95% confidence intervals are greyed out, indicating their insignificance when compared with the white noise autocorrelation distribution.

The Wald-Wolfowitz runs test indicated significant ($P<0.05$) non-randomness in the MRF residual signals of area 4a, area 6 and area 2, for all six participants examined in this study.

2.4.2 Area-specific Patterns of MRF Residuals

Figure 2-4 shows that the autocorrelation profile of each area seems to be a function of the lag number. In other words, the autocorrelation of each area appears to have a characteristic pattern. The mean and standard deviation of the autocorrelation profile of each area of interest across the six participants was compared, as illustrated in Figure 2-5. This figure

confirms the presence of an autocorrelation pattern for each cortical area, which could make it distinguishable from the other areas of the same participant. For example, from visual inspection of autocorrelations between lags 21 and 85 in Figure 2-5 we can observe that area 2 average autocorrelations change within a small range just above 0.16. In contrast, area 4a autocorrelations experience more variations and are mostly smaller than the value of 0.16. Similar to area 4a autocorrelations between lags 21 and 85, average autocorrelations of area 6 mostly fall below the value of 0.16, but vary within a smaller range compared to area 4a autocorrelations. Figure 2-6 provides a closer view of the average autocorrelations of the three areas between lags 21 and 85. The minimum and maximum value of the average autocorrelations are different between the three cortical areas (0.16 – 0.21, 0.12 – 0.17, 0.13 – 0.18 for area 2, area 4a and area 6, respectively). Additionally, between lags 54 and 85, area 2 autocorrelations remain almost constant, while area 4a autocorrelations again increase to the maximum value of 0.17. Area 6 autocorrelations experience a smaller increase between lags 54 and 85, compared to area 4a autocorrelation.

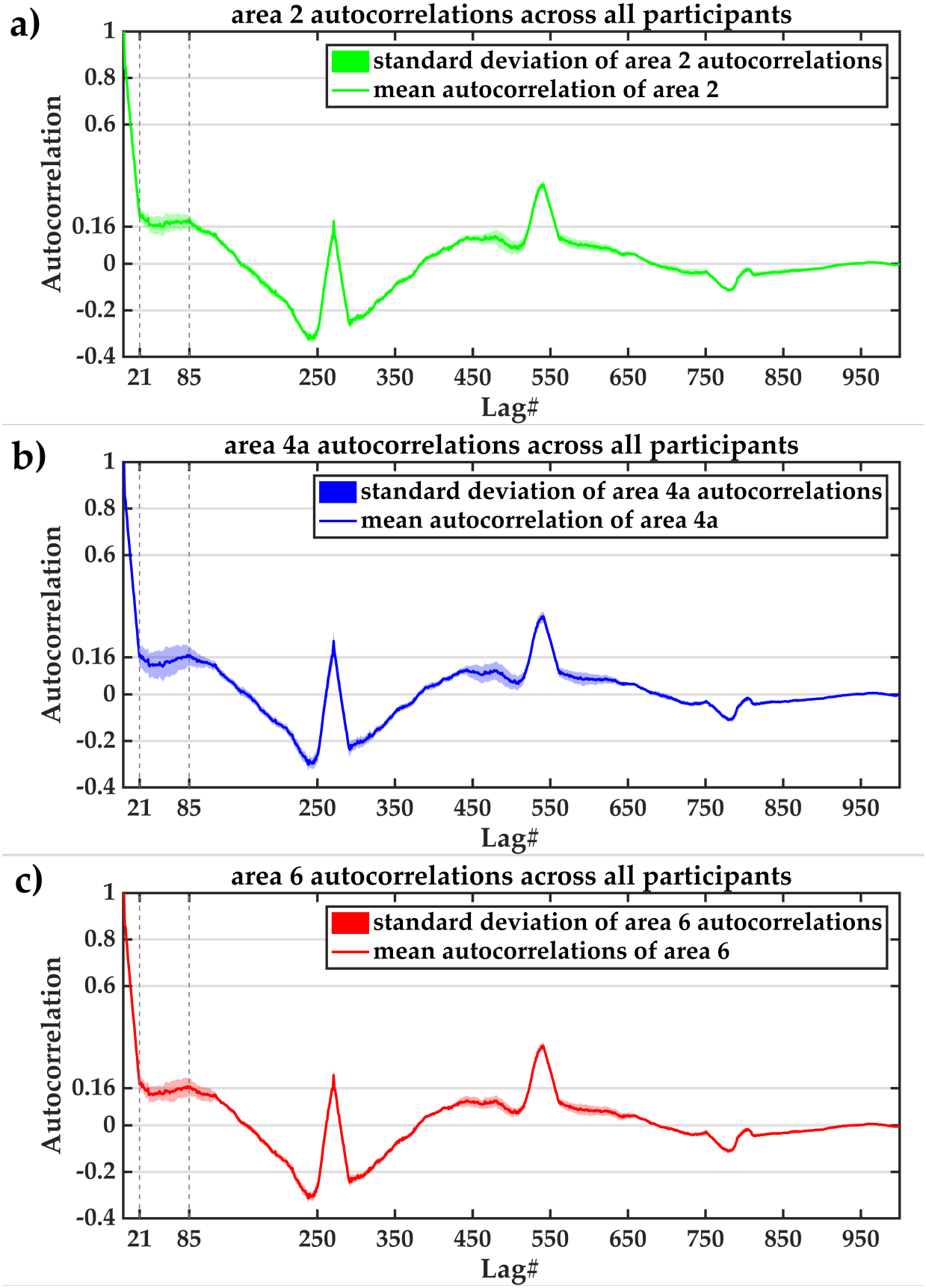

Figure 2-5 Comparison of the normalised autocorrelation patterns of a) area 2, b) area 4a and c) area 6 for six participants. The solid line represents the mean autocorrelation of each area across six participants, and the shaded area corresponds to the standard deviation of the autocorrelations among all participants.

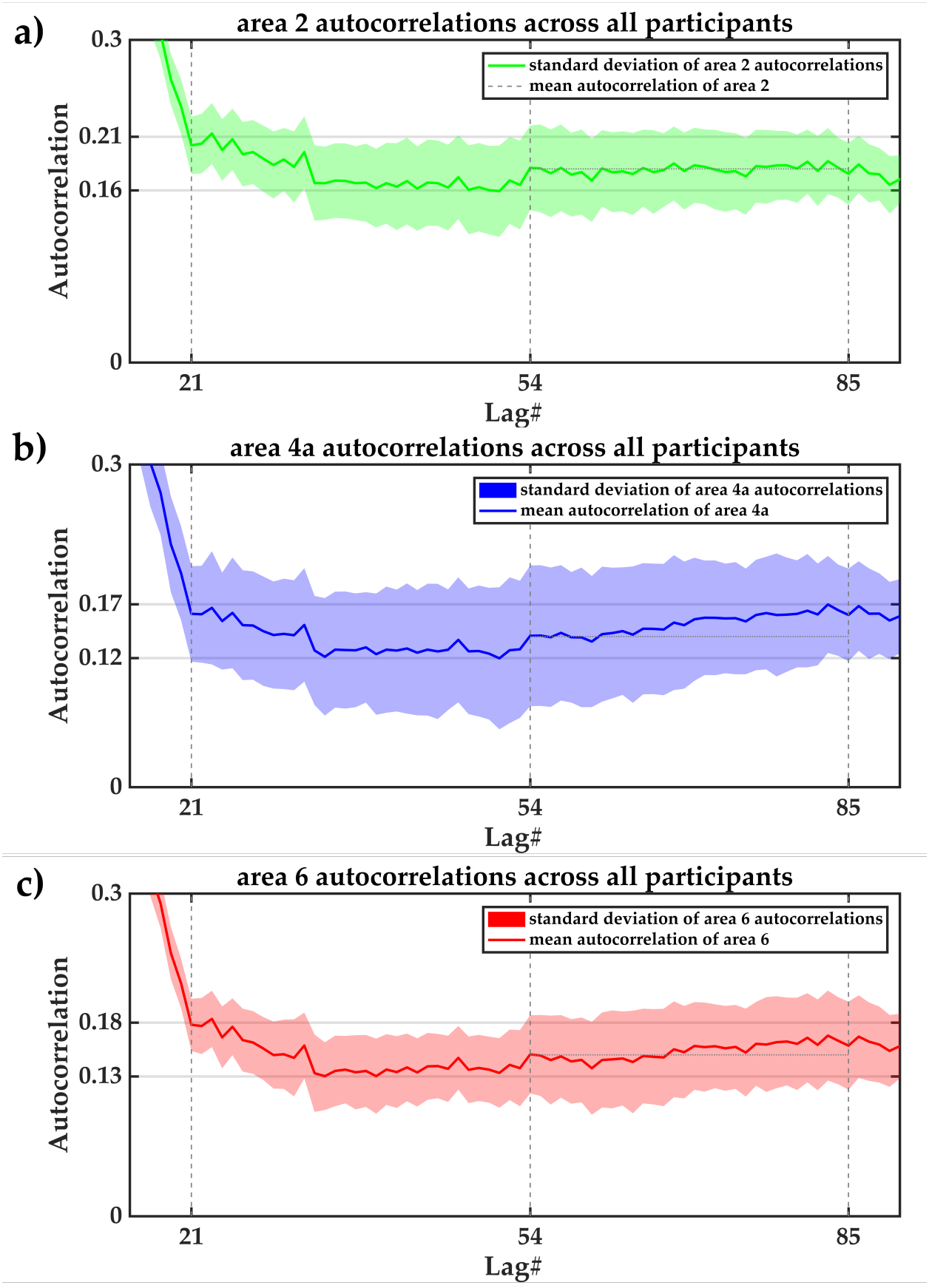

Figure 2-6 An example of the difference in the autocorrelation patterns of a) area 2, b) area 4a and c) area 6 between lags 21 and 85. The solid line represents the mean autocorrelation of each area across six participants, and the shaded area corresponds to the standard deviation of the autocorrelations among all participants.

2.4.3 Interareal Dissimilarity of MRF Residuals

The dissimilarity measurements for six participants are represented in Figure 2-7. Figure 2-7a shows the Euclidean distance from area 2 to area 4a and 6. For all six participants, the distance from area 2 to area 4a is larger than the distance between area 2 and 6. This implies higher dissimilarity between MRF residuals of area 2 and 4a, compared with area 2 and 6. Likewise, for all six participants, Figure 2-7b identifies area 2 as the most dissimilar area to 4a, while area 6 is more similar to area 4a. Figure 2-7c confirms that the dissimilarity between area 6 and 4a is consistently lower for all participants.

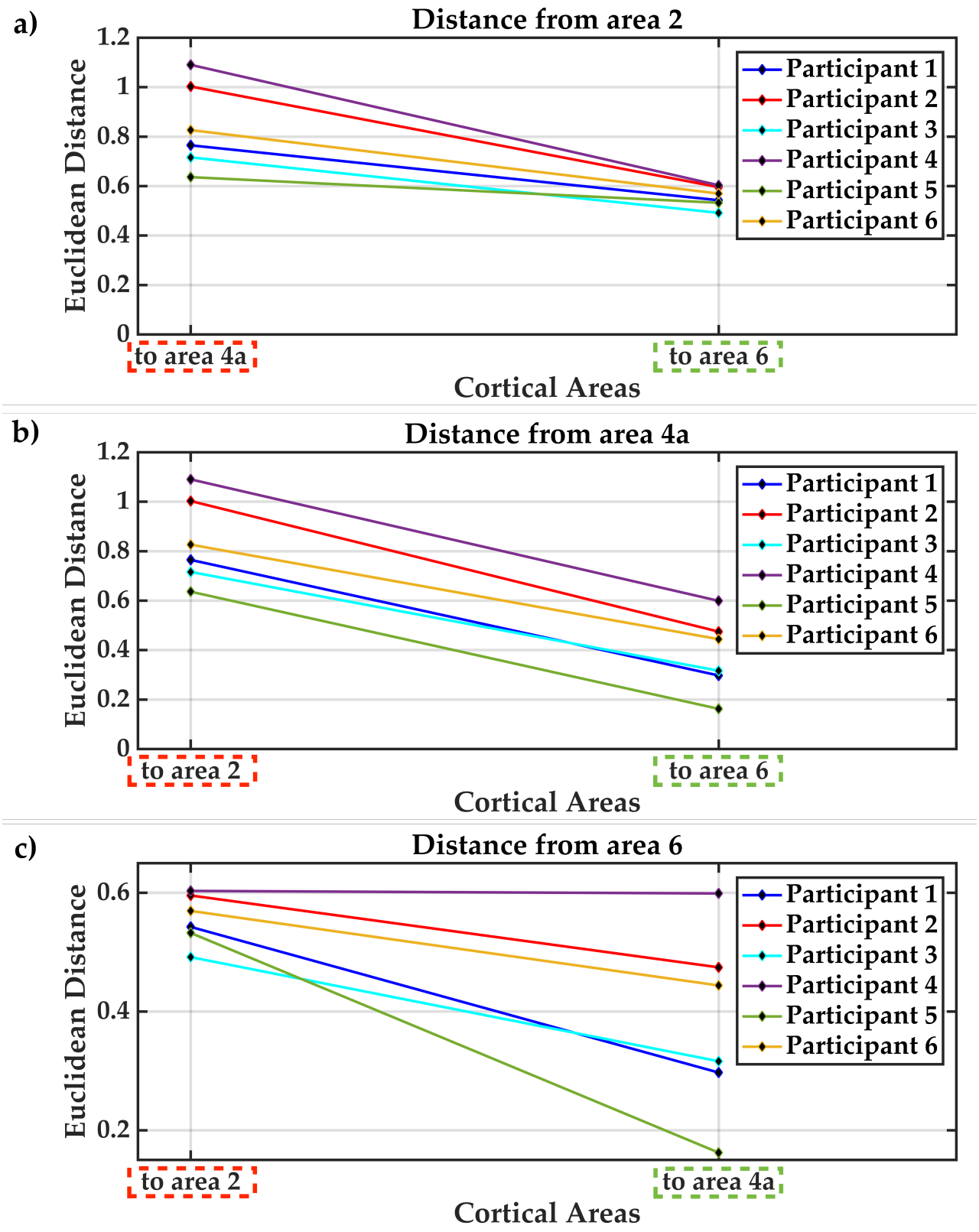

Figure 2-7 The Euclidean distance from a) area 2 to area 4a and 6, b) area 4a to area 2 and 6, c) area 6 to area 2 and 4a for six participants. The maximum (dashed red box) and the minimum (dashed green box) distance values on each diagram identify higher and lower interareal dissimilarity to the target area, respectively.

The significance of the difference between the Euclidean distance values is illustrated with notched box plots in Figure 2-8. The notches of the three box plots do not overlap, meaning

that, with 95% confidence, the medians of the Euclidean distances between the three target areas are significantly different. Additionally, the p-values from the Wilcoxon signed rank test [137] on the distance values confirmed that the difference was statistically significant at $P < 0.05$.

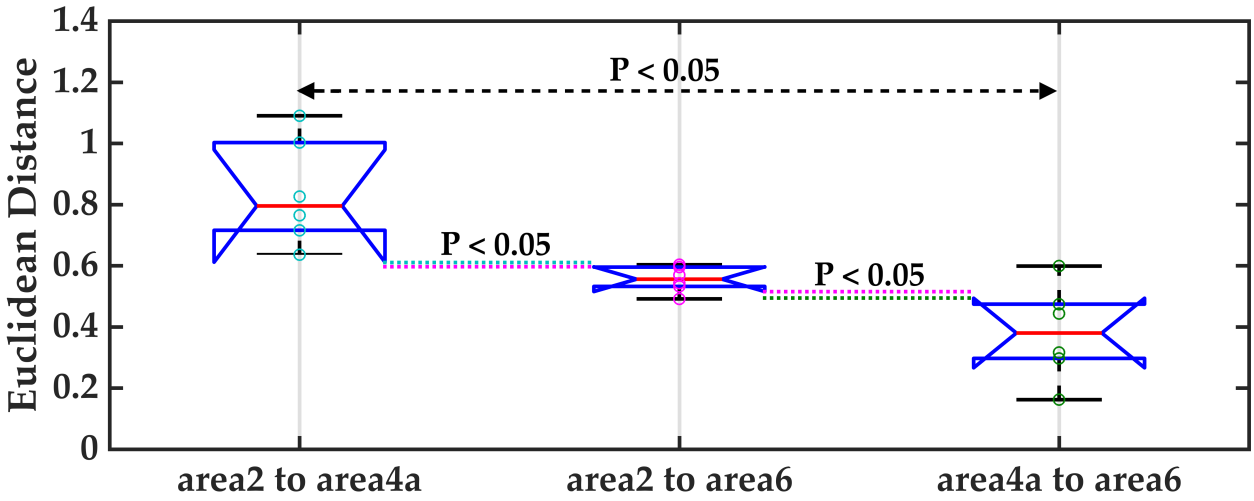

Figure 2-8 Notched box plots of the Euclidean distances between the autocorrelation of the MRF residuals of the three target areas. The distance values between area 2 and 4a are presented with cyan circles, between area 2 and 6 are in magenta, and between area 4a and 6 are in green. The p-values obtained from Wilcoxon signed rank test are also displayed for the difference between the medians of the distance values.

2.5 DISCUSSION

Using the MRF residual analysis framework introduced in this work, we present two key results from the statistical analysis of MRF residuals of three cortical areas. First, we showed significant correlation and non-randomness exists between the MRF residual values of each cortical area (Figure 2-4), demonstrating significant distinction from the properties of a white noise process. Thus, MRF residuals, which theoretically contain no information about the MR relaxometry tissue properties (i.e. T1 and T2*), may have unexplained structure that could reveal more information about tissue architecture. This implies that MR relaxometry tissue properties do not explain tissue characteristics completely. Second, we showed that the unexplained structure present in the residuals can be linked to the microstructural variations in underlying tissue. This was inferred from a) the area-specific patterns in the autocorrelations of the residuals (Figure 2-5 and Figure 2-6), b) statistically significant difference in autocorrelation profile between the three areas (Figure 2-8), c) consistent qualitative between-area similarities across all participants (Figure 2-7), and d) qualitative agreement between the interareal dissimilarity measures of our study (Figure 2-7) and other observer-independent cortical mapping experiments.

According to several microstructural mapping studies, areas 2 and 4 are two areas with conspicuous microarchitectonic distinctions [11, 13, 35, 117, 138]. For example, Geyer, et al. [39] compared these two areas using an observer-independent *ex vivo* cytoarchitectonic method and showed significantly higher dissimilarity between areas 4 and 2 than with other primary somatosensory areas (e.g. areas 3a, 3b and 1). This marked difference has been linked to the thicker cortex, lower cell density, smoother transition from grey matter to white matter [39], larger pyramidal cells [138] and the missing layer IV in area 4 [12, 15] compared to area 2. These two areas also have distinguishable differences in myeloarchitecture (i.e. area 4 is astriate [139], and area 2 is unistriate [140]). Accordingly, myeloarchitectonic studies have also been able to clearly distinguish the two areas on the basis of degree of myelination (higher in area 4 compared to 2) [121] and difference in fibre orientation [62]. In line with these findings, we showed significantly larger dissimilarity between areas 2 and 4a, than between areas 4a and 6 and areas 2 and 6 (Figure 2-8). This would be expected if our method is sensitive to the combined effect of consistently distinctive microstructural tissue components.

Glasser and Van Essen [121] and Cohen-Adad, et al. [62] have reported intermediate myeloarchitectonic dissimilarity of area 6 to areas 2 and 4a. That is, on average, area 6 is observed to have a higher degree of myelination than area 2, while showing lower myelination than area 4a. This may explain smaller distance values between area 6 and areas 2 and 4a (Figure 2-8), compared to the distance between area 2 and 4a.

One main advantage of our framework over other multi-modal MRI microstructural mapping methods is that it was not designed for delineating a limited number of microstructural features of the tissue. Instead, it characterises the non-relaxometry information in the MRF signal residuals collectively, thus may contain information about the ensemble of microscopic tissue components. Consequently, our method may lead to improved accuracy of microstructural tissue characterisation across the cortex, as we believe neglecting the simultaneous effects of multiple microscopic components on the MR signal could be the main concerning source of inaccuracy in most multi-modal MR-based methods. For example, Marques, et al. [116] aimed for independent accurate mapping of iron and myelin contents from a combination of R1, $R2^*$ and QSM measurements through developing a linear model. However, the inconsistency of the resultant maps in some cortical areas across subjects may suggest the presence of other microscopic components contributing to the susceptibility contrast in those areas (e.g. calcium [141]). Therefore, neglecting the

simultaneous effect of all microscopic components on the MR signals may simply challenge the applicability of the multi-modal models across the cortex.

2.5.1 Limitations and Future Directions

We developed a 2D EPI-based MRF sequence for MR fingerprinting data acquisition. The intrinsic limitations of 2D EPI sequence could impose some challenges on our method. Echo-planar imaging suffers from low SNR when high readout bandwidth and high in-plane spatial resolution are used [142]. A relatively high bandwidth (1562 Hz/pixel) was used, with the aim of reducing the minimum TE and TR values and lowering the common EPI-related susceptibility and distortion artefacts. We acquired our MRF images with relatively high in-plane spatial resolution of 1mm to examine the cerebral cortex, which has a 1mm to 4.5mm thickness in humans [15, 143]. The combination of high bandwidth and high in-plane spatial resolution contributed to the low SNR of our MRF images. This may affect interareal dissimilarity measurements in our residual-based processing pipeline, especially between areas with low degree of microstructural dissimilarity. To mitigate possible effects, three repetitions of each MRF slice were acquired using a high field MR scanner (7T).

Future work to cover the entire cerebral cortex requires development of a 3D EPI-based MRF sequence. Besides increasing the SNR, 3D acquisition could also reduce the total acquisition time for a whole brain MRF scan, using partial Fourier sampling and partial parallel imaging along a secondary phase encoding direction [144].

Mis-registration between the MRF scans and SA2RAGE images could result in the use of incorrect $B1^+$ values for MRF dictionary matching in a voxel, resulting in an inaccurate MRF residual. Mis-registration with the atlas could also lead to the inclusion of neighbouring cortical areas. To alleviate this problem, we used MP2RAGE T1w anatomical scans as an intermediate image in a two-level co-registration of $B1^+$ maps and atlas masks with the MRF images. However, the lack of 3D MRF images of the whole brain might affect the accuracy of co-registration between the MP2RAGE and MRF images. Mis-registration is a concern common to multi-modal microstructural mapping [64]. EPI-related susceptibility and geometric distortions also affect registration. Hence our pre-processing procedure also included non-linear registration. EPI distortion correction techniques [145] are likely to further improve realignment accuracy.

The minimum voxel size is a limitation in MR-based microstructural studies [110], especially when studying thinner cortical areas (e.g. < 2mm in the present work). The MRF residuals

of most voxels lying within such areas are more likely to carry some information about the adjacent tissues (e.g. CSF and WM). To minimise the partial volume effect in the present study, voxels with low (i.e. < 90%) GM fraction for each participant were excluded, limiting the application of the proposed method in voxels with high degree of partial volume effect. In a future work, the partial volume effect may be directly formulated in the MRF signal simulations using the method proposed in [10], removing the need to perform separate tissue segmentation, and to exclude voxels with high non-GM fraction. This may also eliminate the need for MRF images with spatial resolutions higher than 1mm, as has been suggested to mitigate partial volume effects in other MRI-based microstructural mapping methods. Although, high resolution images might still be useful for capturing layer-specific cortical variations [34].

Several avenues for enhancing the method could be explored. 3D MRF acquisition with a time-optimised acquisition parameter scheme, and voxel-wise development of the residual analysis framework could allow integration of resultant individualised cortical maps with other types of MR data (e.g. functional data). This method could be more time-efficient and cost-effective than current multi-modal MR-based cortical mapping methods reviewed in [64], especially because there might be no need for separate acquisition of complementary modalities (e.g. phase data of MR signals) and the subsequent data integration through a post-processing procedure.

Finally, it is essential to note that the present work was a proof of concept study for the novel cortical microstructure characterisation approach that was introduced here. Although the results obtained from the small number of subjects were promising and demonstrated the feasibility of using the proposed method for cortical mapping, it is essential to investigate the effectiveness of the present method in a larger population in future work. In terms of examining the inter-subject architectonic variability in the human cerebral cortex, and in regard to statistical inferences, the small sample size examined in this study (i.e. n=6) may not provide us with a strong supporting evidence.

2.6 CONCLUSIONS

Our MRF residual analysis framework identified area-specific patterns in the MRF residual signals of three cortical areas: primary motor cortex (area 4a), premotor cortex (area 6) and primary somatosensory cortex (area 2). Similar patterns of microstructural variations are reported in observer-independent cortical mapping studies. This agreement suggests that

a) MR relaxometry tissue properties do not reflect the underlying tissue characteristics completely, and b) MRF residuals could reflect the microstructural variations between the human brain cortical areas. Additionally, it is likely that MRF signals are affected by a combination of microstructural tissue properties, providing us with a basis for developing a multi-parametric observer-independent microstructural mapping method. Our framework could be further tailored in future studies towards developing a method for voxel-wise microanatomical parcellation of the cerebral cortex in individuals.

Chapter 3 Developing 3D MR fingerprinting residual analysis towards microanatomical characterisation of the whole cerebral cortex in human

3.1 INTRODUCTION

In Chapter 2 we described a new method based on MR fingerprinting (MRF) framework which distinguished between three cortical areas (Brodmann area (BA) 2: primary somatosensory cortex, BA4: primary motor cortex and BA6: premotor cortex). Particularly, the MRF residual analysis framework demonstrated the presence of information in MRF signals complementary to MR relaxometry (T1, $T2^*$), a potentially useful finding for accurate *in vivo* human cortical parcellation. Furthermore, adaptation of MRF framework mitigated the challenge of acquisition, integration, and interpretation of the data from multiple MR contrasts, which is a concern common in most quantitative multi-modal MRI cortical mapping methods [64]. Despite the promising findings, the MRF residual-based cortical mapping method presented in Chapter 2 was a proof-of-principal study and had several limitations.

The MRF residual-based cortical mapping method presented in Chapter 2 utilised a 2D single-shot gradient-echo EPI-based [142] MRF sequence for MRF signal acquisitions. The successful use of cartesian EPI readout for developing an MRF sequence (EPI-MRF) has also been demonstrated by Rieger, et al. [69], aiming to provide an alternative for the non-cartesian readouts (e.g. spiral [10] and radial [71]) used in other MRF studies. EPI-MRF could not achieve an efficient k-space sampling comparable to the spiral-based MRF sequences, due to the limited undersampling options available [69]. On the other hand, compared to the non-cartesian readouts (e.g. spiral), EPI could benefit from more robustness to system imperfections (such as gradient deviations and the effect of eddy currents on trajectory accuracy) [146], which may affect MRF parameter mapping accuracy [69].

While the EPI-based MRF residual analysis study presented in Chapter 2 benefited from the inherent characteristics of the cartesian EPI readout and established the feasibility of performing microstructural characterisation of the grey matter, the single-slice (2D) MRF acquisition imposes several limitations on the extended cerebral cortex coverage. Improved spatial coverage using single-slice acquisition could become especially challenging in microstructural mapping applications that require high spatial resolutions [34]. Achieving higher spatial resolution in the slice direction would require acquisition of larger number of slices, which linearly increases the total acquisition time of conventional single-slice acquisition sequences due to the need for full magnetization recovery before the acquisition of a new slice [144].

Several studies have investigated different methods for optimising the acquisition time in MRF applications with large spatial coverage. Amthor, et al. [147] proposed a method that could reduce the magnetization recovery time required between acquisition of multiple slices, using a non-relaxed steady state magnetization as the initial spin state of the fingerprints. Their method provided a generalisable time optimisation approach that is applicable to all types of k-space sampling methods used in MRF. However, the lower SNR resulted from the use of non-relaxed initial spin state, could affect the MRF parameter mapping accuracy and precision [147]. To further improve the efficiency of MRF acquisitions with large spatial coverage, simultaneous multi-slice (SMS [148]) MRF studies have benefited from variable phase encoding techniques for simultaneous excitation of multiple slices [75, 149]. However, the achievable acceleration factor in SMS-MRF is limited to 3, due to degraded MRF parameter mapping precision as a consequence of incomplete slice signal separation and lower SNR at acceleration factors higher than 3 [149]. Additionally, the acceleration factor of 3 in SMS-MRF could be achieved at the cost of acquiring additional preparation data, use of computationally expensive complex slice separation algorithms [149], and increased specific absorption rate (SAR) [150]. To overcome these issues Rieger, et al. [68] developed a slice-interleaved EPI-MRF sequence and achieved the acceleration factor of 4, without compromising the MRF parameter quantification accuracy. However, slice-interleaved acquisitions do not allow acquisition of continuous imaging volumes. Further improvements could be achieved using continuous 3D volumetric sampling schemes, resulting in higher through-plane resolutions and enhanced slice profiles [68, 73, 151], while maintaining high MRF parameter mapping accuracy and precision due to high SNR [73, 151]. The 3D volumetric acquisitions could achieve high acceleration factors, as they enable the application of k-space undersampling techniques (e.g. partial Fourier sampling and partial parallel imaging) along a secondary phase encoding direction (k_z) [73, 144, 151].

The purpose of this study was to explore the feasibility of extending the spatial coverage of our MRF residual analysis framework (Chapter 2), within a clinically acceptable time. We investigated this through adaptation of the 3D EPI sequence developed previously by Poser, et al. [144], to benefit from the above-mentioned characteristics of 3D volumetric acquisition schemes and EPI readouts at the same time, for our MRF signal acquisitions. Furthermore, the possibility of total MRF acquisition time optimisation was examined empirically, through reducing the total number of MRF baseline images.

3.2 METHODS

3.2.1 Subjects

Six volunteers (one male and five females) participated in a two hour-long MRI scan session. Participants were healthy individuals aged between 27 years and 35 years with no history of neurological disease. Participants were provided with an overview of the experiment and signed a written consent form prior to the scan. Each participant underwent two scans separated by a 15-minute break. A whole-brain 3D EPI-based MRF scan was performed in both sessions. In the first session, we also performed a whole-brain 3D SA2RAGE and an MP2RAGE scan.

3.2.2 Regions-of-Interest

We extracted three cortical areas from the Juelich cyto and myeloarchitectonic histological atlas of the human brain [41, 122]: primary somatosensory cortex (BA2), primary motor cortex (BA4a) and premotor cortex (BA6). These cortical areas were chosen on the basis that their microstructural similarity has been established quantitatively and qualitatively in many observer-independent cortical mapping studies [13, 33, 35], providing a means of validation for the inter-areal similarities measured in the present study.

Note that the atlas provides probability masks for each area, representing the interindividual differences in the spatial location of each area. A voxel with high probability value indicates that there is a higher chance that the corresponding voxel in the MR image of a new individual would belong to the area of interest. In this study, we excluded the voxels with probability values of less than 80 percent from the atlas probability masks. All regions-of-interest (ROI) masks were then binarized using FSL [123], such that the value of 1 in the binarized mask represents the voxels with probability of higher than 80 percent.

3.2.3 MRI Acquisition

The scan protocols were approved by the local ethics committee, and were performed at the Centre for Advanced Imaging, The University of Queensland, on a 7T whole-body MRI research scanner (Siemens Healthcare, Erlangen, Germany) using a 32-channel head coil (Nova Medical, Wilmington, Massachusetts). B_0 shimming was performed at the beginning of each scan session to reduce susceptibility effects.

MRF acquisition

A 3D EPI [144] sequence was adapted to be utilised for acquiring 1000 baseline MRF images with the following parameters:

TR = 41 - 99 ms (Figure 3-2), FA = 10 - 77° (Figure 3-1), TE = 12 - 48 ms (Figure 3-2), Partial Fourier Phase = 6/8, voxel size = 1.4 × 1.4 × 1.4 mm, and matrix size = 142 × 142 × 88. We used GRAPPA parallel imaging [127] in both in-plane (with acceleration factor =3 and reference lines = 36) and through-plane phase encoding directions (with acceleration factor =2 and reference lines = 12). Fat Saturation was used to reduce the common chemical-shift artefacts observed in EPI sequences [152]. Each MRF scan was acquired twice, in two separate sessions, to increase SNR through averaging.

MRF acquisition patterns

The half-sinusoidal flip angle pattern used for the MRF acquisitions (Figure 3-1) was adopted from [79], adding the abrupt flip angle changes (0°-40°-50°-60°-0°) at the final baseline images to increase the sensitivity of MRF signals to $B1^+$ variations [153].

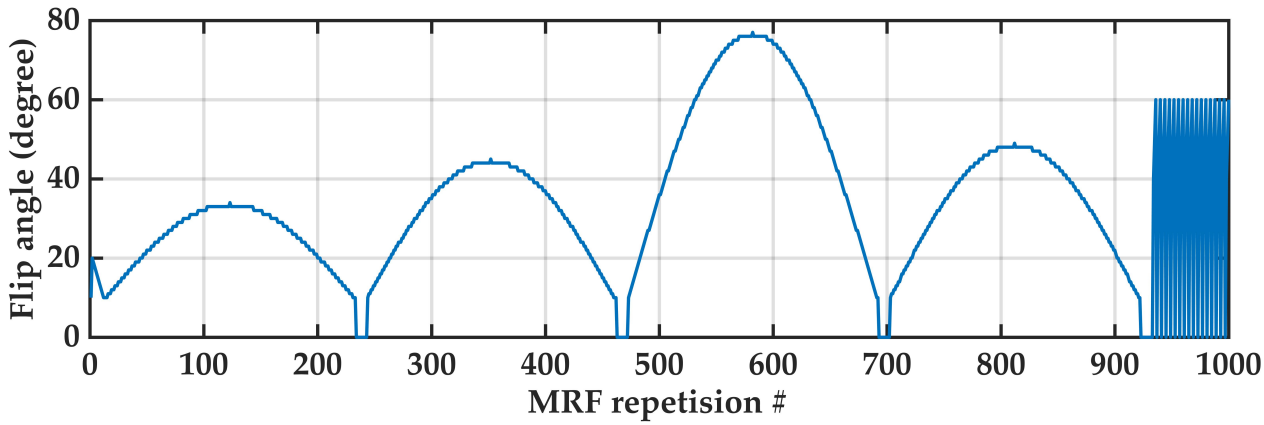

Figure 3-1 The pseudo-randomised pattern of flip angles, used to acquire the 3D MRF images.

We also used pseudo-randomised patterns suggested by Rieger, et al. [69] for TE variations (Figure 3-2), to improve SNR as a result of the higher distribution of TE values at the shorter values. This also allowed optimising the total MRF acquisition time by setting the TR values to the minimum possible value for each TE at each MRF repetition. The alternating pattern has also been shown to increase sensitivity of MRF signals to T1 and $T2^*$ variations [69], leading to more accurate estimation of these tissue properties.

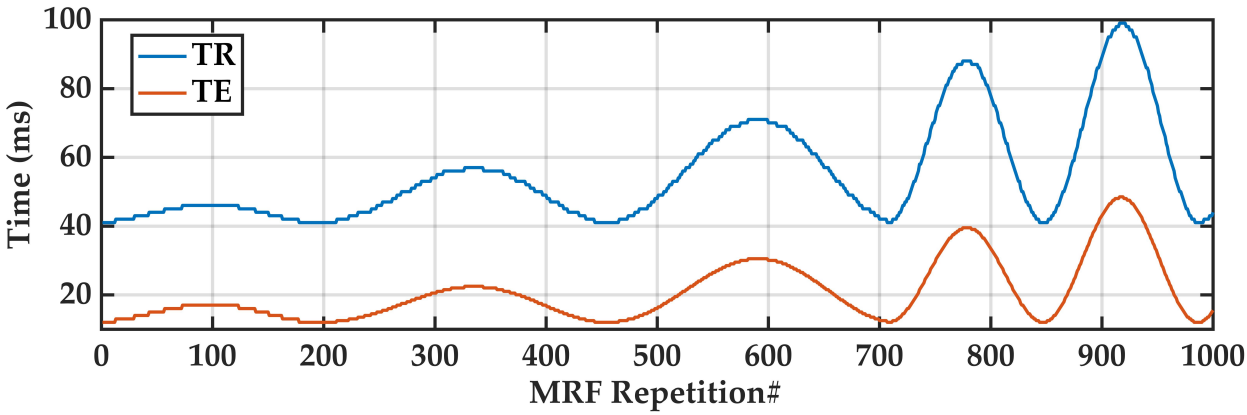

Figure 3-2 The pseudo-randomised pattern of repetition time (TR) and echo time (TE), used to acquire the 3D MRF images.

B1⁺ maps

A 3D Saturation-prepared with 2 Rapid Gradient Echoes (SA2RAGE) sequence [124] was utilised to acquire the whole-brain transmit magnetic field ($B1^+$) map of the brain, for $B1^+$ inhomogeneity correction on the MRF signals [154]. When simulating the MRF signal evolutions for generating the MRF dictionary, $B1^+$ values were used as a linear scaling factor to calculate actual flip angles based on the nominal flip angle values (Figure 3-1).
The SA2RAGE acquisition parameters were as follows: TR = 2400 ms, TE = 0.95 ms, $FA_{1/2}$ = 6°/10°, voxel size = 4 × 4 × 4 mm, and matrix size = 48 × 58 × 64.

T1-weighted images

We acquired 3D T1-weighted images of each participant, using a prototype Magnetization Prepared 2 Rapid Acquisition Gradient Echoes (MP2RAGE) sequence [125]. The acquired T1-weighted images were used to create gray matter masks of each individual and to transform the Juelich atlas masks from the MNI-152 standard space to the MRF native space. The MP2RAGE acquisition was run with the following parameters: Repetition time (TR) = 6000 ms, echo time (TE) = 3.97 ms, inversion time $TI_{1/2}$ = 800 ms/2700 ms, flip angle $FA_{1/2}$ = 4°/5°, voxel size = 1 × 1 × 1 mm, and matrix size = 222 × 240 × 144.

3.2.4 Image Processing

Skull-stripping was first performed on all MRF, T1-weighted and $B1^+$ images, using FSL BET [129], to obtain higher brain tissue co-registration accuracy between these images.

To mitigate the effects of head motion during the long MRF scans, we linearly co-registered (using FSL FLIRT [130, 131] with 6 degrees of freedom (DOF)) all the 1000 MRF 3D

volumes in each MRF scan session, separately. Subsequently, we linearly registered (using FSL FLIRT with 6 DOF) the MRF images of the second scan session to the MRF images of the first scan session. Finally, we calculated the average images between the MRF images of the two sessions.

The ROI binary masks were transformed from the MNI-152 standard space to the MRF native space using a two-level process. First, ROI binary masks were non-linearly registered (FSL FNIRT [132]) to the MP2RAGE T1-weighted image for each individual. Subsequently, ROI masks were linearly transformed from the MP2RAGE native space to the MRF native space.

We then used MP2RAGE T1-weighted images to create the individual's gray matter masks, using *fsl_anat* tool [155]. The *fsl_anat* pipeline includes enhanced bias-field correction, which improves tissue type segmentation accuracy. The gray matter mask of each individual was then used to extract the individual-specific portion of the transformed binary ROI masks.

3.2.5 MRF Residual Analysis

MRF residual analysis was performed as described in Chapter 2. The MRF residual signal for each voxel of interest was calculated as the difference between the measured MRF signal and the best match from the MRF dictionary.

The MRF dictionary was generated off-line in MATLAB and Statistics Toolbox Release 2018b (The MathWorks, Inc., Natick, Massachusetts, United States) using Bloch equation simulation of the magnetization behaviour on the following range of T1, $T2^*$ and $B1^+$ parameters: T1= 100 ms – 1 s in steps of 10 ms, 1 – 2s in steps of 20 ms, 2 – 3s in steps of 30 ms, 3 – 4s in steps of 40 ms, and 4 – 5 s in steps of 50 ms; $T2^*$= 15 – 20 ms in steps of 2 ms, 20 – 40 ms in steps of 3 ms, 40 – 200 ms in steps of 5 ms, and 200-350 ms in steps of 10 ms; $B1^+$= 0.4 – 1.4 in steps of 0.05. Dictionary matching was then performed through finding the maximum inner product of the measured and the simulated dictionary MRF signals.

The MRF signal residual of each voxel was statistically characterised by its normalised autocorrelation, to i) examine deviation of MRF residuals from the white noise distribution (using white noise test), and ii) statistically measure the dissimilarity between MRF residuals of the target cortical areas (using the Euclidean distance between autocorrelations of the areas).

3.2.6 MRF Acquisition Time Optimisation

Although we used k-space undersampling methods (GRAPPA parallel imaging and partial Fourier) to increase the time efficiency of our MRF acquisitions, the proposed number of baseline MRF images (1000 3D volumes of 88 slices), and the TR acquisition pattern (Figure 3-2) would lead to the total acquisition time of about 42 minutes. Long acquisition time would affect the participants comfort, increasing the likelihood of motion artefacts resulted from the participants movements during the scan.

In this study, we opted to investigate the feasibility of optimising the MRF acquisition time empirically. Accordingly, we first performed MRF residual analysis on the 1000 time point MRF signals to explore the feasibility of extending the spatial coverage of the method presented in Chapter 2. We then investigated the feasibility of reducing the MRF acquisition time through decreasing the total number of MRF baseline images, without compromising the MRF residual distinction between the regions of interest.

Defining the optimal number of baseline MRF images required certain considerations. First, several studies have proposed different MRF acquisition parameter profiles, aiming to improve the quantification performance of the MRF framework [69]. Consequently, the MRF optimisation studies usually maintain the original acquisition parameter patterns. Second, it has been shown that reducing the number of baseline MRF images may lead to losing useful information from the MRF signal, therefore compromising the performance of tissue parameter mapping. Therefore, usually a trade-off is sought between the number of baseline MRF images (or, MRF acquisition time) and the parameter of interest (e.g. tissue property quantification accuracy).

Accordingly, in this study, we proposed an empirical approach based on the 1000-time point MRF data (using the average of the MRF images acquired in two separate scan sessions) to find an optimal point (i.e. optimal number of MRF residual signal time points per voxel) such that *i*) the overall pattern of MRF acquisition parameters, and *ii*) the amount of information present in the MRF residual signal would experience minimum possible change, compared to the 1000-time point MRF residual signals.

Maintaining the MRF acquisition profiles

To meet the first requirement, we subsampled the 1000-time point MRF acquisitions by dropping out every n^{th} MRF repetition number, starting from n=10 down to n=2. Subsequently, we continued the subsampling process by including every m^{th} MRF repetition

number, where $3 \leq m \leq 10$. Figure 3-3 illustrates the difference between the two parts of the subsampling process.

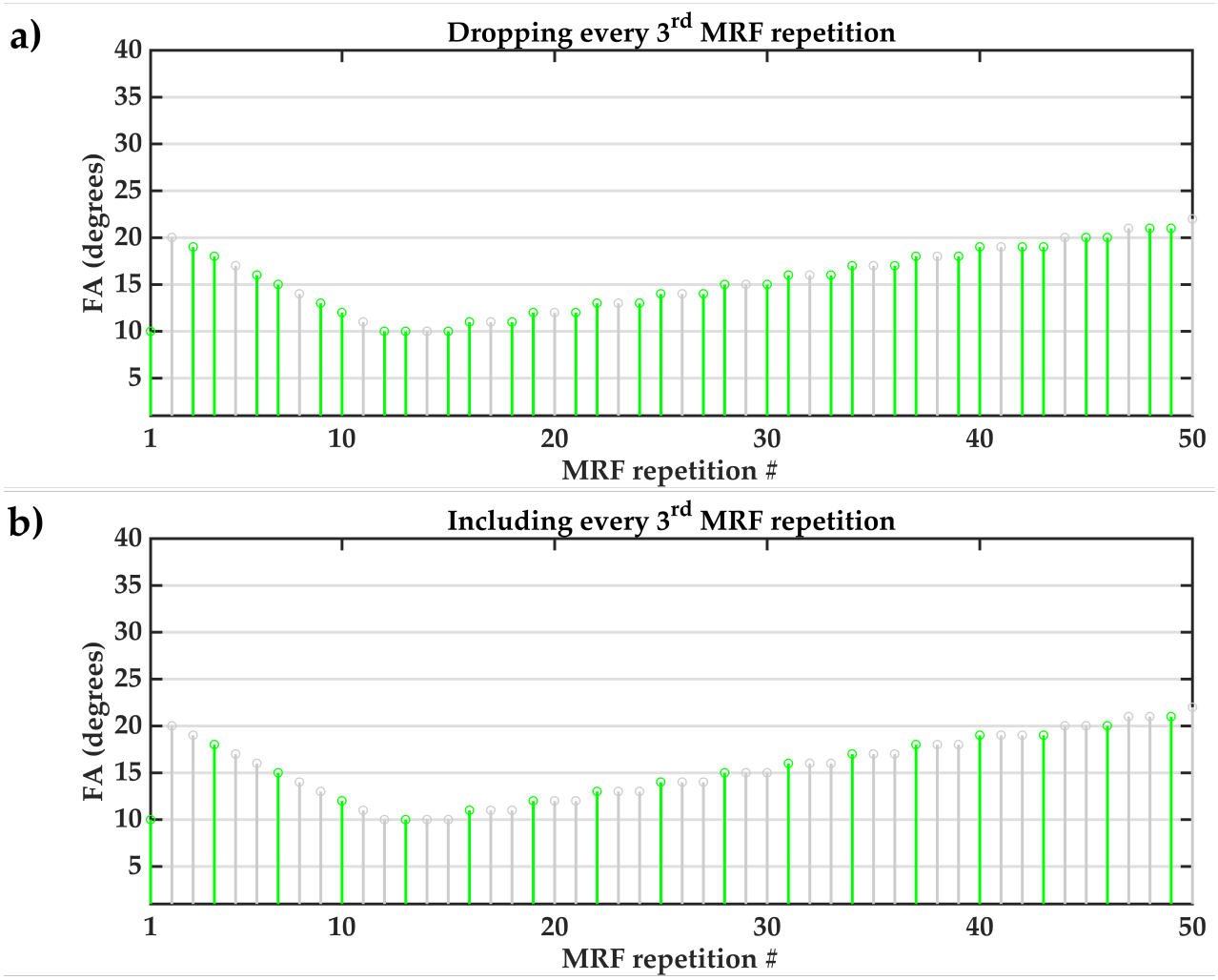

Figure 3-3 Two representative subsampling steps of the MRF acquisition optimisation process, where we a) drop out every 3rd, and b) include in every 3rd MRF repetition numbers of the acquisition parameter profiles. The green and gray time points indicate the MRF repetition numbers that have been included, and excluded at the specified optimisation step, respectively.

Figure 3-4 compares the MRF acquisition parameter (flip angles, repetition time and echo time) profiles of the two subsampling steps presented in Figure 3-3, demonstrating that the proposed subsampling scheme preserves the overall pattern of the acquisition parameters during the optimisation process. Note that the patterns illustrated in Figure 3-4 are both similar to the original pattern of acquisition parameters as depicted in Figure 3-1 and Figure 3-2.

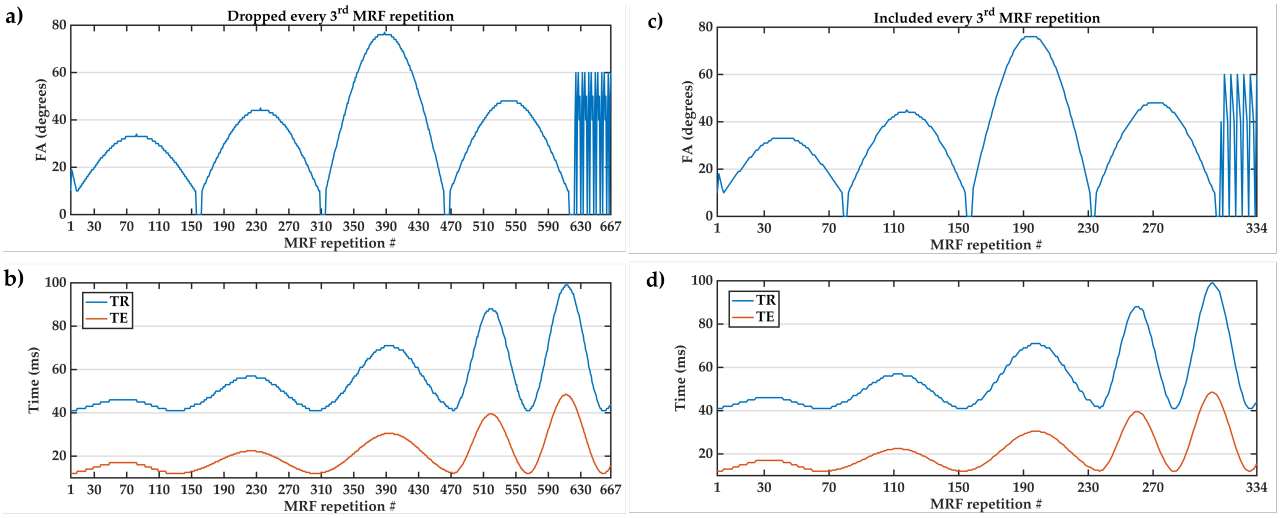

Figure 3-4 The MRF acquisition parameter profiles of the subsampling step at which a, b) we dropped out every 3rd, and c, d) we included every 3rd MRF repetition number.

Preserving the MRF residual signal information

To compare the amount of information present in the MRF residual signals between the subsampling steps, we calculated the mean squared error (MSE) between the measured MRF signals and their best match from the MRF dictionary, for all voxels of interest from all participants. A statistical test was then performed to determine if there was a significant difference between the MSE of the MRF residuals at the specified subsampling step and the original 1000-time point acquisition. The subsampling steps at which no significant change was observed in the MSE of the MRF residuals (compared to the original MRF acquisition with 1000 samples), could theoretically preserve the amount of information available in the 1000-time point MRF residuals, thus not compromising the separability of the MRF residuals of the selected cortical areas.

To validate if the suggested optimal point could actually lead to distinguishing the distinctions between MRF residuals of the selected cortical areas, we repeated the MRF residual analysis as described above on the residual signals subsampled with the suggested optimal pattern.

Simulating MRF parameter quantification

Using fewer number of MRF repetitions could degrade the MRF parameter quantification accuracy, thus affecting the MRF residuals. To investigate this effect on the subsampled MRF signals in this study, we performed an MRF parameter quantification simulation as described below.

For a range of tissue properties (T1= 1600 – 2200 ms, $T2^*$= 20 – 60 ms) we simulated two test sets of MRF signals with 1000 and *n* time points, where *n* was the optimal subsampling step identified in the optimisation process described above. We then generated two MRF dictionaries with equal number of time points as in the two test sets, using the full range of T1, $T2^*$ values as described above. Dictionary matching was performed on both MRF signal test sets, and tissue properties were derived accordingly. The fit accuracy was then measured by calculating the relative error for T1 and $T2^*$ estimations as follows:

$$T1\ relative\ error\ = \frac{T1_{actual} - T1_{estimated}}{T1_{actual}} * 100$$

, where $T1_{actual}$ and $T1_{estimated}$ represent the actual T1 value of the test set MRF signal, and the T1 value derived from the MRF dictionary for the test set signal, respectively. The relative error for $T2^*$ was calculated similarly.

Note that to probe the effect of different SNR values on the fit accuracy of the subsampled MRF signals, we applied additive white gaussian noise with a range of SNR values (5 - 30) on both test set MRF signals.

Finally, we compared the relative errors of the tissue properties between the two test sets, to examine if the subsampling step would affect the MRF parameter quantification accuracy significantly, when compared with the original 1000 time point MRF acquisition.

3.3 RESULTS

3.3.1 White Noise Test on MRF Residuals

Figure 3-5 illustrates the comparison between the autocorrelation distribution of the MRF residual signals of areas 2, 4a and 6 for two participants, and the Gaussian white noise autocorrelation distribution. The autocorrelation of the MRF residuals of the three areas exceeds the 95% confidence interval of the white noise autocorrelation distribution at several lag numbers, demonstrating significant non-randomness ($P<0.05$) between the autocorrelations for each area. This suggests significant difference between the MRF residuals of each area and a white noise process. Similarly, significant difference was observed between autocorrelations of the MRF residuals of the three areas and the autocorrelation distribution of Gaussian white noise, for all other participants.

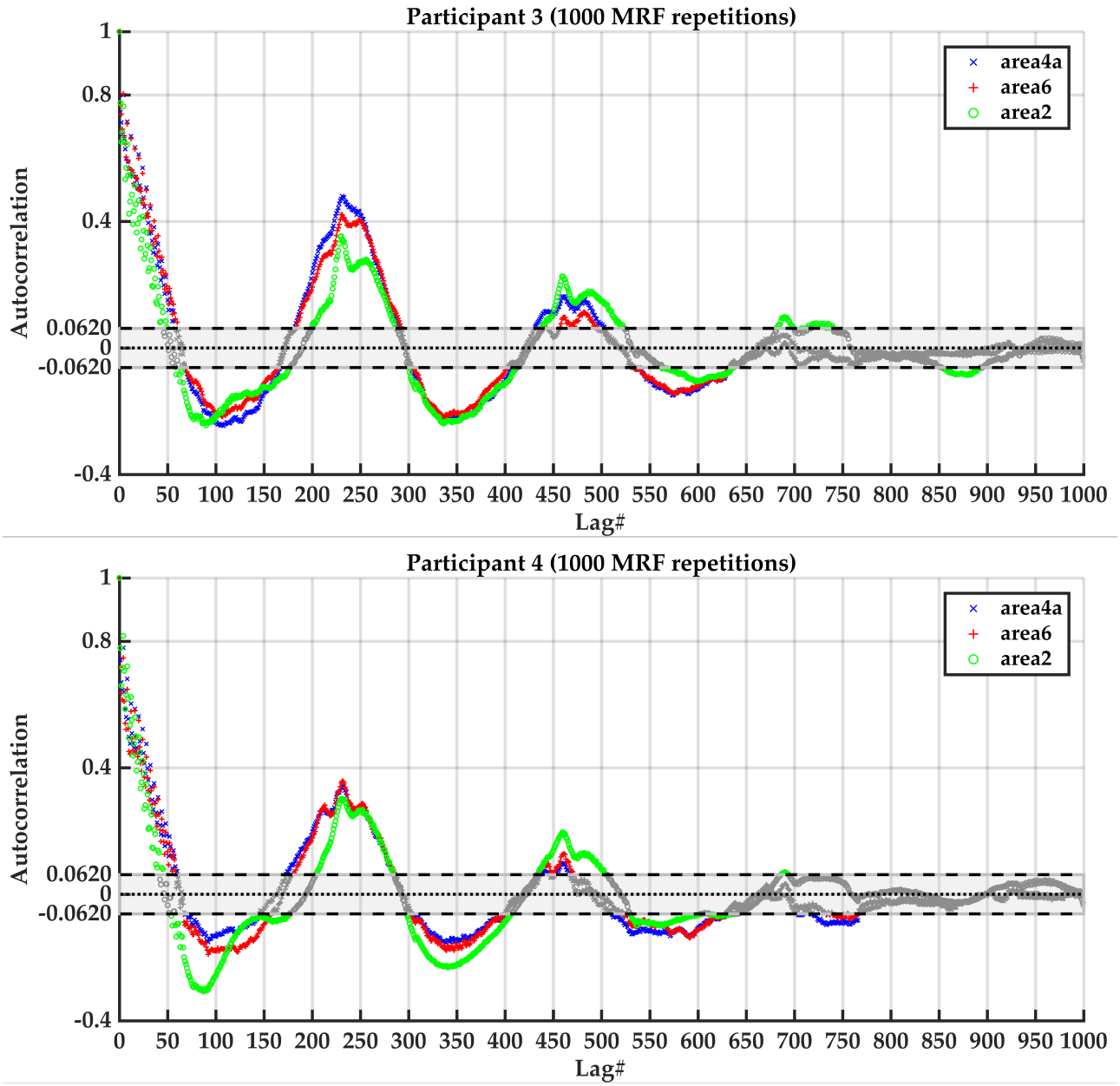

Figure 3-5 Normalised autocorrelation of the MRF residuals of area 4a (blue), area 6 (red) and area 2 (green) for two representative participants overlaid on the 95% confidence intervals (±0.062) of a Gaussian white noise autocorrelation distribution. Autocorrelation values that fall between the 95% confidence intervals are greyed out, indicating their insignificance when compared with the white noise autocorrelation distribution.

3.3.2 Area-specific MRF residuals

The mean and standard deviation of the MRF residual autocorrelations for each area, across six participants, are depicted in Figure 3-6. Comparing the autocorrelation profiles between the three target areas revealed the presence of patterns, as a function of the lag number, which were specific to each cortical area. For example, in Figure 3-7 a closer view of the autocorrelation values of each area, between lags 62 and 185, visualises some of these differences. In Figure 3-7a we observe that the autocorrelations of area 2 fall slightly under

the value of -0.2 before the lag number 102. Then, at lag number 102, area 2 autocorrelations reach -0.2 again, before they increase to 0 at lag number 185. In contrast, area 4a and 6 autocorrelations (Figure 3-7b, c) stay above the value of -0.2 between lags 62 and 185, and then cross the value of 0 before the lag number 185. Additionally, Figure 3-7 shows the higher similarity between autocorrelation patterns of area 4a and 6 (Figure 3-7b, c), compared to area 2 autocorrelations (Figure 3-7a). Although, the area 6 autocorrelations are closer to the value of -0.2 between lags 62 and 185, compared to the area 4a autocorrelations. Consequently, these characteristic patterns of autocorrelations of the MRF residuals may be able to distinguish between the cortical areas of interest.

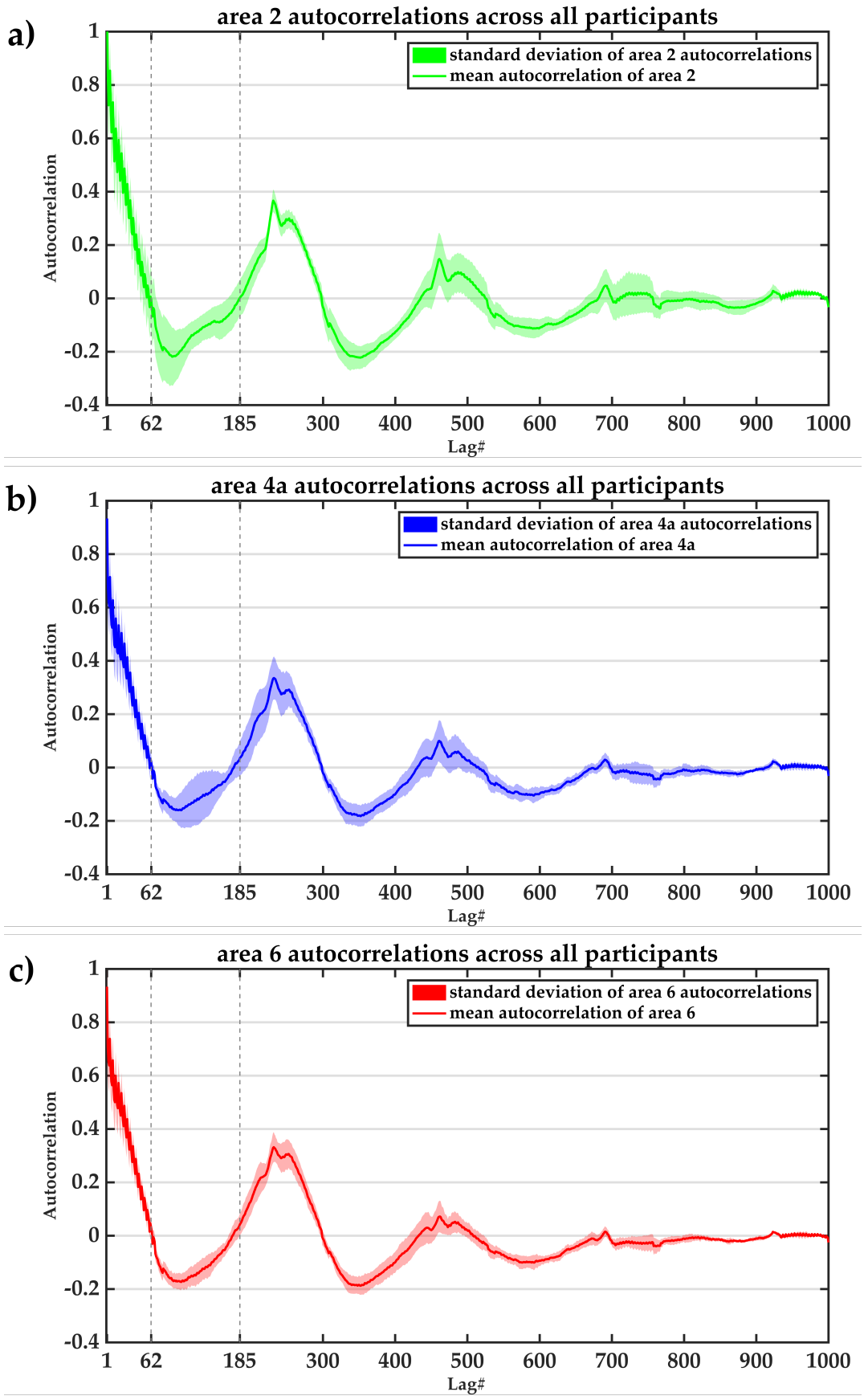

Figure 3-6 Comparison of the normalised autocorrelation patterns of a) area 2, b) area 4a and c) area 6 for six participants. The solid line represents the mean autocorrelation of the MRF residual signal of each area across six participants, and the shaded area corresponds to the standard deviation of the autocorrelations among all participants.

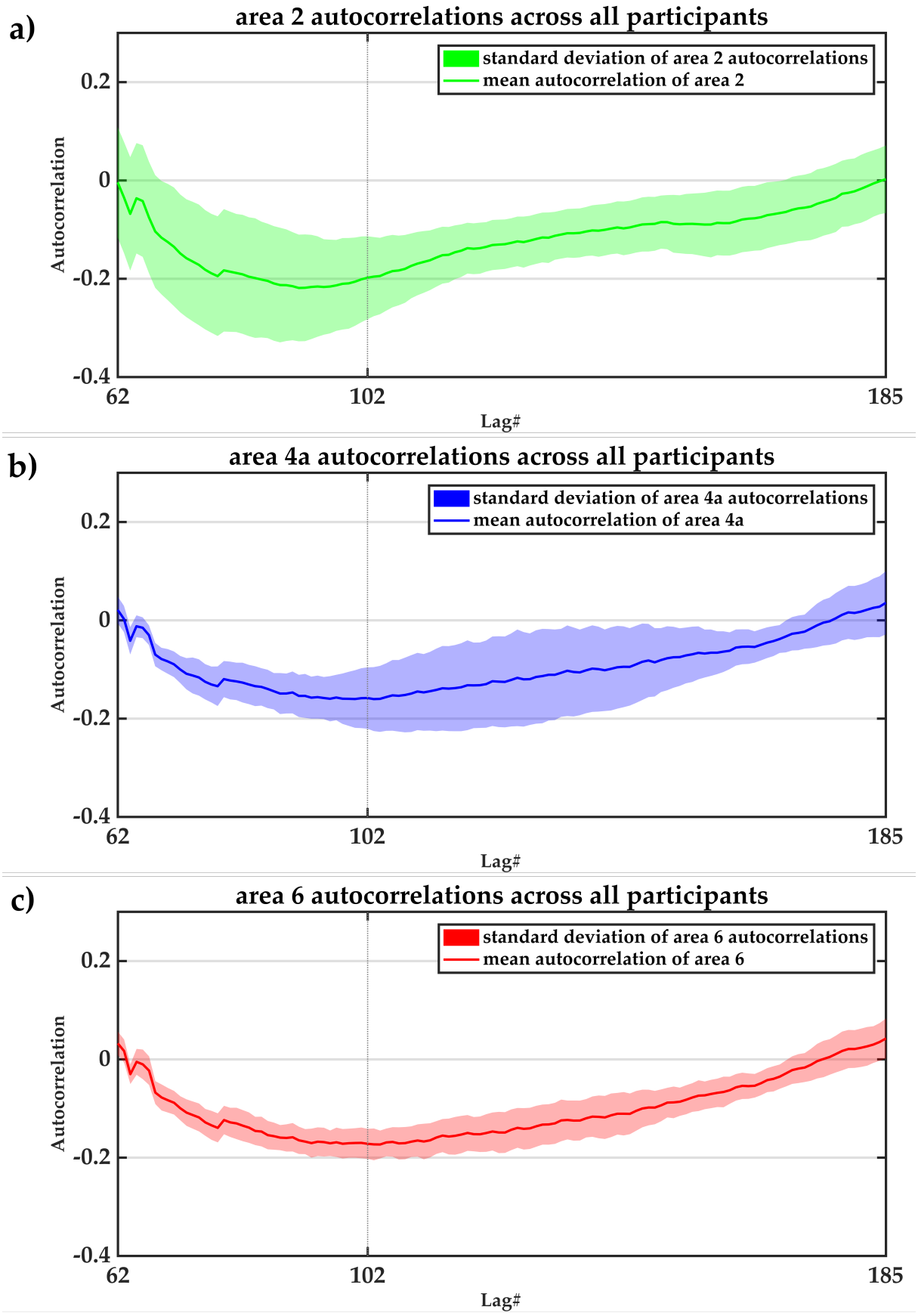

Figure 3-7 An example of the difference in the autocorrelation patterns of a) area 2, b) area 4a and c) area 6 between lags 62 and 185. The solid line represents the mean autocorrelation of each area across six participants, and the shaded area corresponds to the standard deviation of the autocorrelations among all participants.

3.3.3 Areal Dissimilarity of MRF Residuals

The Euclidean distances between the MRF residuals autocorrelations of the cortical areas of interest are displayed in Figure 3-8, for all six participants. The Euclidean distances demonstrate the dissimilarity between the autocorrelation profiles of three cortical areas, for each participant. Figure 3-8a compares the distance from area 2 to areas 4a and 6. For all six participants, larger Euclidean distance between area 2 and 4a shows higher dissimilarity between MRF residuals of these two areas, compared with the dissimilarity between area 2 and 6. Similarly, Figure 3-8b confirms higher dissimilarity between areas 4a and 2, compared with the dissimilarity between area 4a and 6, for all six participants. Figure 3-8c, which compares the distance from area 6 to areas 2 and 4a, also confirms that area 6 is more similar to area 4a than to area 2.

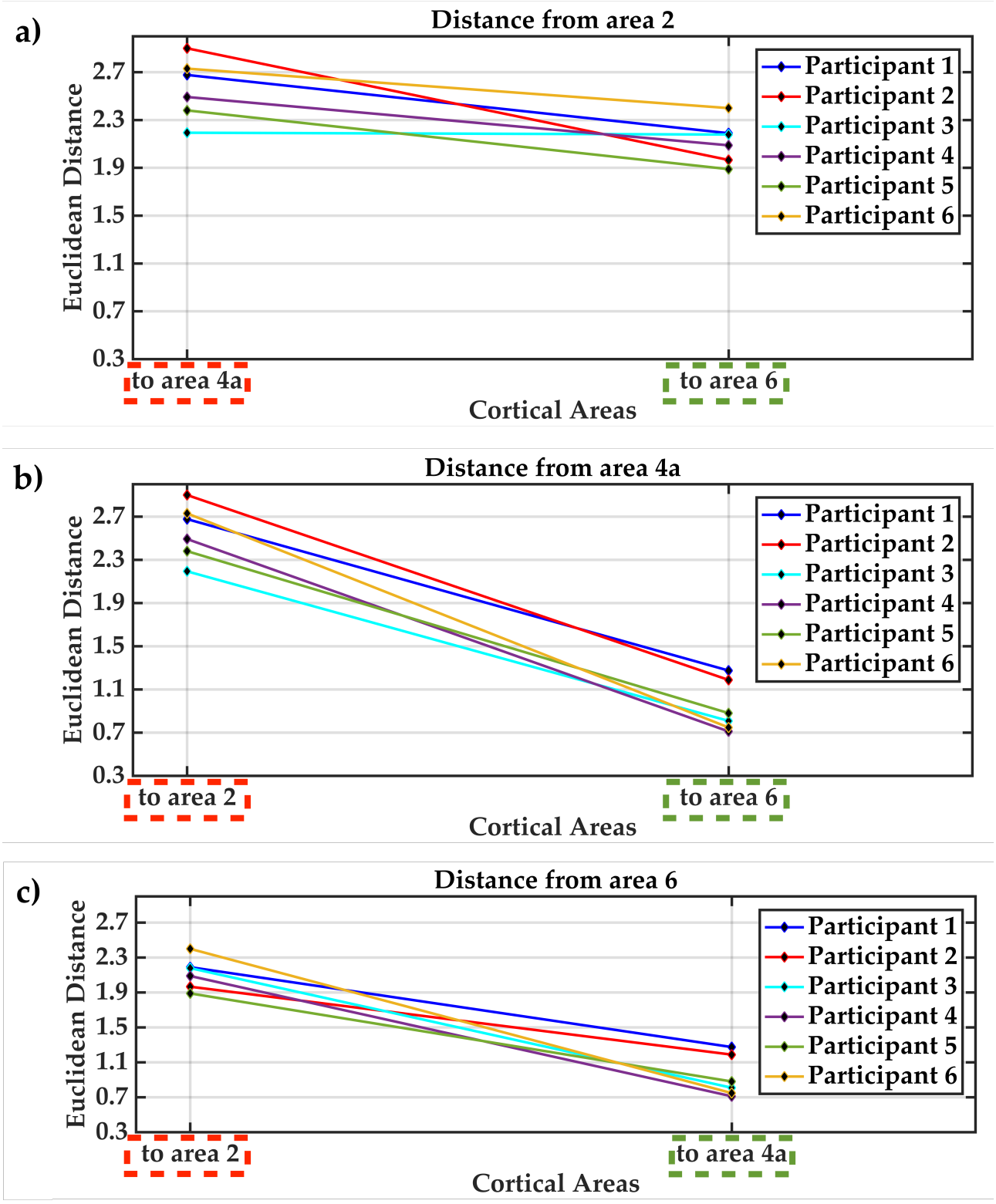

Figure 3-8 The Euclidean distance from a) area 2 to areas 4a and 6, b) area 4a to areas 2 and 6, c) area 6 to areas 2 and 4a for six participants. The maximum (dashed red box) and the minimum (dashed green box) distance values on each diagram identify higher and lower areal dissimilarity to the target area, respectively.

The notched box plots in Figure 3-9 demonstrate the significant difference between the Euclidean distances of pairs of cortical areas of interest. No overlap between the notches of

the three box plots indicates that the medians of the Euclidean distances between the three cortical areas are significantly different (P<0.05). Additionally, the p-values from the Wilcoxon signed rank test [137] on the distance values confirmed that there was a statistical significant difference (P < 0.05) between he Euclidean distance of each area from the other two areas.

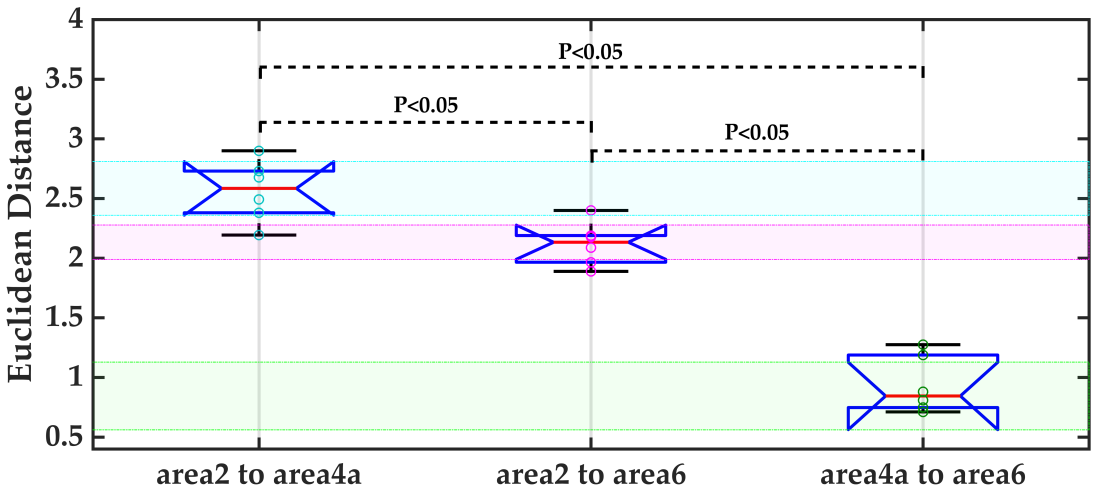

Figure 3-9 Notched box plots of the Euclidean distances between the autocorrelation of the MRF residuals of the three target areas. The distance values between area 2 and 4a are presented with cyan circles, between area 2 and 6 are in magenta, and between area 4a and 6 are in green. The 95% confidence intervals of the distribution of the Euclidean distances between each pair of areas are indicated by the shaded areas with the similar colours. The p-values obtained from the Wilcoxon signed rank test are also displayed for the difference between the medians of the distance values.

3.3.4 MRF Acquisition Time Optimisation

In Figure 3-10 the MSE of the MRF residuals of the selected cortical areas for all participants are illustrated at each subsampling step of the MRF acquisition time optimisation process. The MSE of the residuals at each step were compared with the MSE of the MRF residuals of the original MRF acquisition with 1000 time points (i.e. step '*whole 1000'*). Figure 3-10 is zoomed in for the steps between '*whole 1000*' and '*included every 2nd*' as presented in Figure 3-11, for a closer representation of the difference between the MSE values at these steps. As illustrated in Figure 3-11, the notched box plots of the MSE of the residuals at steps '*dropped every 10th*' to '*dropped every 3rd*' overlap with the notched box plots for the initial step '*whole 1000'.* The overlap implies that no significant difference (P>0.05) was observed between the MSE of the MRF residuals at steps '*dropped every 10th*' to '*dropped every 3rd*', and the MSE of residuals at the initial step '*whole 1000'*. Note that there is no overlap between the notched box plot of step '*included every 2nd*' and the initial step, implying a significant difference (P>0.05) between the MSE of the MRF residuals of these

two steps. This suggested that the subsampling of the residuals could continue up to the step '*dropped every 3rd*', without losing much information in the MRF residuals. As a consequence of the optimisation at this step, the total number of MRF signals time points could reduce to 667 (from 1000), suggesting the feasibility of decreasing the total MRF acquisition time to 26.8 minutes (from 40.2 minutes).

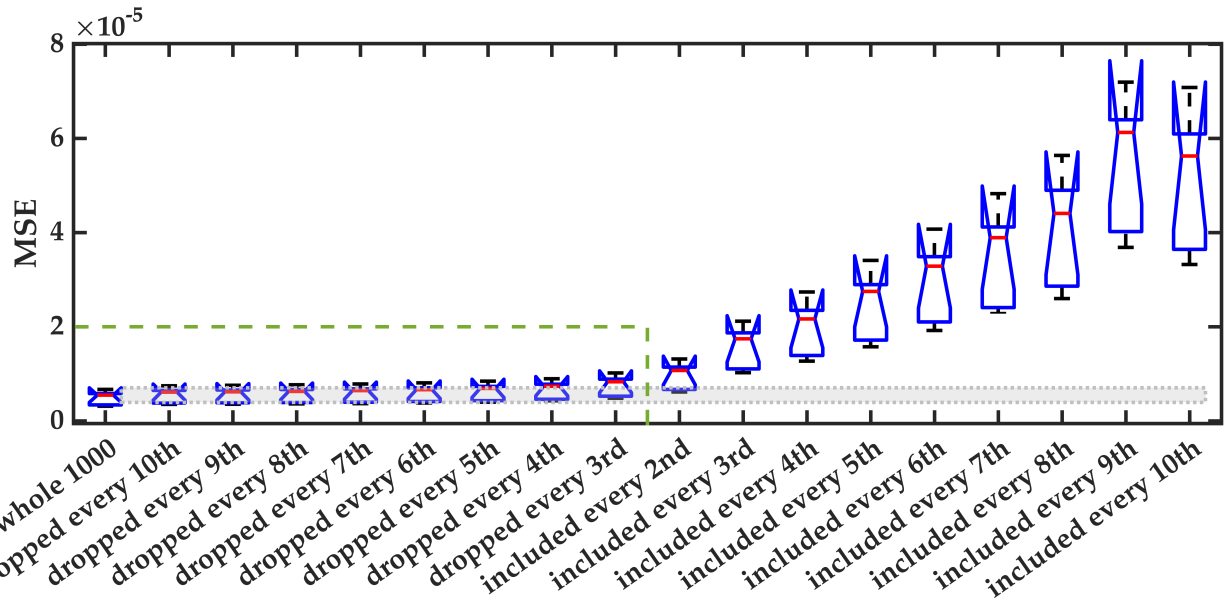

Figure 3-10 MSE of the MRF residuals of the target cortical areas, for all participants, at each subsampling step of the acquisition time optimisation process. The gray shaded area indicates the 95% confidence intervals for the MSE of the MRF residuals at the initial step, where all the 1000 MRF residual signal time points were used.

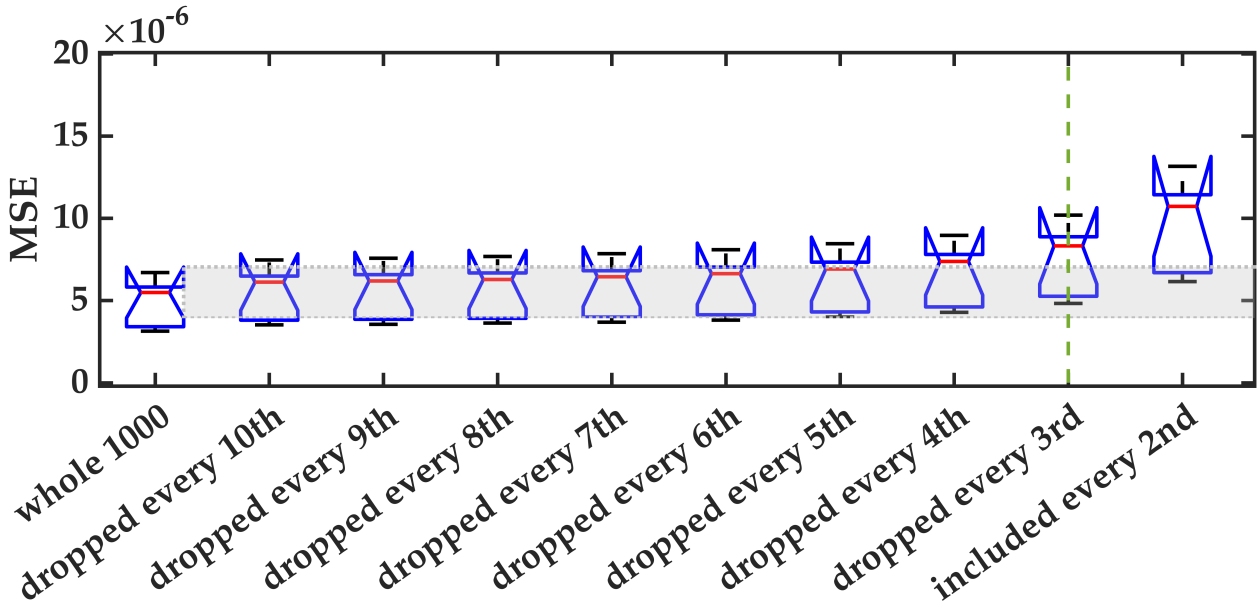

Figure 3-11 The subsampling steps of the MRF acquisition time optimisation process, at which no significant difference (P>0.05) was observed between the MSE of the MRF residuals, as compared with the MSE of the residuals of the original 1000 time point MRF acquisition.

MRF parameter quantification accuracy

Figure 3-12 depicts the simulation of the MRF T1 and $T2^*$ quantification accuracy at different SNR levels (5 – 30), using MRF signals with 1000 and 667 time points. At SNR values of larger than 20, no significant difference (P<0.05) was observed in the relative errors of T1 and $T2^*$ estimations, between the MRF signals with 1000 and 667 samples.

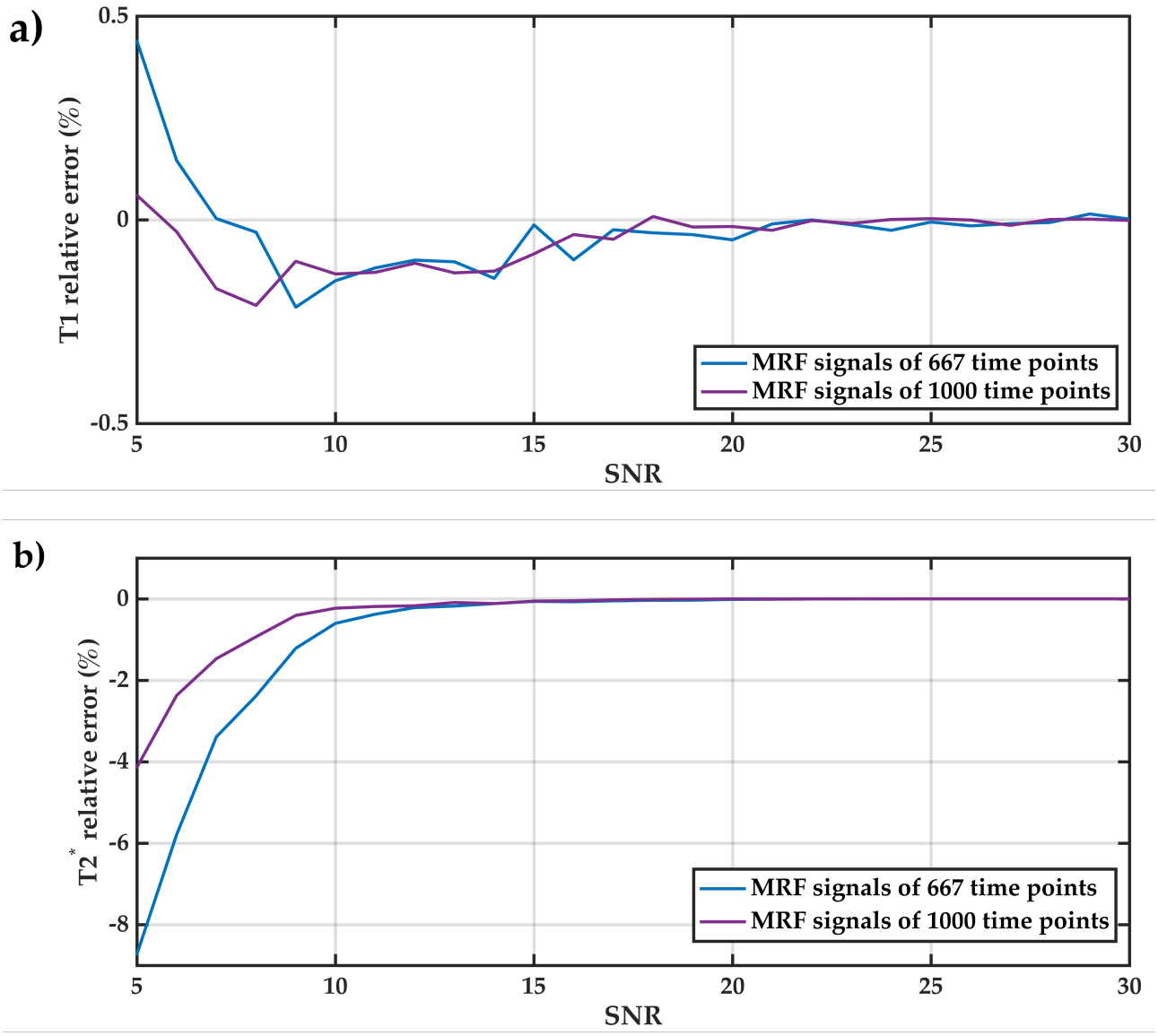

Figure 3-12 The relative error of MRF parameter quantification for a) T1 and b) $T2^*$, at SNR values between 5 and 30, is simulated using 1000-time point MRF signals (blue lines) versus 667-time point MRF signals.

MRF residual analysis of the subsampled signals

In this section, the results of the MRF residual analysis on the subsampled signals for the same cortical areas of interest and the same participants are compared with the MRF residual analysis on the original MRF signals with 1000 samples.

Figure 3-13 illustrates the comparison between the autocorrelation distribution of the subsampled MRF residual signals of areas 2, 4a and 6 for two participants, and the Gaussian white noise autocorrelation distribution. Similar to the white noise test results on the MRF signals with 1000 samples (Figure 3-5), the autocorrelation of the 667-time point MRF residuals of the three areas exceed the 95% confidence interval of the white noise

autocorrelation distribution at several lag numbers. This demonstrates significant non-randomness ($P<0.05$) between the autocorrelation values of each area, suggesting significant difference between the MRF residuals of each area and a white noise process. Similarly, significant difference was observed between autocorrelations of the 667-time point MRF residuals of the three areas and the autocorrelation distribution of Gaussian white noise, for all other participants.

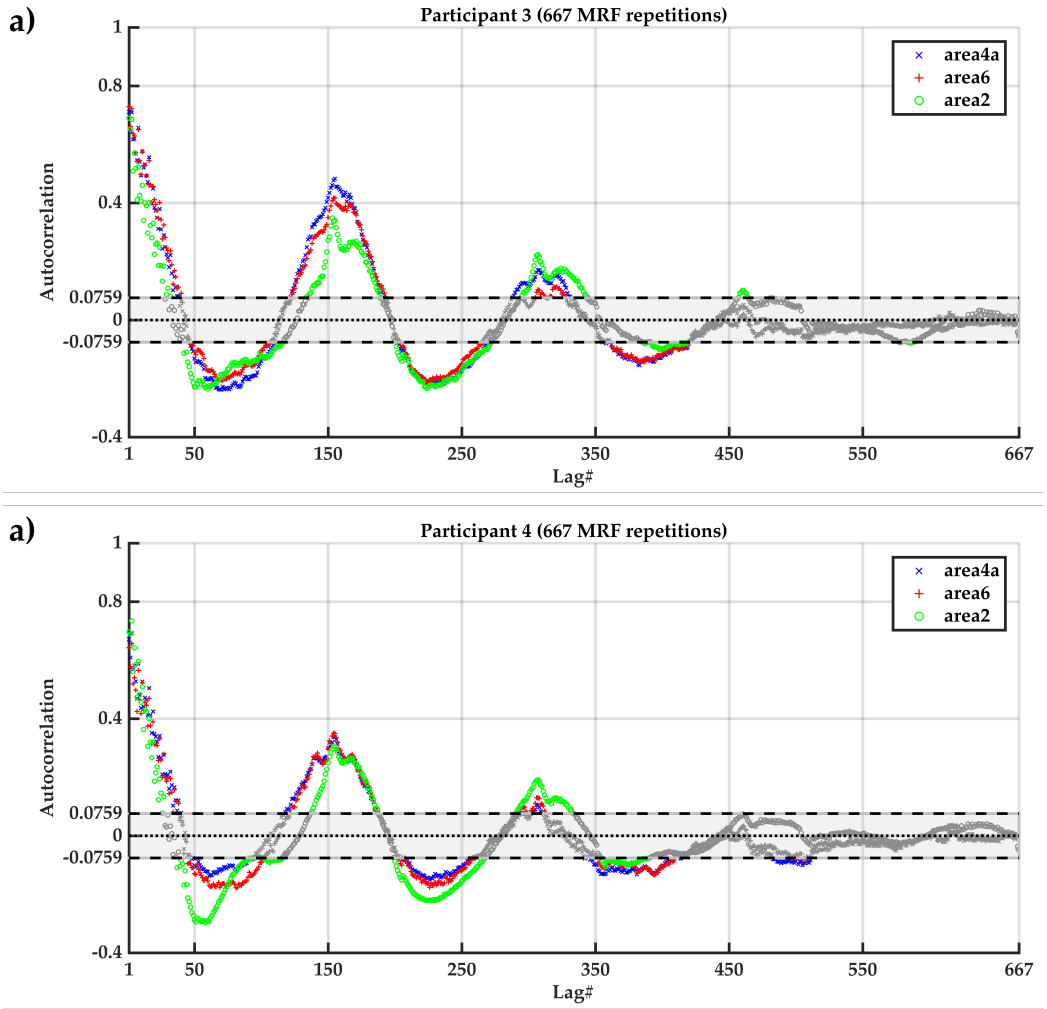

Figure 3-13 Normalised autocorrelation of the 667-time point MRF residuals of area 4a (blue), area 6 (red) and area 2 (green) for two representative participants overlaid on the 95% confidence intervals (±0.075) of a Gaussian white noise autocorrelation distribution. Autocorrelation values that fall between the 95% confidence intervals are greyed out, indicating their insignificance when compared with the white noise autocorrelation distribution.

The mean and standard deviation of the subsampled MRF residual autocorrelations for each area, across six participants, are depicted in Figure 3-14. Comparing the autocorrelation profiles between the three target areas confirmed the presence of area-specific patterns, which are a function of the lag number, as was also observed for the autocorrelations of the 1000-time point MRF residuals (Figure 3-6).

Figure 3-15 illustrates a closer view of the autocorrelation profiles of each area, between lags 42 and 123. The patterns of autocorrelation of each area in this figure is similar to that observed in Figure 3-7 (between lags 62 and 185) for the autocorrelation profile of the areas when we had 1000-time point MRF residuals. Consequently, the characteristic patterns of autocorrelations of the MRF residuals were preserved during the subsampling process.

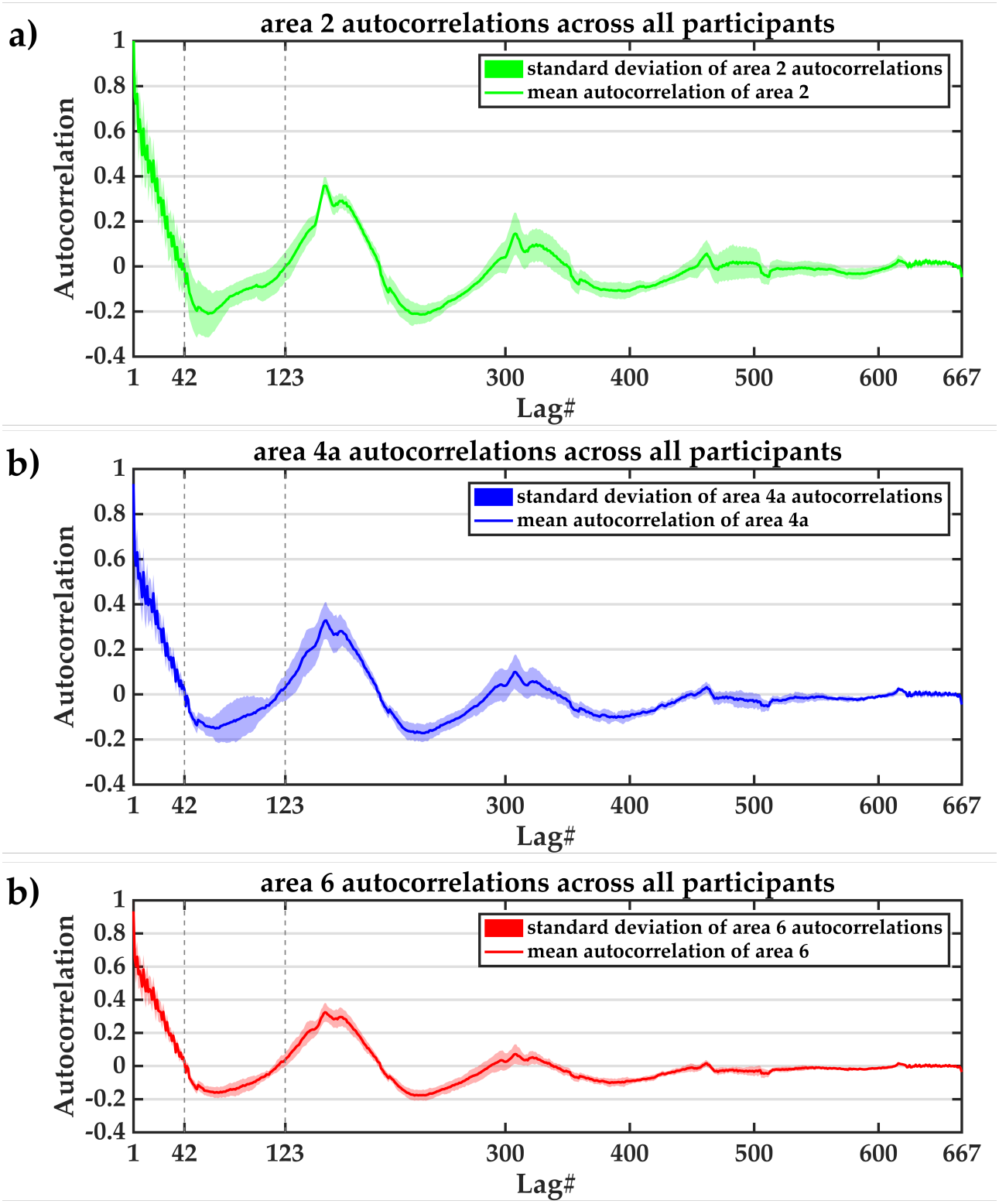

Figure 3-14 Comparison of the normalised autocorrelation patterns of a) area 2, b) area 4a and c) area 6 for six participants, when using the subsampled MRF residual signals with 667 time points. The solid line represents the mean autocorrelation of the MRF residual signal of each area across six participants, and the shaded area corresponds to the standard deviation of the autocorrelations among all participants.

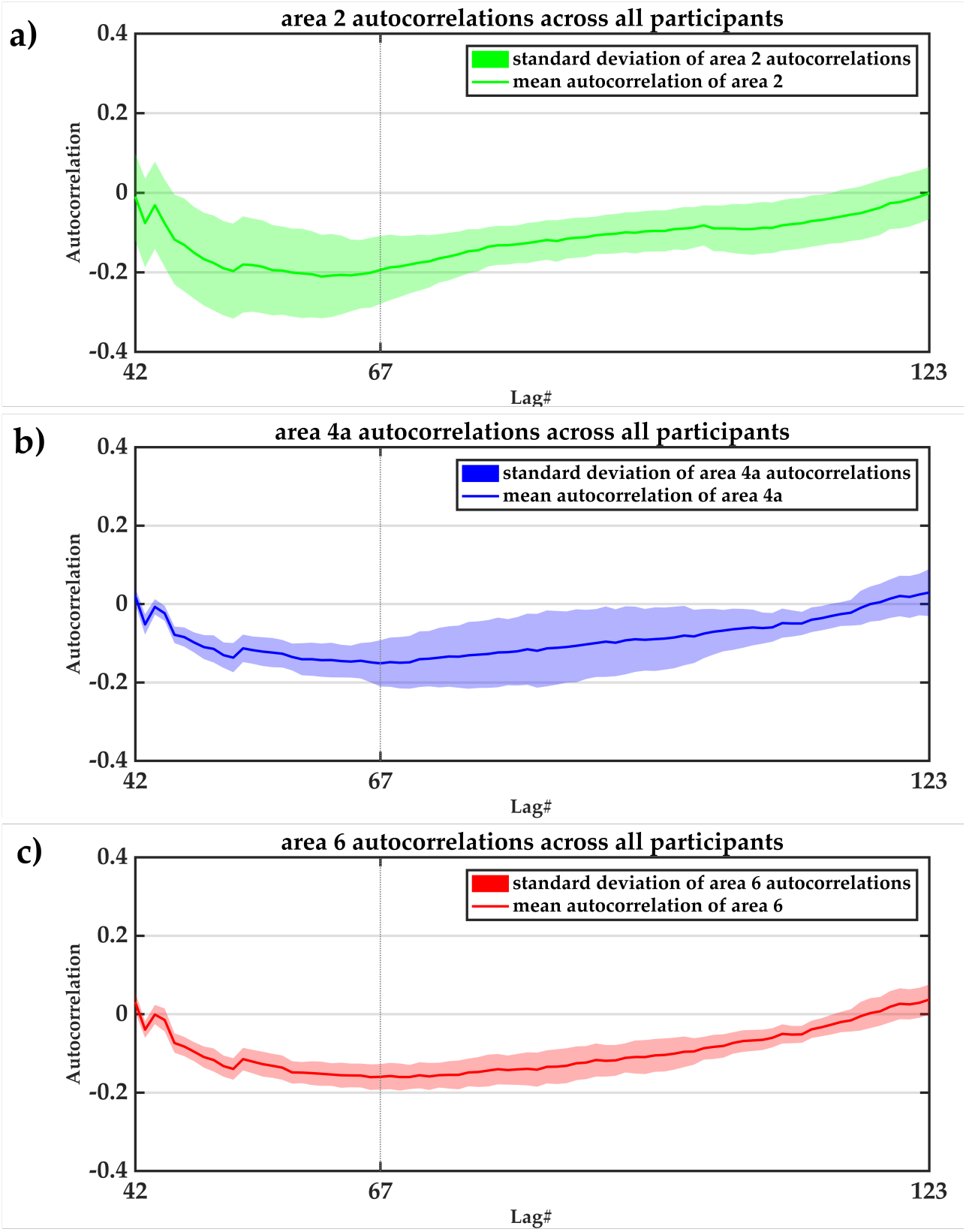

Figure 3-15 An example of the difference in the autocorrelation patterns of a) area 2, b) area 4a and c) area 6 between lags 42 and 123, when using the subsampled MRF residual signals with 667 time points. The solid line represents the mean autocorrelation of each area across six participants, and the shaded area corresponds to the standard deviation of the autocorrelations among all participants.

The areal dissimilarity measures between the subsampled MRF residuals autocorrelations of the cortical areas of interest are displayed in Figure 3-16, for all six participants. Similar to the case when we had 1000-time point MRF residual signals, for all participants, the Euclidean distance from area 2 to area 4a is larger than the distance between area 2 and 6 (Figure 3-16a). This suggests higher dissimilarity between the MRF residuals of area 2 and 4a, than between area 2 and 6 residuals. Also, Figure 3-16 b, c confirm higher similarity between the 667-time point MRF residuals of area 6 and 4a than between area 2 and 4a residuals, as the Euclidean distance between area 4a and 6 is smaller.

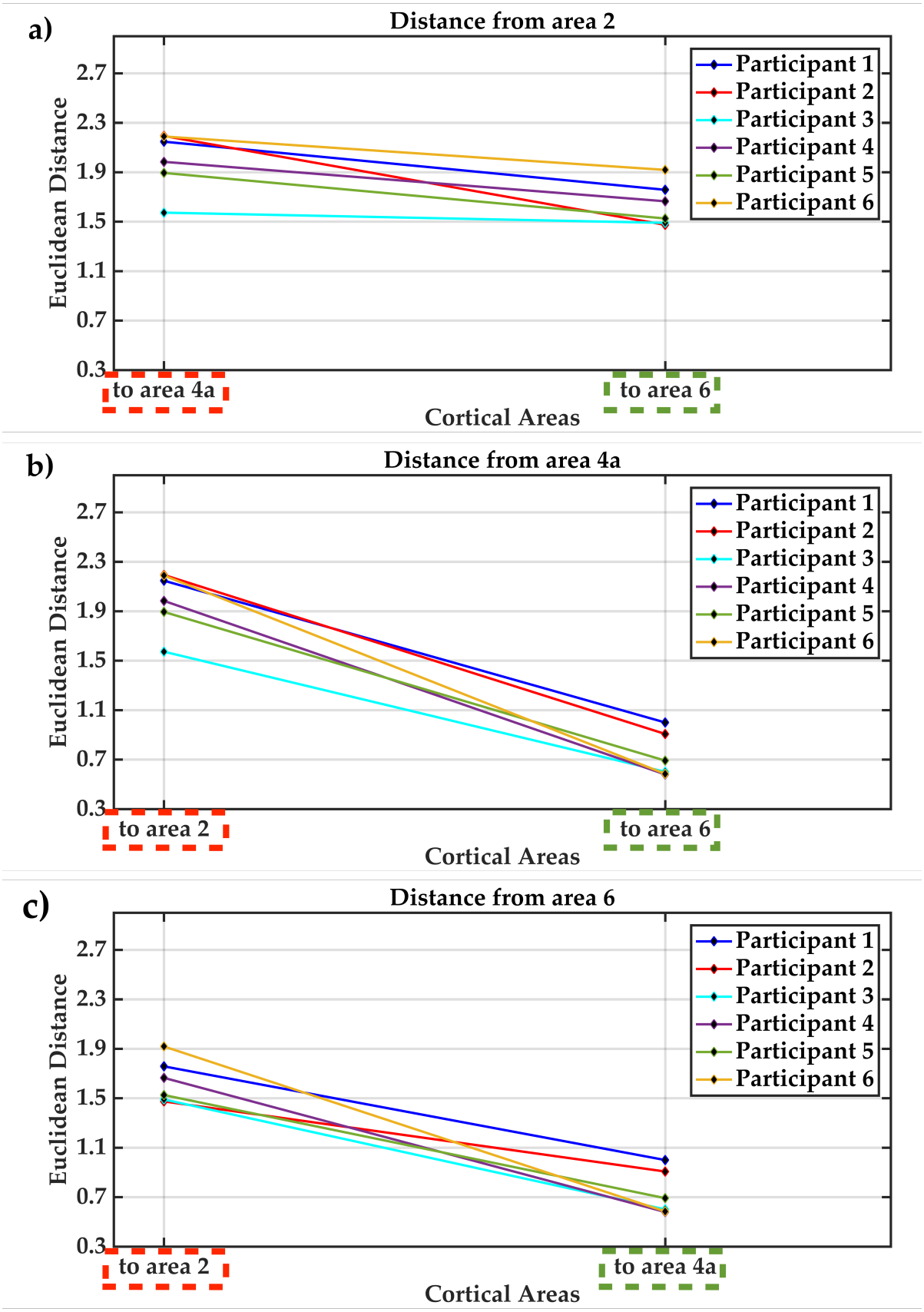

Figure 3-16 The Euclidean distance from a) area 2 to areas 4a and 6, b) area 4a to areas 2 and 6, c) area 6 to areas 2 and 4a for six participants, when using the subsampled MRF residual signals with 667 time points . The maximum (dashed red box) and the minimum (dashed green box) distance values on each diagram identify higher and lower areal dissimilarity to the target area, respectively.

The notched box plots of the Euclidean distances in Figure 3-17 confirmed significant difference (P<0.05) between the distance values of pairs of cortical areas of interest when we used the subsampled 667-time point MRF residuals.

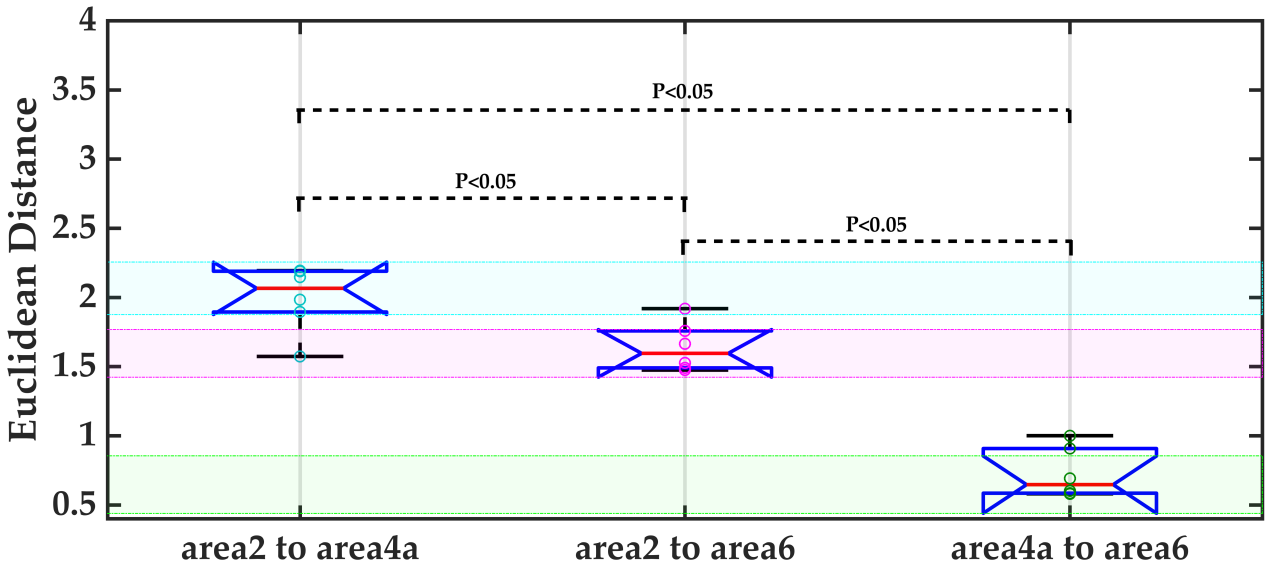

Figure 3-17 Notched box plots of the Euclidean distances between the autocorrelation of the subsampled MRF residuals (with 667 time point samples) of the three target areas. The distance values between area 2 and 4a are presented with cyan circles, between area 2 and 6 are in magenta, and between area 4a and 6 are in green. The 95% confidence intervals of the distribution of the Euclidean distances between each pair of areas are indicated by the shaded areas with the similar colours. The p-values obtained from the Wilcoxon signed rank test are also displayed for the difference between the medians of the distance values.

3.4 DISCUSSION

We demonstrated the feasibility of extending the utility of the MRF residual analysis framework from the 2D single-slice MRF acquisitions (Chapter 2) to 3D volumetric MRF acquisitions. The MRF residual signals generated from the 3D EPI-MRF acquisitions of 1000 baseline images could distinguish the distinctions between three cortical area of interest: primary somatosensory cortex (area 2), primary motor cortex (area 4a), and premotor cortex (area 6).

The Euclidean distance measures between the autocorrelations of the MRF residuals indicated areas 2 and 4a as the most dissimilar, and areas 4a and 6 as the most similar areas. These findings are in agreement with the areal distances observed in Chapter 2 between these three cortical areas. The interareal similarity profiles (Figure 3-8) are also qualitatively in agreement with the areal similarity between these three areas, as examined

in several microstructural mapping studies. For example, areas 2 and area 4a are established to have marked cyto- [62] and myelo-architectonic [121] distinctions, while areas 4a and 6 are known to be marginally different in terms of their microstructural characteristics [62, 121]. Consequently, the areal dissimilarity measures in this study suggest that the distinctive structures present in the MRF residuals might contain information associated with microstructural variations between the cortical areas of interest.

Furthermore, we demonstrated the feasibility of optimising the total MRF scan time from 40.2 to 26.8 minutes. Similar autocorrelation patterns of the 667-time point (Figure 3-15) and 1000-time point (Figure 3-7) MRF residuals for each cortical area, demonstrated that the proposed optimisation scheme would maintain the distinctive structures in the MRF residuals of each cortical area. Further, the agreement between the areal dissimilarity profiles of the 667-time point (Figure 3-16) and 1000-time point (Figure 3-8) residuals, implies that optimised MRF residual signals would preserve sufficient information to distinguish the microstructural variations between cortical areas. Additionally, our simulations suggest that on high-field MR scanners (with high SNR), an MRF acquisition that uses the optimised acquisition parameter patterns with 667 baseline images, would still obtain an MRF parameter quantification accuracy comparable to the MRF acquisition with 1000 baseline images (Figure 3-12). As a consequence of this, the MRF residual signals of the optimised acquisition pattern would contain the same amount of information as in the original acquisition in this study, thus not compromising the separability of the cortical areas based on their MRF residual signals. Moreover, these findings

The 3D EPI-MRF sequence in this study achieved a two-fold acquisition time acceleration, compared with the 2D EPI-MRF sequence used in Chapter 2, mainly caused by the use of GRAPPA parallel imaging with acceleration factor of 2 along the through-plane phase encoding direction. This time acceleration could not be achieved using a 2D EPI-MRF sequence, as there is only one phase encoding direction which only enables in-plane acceleration [144]. In addition to higher acquisition time acceleration, 3D EPI-MRF sequence benefits from higher SNR, improved slice profile and higher through-plane spatial resolutions [144].

The present study formed the basis for future developments towards the whole cerebral cortex parcellation. However, there are several venues for further developments in future works. First, EPI sequences suffer from signal loss at the tissue-air interfaces (e.g. near the sinus), where there is significant magnetic field inhomogeneity [156]. Rieger, et al. [69] have

reported inaccurate $T2^*$ quantification at these areas. Geometric image distortions are also common in EPI acquisitions [156]. These artefacts may challenge the goal of whole cerebral cortex parcellation using the 3D EPI-based MRF residual analysis described in this study. Although many algorithms have been developed to resolve these issues [156], the effect of these artefact correction methods on the MRF signals needs to be investigated in future work. Second, in this study we only showed the feasibility of employing the k-space undersampling techniques along the secondary phase encoding direction that is available in 3D EPI sequences. Accordingly, we only used the acceleration factor of 2 along the through-plane phase encoding direction. Future work may investigate the effect of higher k-space undersampling factors on the MRF signals, and accordingly on the MRF residual analysis framework.

3.5 CONCLUSION

We established the feasibility of distinguishing the microstructural variations between cortical areas, exploiting the previously described MRF residual analysis framework on the data acquired from a 3D EPI-MRF sequence. We also demonstrated the resilience of the MRF residual analysis framework to the optimisation of the total number of MRF repetitions. We established the foundation for future work towards voxel-wise parcellation of the human cerebral cortex, using the area-specific information present in MRF residual signals.

Chapter 4 Towards in vivo voxel-wise parcellation of human cerebral cortex using MR fingerprinting and machine learning

Shahrzad Moinian, Viktor Vegh, David Reutens, “In vivo voxel-wise parcellation of the human cerebral cortex using 3D MR fingerprinting (MRF) and supervised machine learning classification”. Submitted to *International Society for Magnetic Resonance in Medicine (ISMRM)*.

The above conference abstract has been submitted to ISMRM 2020. It has since been revised and further developed, and is incorporated in this thesis as Chapter 4.

I have made a substantive contribution to the authorship of the manuscript:

- Conception and design of the project.
- Analysis and interpretation of the data on which the manuscript is based.
- Drafting significant parts of the manuscript and critically reviewing it so as to contribute to the interpretation.

As the first author, I have participated in conceptualisation, experiment design, MR sequence development and testing, implementation of the data analysis scripts, implementation of the machine learning algorithms and techniques, data acquisition, data analysis and interpretation.

4.1 ABSTRACT

Accurate parcellation of the human cerebral cortex provides a reliable guide for neurosurgical decision making, development of individualised treatment plans and identification of structure-function associations. While the quantitative histology-based methods provide accurate microstructural cortical maps, they are not directly translatable to the individual humans. The most promising *in vivo* quantitative MR-based microstructural cortical mapping methods are yet to achieve a comparable level of parcellation accuracy throughout the cortex.

We present an automated method of *in vivo* voxel-wise human cortical parcellation, using MR fingerprinting (MRF) residual analysis and supervised machine learning classification. We scanned six participants using a 3D EPI-MRF sequence developed in-house on a 7T Siemens scanner. A set of 999 normalised autocorrelations of the MRF residual signal of each voxel of interest from primary somatosensory cortex BA1 and BA2, primary motor cortex BA4a, premotor cortex BA6, visual cortex BA17 and BA18, and Broca area BA45 were used as the feature vectors. The feature vectors of each cortical area were uniquely labelled before being fed into the model selection procedure for comparing the performance of linear support vector machine (L-SVM), Radial Basis Function SVM (RBF-SVM), Random Forests (RF) and K-nearest neighbours (KNN) supervised classification algorithms. We compared the prediction performance of each algorithm, using two different feature representation approaches: i) features from each voxel, and ii) features derived from a volume comprising 3×3×3 voxels.

The RBF-SVM classifier using the volume-based feature representation performed best with macro-average area under the Receiver Operating Characteristic curve (ROC-AUC) of 0.83, sensitivity of 0.71 and specificity of 0.95 on the unseen test set.

The method may have the potential to be integrated with the online image reconstruction process on MR scanners, towards employing voxel-wise microstructural cortical parcellation for real-time clinical applications.

4.2 INTRODUCTION

The importance of accurate individual-specific cortical parcellation of the brain can be well realised in neurosurgical decision-making processes [157, 158], and the study of the association between the function and tissue microstructure [2, 3]. An observer-independent microstructural mapping method was first developed using quantitative histological studies of the post-mortem brain tissues by Schleicher, et al. [9] in 1999. Although this is a reliable and reproducible solution to many problems with the classical histology-based microarchitectonic mapping approaches [15, 16, 25, 30], it cannot be applied to the living human brain.

Among the *in vivo* microarchitectonic mapping methods, the effectiveness of exploiting quantitative multi-modal MRI methods for microstructural mapping of the human brain cortex has been evidenced in a multitude of studies [47, 53, 62, 64, 116, 117]. These methods provided a foundation to obtain insightful information through observer-independent and reproducible examination of the cortical microstructural variations. However, most multi-contrast MR-based microarchitectonic cortical mapping methods developed to date rely on the average microstructural variations across a limited number of individuals. As a result, these methods are mostly inapplicable for delineating individual-specific microarchitectural variations, leading to unreliable and uncertain voxel-wise localisation of some areas in individuals, specifically those with high degree of interindividual microstructural variability (e.g. primary somatosensory cortex [33, 39] and visual cortex [38]).

Inefficiency is another main drawback of the current quantitative multi-model MRI microstructural mapping methods, limiting their utility in real-time applications. The data analysis in these methods involves extensive postprocessing, which usually needs manual intervention [47, 64]. Automating cortical parcellation methods could provide us with major developments in this regard. The improved efficiency gained from an automated voxel-wise cortical mapping method enables utility of the resultant individual-specific maps in real-time applications such as MRI-guided stereotactic neurosurgery [158, 159].

Machine learning (ML) provides the avenue for dealing with both the above-mentioned issues of the current multi-modal MRI microstructural parcellation methods. Firstly, ML-based algorithms have promoted automated model development processes to tackle the problem of time-efficiency in a variety of applications including brain imaging and neuroscience. Supervised ML classification solutions automatically learn a model from a set

of labelled (i.e. with known classes) data samples, describing the distinctions between two or more categories present in the training dataset. Once the model is built, it can be used for time-efficient prediction of the class of future data samples with unknown labels. Secondly, in addition to enhancing time-efficiency, ML-based algorithms have proved effectiveness and reliability in many voxel-wise and individual-specific neuroimaging studies including brain tumour segmentation [160], neurological disease detection [161-163] and identification of psychiatric disorders [164]. Thus, ML facilitates developing models that can learn from voxel-wise individualised data instead of group-average data, and in turn can reliably be applied to new individuals.

A few cortical parcellation studies have also benefited from time-efficient ML-based solutions and their effectiveness in dealing with voxel-wise and individual-specific data. However, ML-based microarchitectural parcellation models developed so far were trained using multiple neurobiological properties like areal function [107, 165], connectivity and topography [107], combined with the microstructural tissue characteristics of the cortex. Combination of these properties has demonstrated enhanced accuracy of areal border delineation, especially where use of only architectonic features has been shown as insufficient (e.g. Broca areas [165]). Despite these developments, as Eickhoff, et al. [8] stressed, each of these neurobiological markers serve us with unique insights into the organisation of brain. Thus, the importance of improving the accuracy of parcellations derived from each one of these neurobiological modalities should not be neglected. Closer inspection of the data used in [107, 165], reveals potential areas of improvement regarding the parcellations obtained from the microstructural properties. They employed a method based on structural T1w and T2w images [121] to derive myelin content and thickness measures of the cortex, while multitude of studies have argued adequacy of MR relaxometry-based information for accurate characterisation of microscopic features throughout the cortex, and have thus suggested adding complementary information from other MR modalities [47, 64].

To the best of our knowledge, no ML-based models have been developed to date aiming at improving microstructural parcellation of the cortex, using microarchitectonic information complementary to the MR relaxometry-based information. The first key challenge for developing such a method could be in identifying an appropriate method of data representation to the ML algorithms. It is essential to provide supervised ML algorithms with descriptive and discriminative characterisation (i.e. features) of the target data samples. In a previous study (Chapter 2), we presented a new quantitative multi-modal MRI method of characterising the human brain cortex, using MR fingerprinting (MRF) residual analysis. The

MRF residual analysis method suggested that MRF signals contain information complementary to the MR relaxometry-based information, which could be helpful towards more accurate microarchitectonic cortical parcellation. Using autocorrelations as a statistical measure of characterising the MRF residuals, we differentiated three microarchitectonically distinct cortical areas (primary somatosensory cortex BA2, premotor cortex BA6 and primary motor cortex BA4a) in six individuals. The results suggest that MRF residual autocorrelations may potentially provide us with an appropriate feature representation, which would be required for developing a ML-based model for microstructural cortical parcellation. However, the analysis in Chapter 2 was based on the average MRF residual signals from each target area, and the utility of the method at the voxel-level was not investigated.

This research aims to establish the feasibility of developing an automated method for *in vivo* voxel-wise parcellation of the human brain cortex. We combined our previously proposed MRF residual analysis approach, as a method of statistical characterisation of the tissue microstructure underlying each image voxel, with classical supervised classification algorithms.

4.3 METHODS

4.3.1 Subjects

Six volunteers (one male and five females) participated in a two hour-long MRI scan session. Participants were healthy individuals aged between 27 years and 35 years with no history of neurological disease. Each participant underwent two scans separated by a 15 minute break. A whole-brain 3D EPI-based MRF scan was performed in both sessions. In the first session, we also performed a whole-brain 3D SA2RAGE and an MP2RAGE scan.

4.3.2 Regions-of-Interest

We extracted 7 cortical areas from the Juelich cyto and myeloarchitectonic histological atlas of the human brain [41, 122]: primary somatosensory cortex (BA1 and BA2), primary motor cortex (BA4a), premotor cortex (BA6), primary and secondary visual cortex V1 (BA17) and V2 (BA18), and the Broca area BA45. These cortical areas were chosen on the basis that they are microstructurally distinct histologically [13, 33, 35, 37-39].

Note that the atlas provides probability masks for each area, representing the interindividual differences in the spatial location of each area. A voxel with high probability value indicates that there is a higher chance that the corresponding voxel in the MR image of a new individual would belong to the area of interest. In this study, we excluded the voxels with probability values of less than 80 percent from the atlas probability masks. All ROI masks were then binarized using FSL [123], such that the value of 1 in the binarized mask represents the voxels with probability of higher than 80 percent.

4.3.3 MRI Acquisition

The scans were performed at the Centre for Advanced Imaging, The University of Queensland, on a 7T whole-body MRI research scanner (Siemens Healthcare, Erlangen, Germany) using a 32-channel head coil (Nova Medical, Wilmington, Massachusetts). B_0 shimming was performed at the beginning of each scan session to reduce susceptibility effects.

MRF acquisition

A 3D EPI-based [144] MRF sequence was used to acquire 1000 frames of 3D MRF images with the following parameters:

TR = 41 - 99 ms (Figure 3-2), FA = 10 - 77° (Figure 3-1), TE = 12 - 48 ms (Figure 3-2), Partial Fourier Phase = 6/8, voxel size = 1.4 × 1.4 × 1.4 mm, and matrix size = 142 × 142 × 88. We used GRAPPA parallel imaging [127] in both phase encoding (with acceleration factor =3 and reference lines = 36) and slice encoding directions (with acceleration factor =2 and reference lines = 12). Fat Saturation was used to reduce the common chemical-shift artefacts observed in EPI sequences [152]. Each MRF scan was acquired twice, in two separate sessions, to increase SNR through averaging.

MRF acquisition patterns

The sinusoidal flip angle pattern used for the MRF acquisitions (Figure 4-1) was adopted from [79], adding the abrupt flip angle changes (0°-40°-50°-60°-0°) at the final frames to increase the sensitivity of MRF signals to $B1^+$ variations [153].

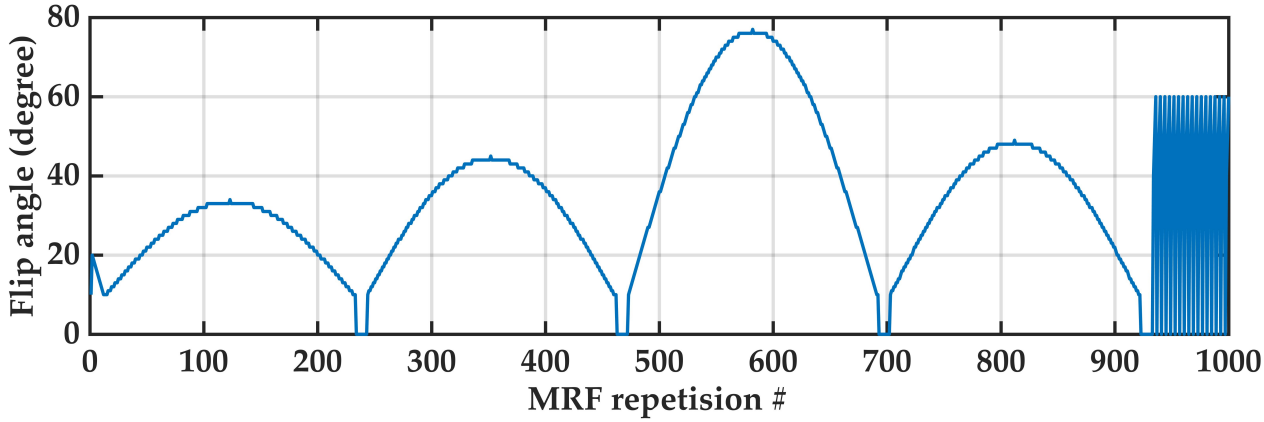

Figure 4-1 The pseudo-randomised pattern of flip angles, used to acquire the 3D MRF images.

We also used pseudo-randomised patterns suggested by Rieger, et al. [69] for TE variations (Figure 4-2), to improve SNR as a result of the higher distribution of TE values at the shorter values. This also allowed optimising the total MRF acquisition time by setting the TR values to the minimum possible value for each TE at each MRF repetition. The alternating pattern has also been shown to increase sensitivity of MRF signals to T1 and $T2^*$ variations [69], leading to more accurate estimation of these tissue properties.

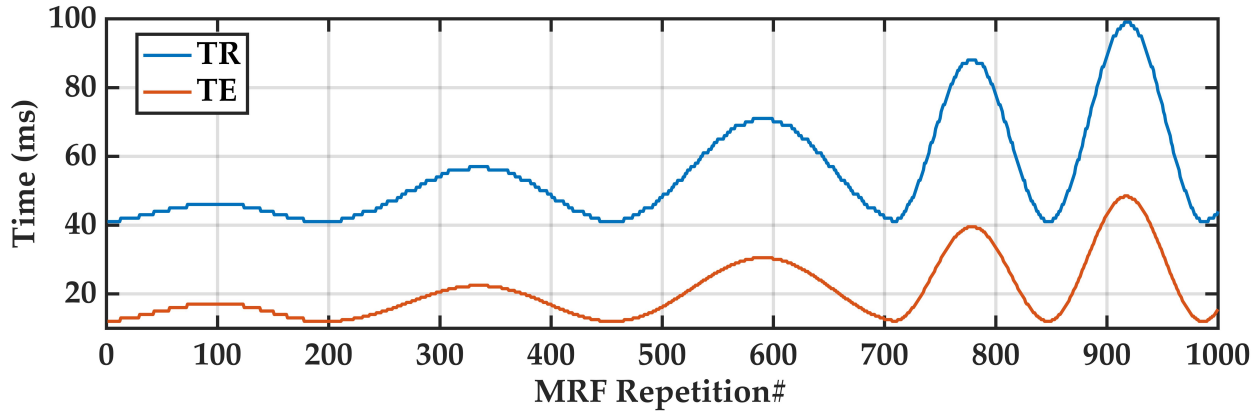

Figure 4-2 The pseudo-randomised pattern of repetition time (TR) and echo time (TE), used to acquire the 3D MRF images

B1+ maps

A 3D Saturation-prepared with 2 Rapid Gradient Echoes (SA2RAGE) sequence [124] was utilised to acquire the whole-brain transmit magnetic field ($B1^+$) map of the brain, for $B1^+$ inhomogeneity correction on the MRF signals [154]. When simulating the MRF signal evolutions for generating the MRF dictionary, $B1^+$ values were used as a linear scaling factor to calculate actual flip angles based on the nominal flip angle values (Figure 4-1).

The SA2RAGE acquisition parameters were as follows: TR = 2400 ms, TE = 0.95 ms, $FA_{1/2}$ = 6°/10°, voxel size = 4 × 4 × 4 mm, and matrix size = 48 × 58 × 64.

T1-weighted images

We acquired 3D T1-weighted images of each participant, using a prototype Magnetization Prepared 2 Rapid Acquisition Gradient Echoes (MP2RAGE) sequence [125]. The acquired T1-weighted images were used to create gray matter masks of each individual and to transform the Juelich atlas masks from the MNI-152 standard space to the MRF native space. The MP2RAGE acquisition was run with the following parameters: Repetition time (TR) = 6000 ms, echo time (TE) = 3.97 ms, inversion time $TI_{1/2}$ = 800 ms/2700 ms, flip angle $FA_{1/2}$ = 4°/5°, voxel size = 1 × 1 × 1 mm, and matrix size = 222 × 240 × 144.

4.3.4 Image Processing

Skull-stripping was first performed on all MRF, T1-weighted and $B1^+$ images, using FSL BET [129], to obtain higher brain tissue co-registration accuracy between these images.

To mitigate the effects of head motion during the long MRF scans, we linearly co-registered (using FSL FLIRT [130, 131] with 6 degrees of freedom (DOF)) all the 1000 MRF 3D volumes in each MRF scan session, separately. Subsequently, we linearly registered (using FSL FLIRT with 6 DOF) the MRF images of the second scan session to the MRF images of the first scan session. Finally, we calculated the average images between the MRF images of the two sessions.

The ROI binary masks were transformed from the MNI-152 standard space to the MRF native space using a two-level process. First, ROI binary masks were non-linearly registered (FSL FNIRT [132]) to the MP2RAGE T1-weighted image for each individual. Subsequently, ROI masks were linearly transformed from the MP2RAGE native space to the MRF native space.

We then used MP2RAGE T1-weighted images to create the individual's gray matter masks, using *fsl_anat* tool [155]. The *fsl_anat* pipeline includes enhanced bias-field correction, which improves tissue type segmentation accuracy. The gray matter mask of each individual was then used to extract the individual-specific portion of the transformed binary ROI masks.

4.3.5 Classification Model

We investigated the utility of classical supervised machine learning classification algorithms to perform voxel-wise cortical parcellation on the 7 cortical areas of interest. Overall, the choice of classical machine learning classification algorithms (and not deep learning) was based on the consideration of the sample size. The general rule of thumb is that deep learning algorithms require a very large sample size, as they would need to extract features from the input data. In contrast, in classical machine learning classification we need to extract some features from the input data (i.e. to characterise the input data), and then provide the classification algorithms with a training set containing the characterised input data.

Multi-class supervised classification

Supervised classification involves learning a model based on a set of labelled training data samples (i.e. with known classes), such that the model can predict the class label of any unseen data samples (i.e. test set) which are described with similar features.

In this study we approached parcellation of 7 cortical areas as a multi-class supervised classification [166] problem. In individual MRF images, voxels belonging to the same cortical area according to the Juelich atlas masks was denoted by a unique integer value.

One-vs-one (OVO) multi-class classification

We employed OVO multi-class classification approach, in which one classifier is trained for each pair of classes [167]. The class that receives the majority of votes at the time of prediction will be then considered as the final class of the input data sample. In contrast to OVO, the one-vs-the-rest (OVR) approach trains one classifier per class [167]. As a result, the computational efficiency of the OVO approach is lower than that of the OVR approach. However, the OVR approach would lead to the class imbalance problem (as discussed in section *Imbalanced class oversampling*), in most of the cases. To avoid the class imbalance problem in this study, use of the OVO approach was preferred.

Feature representation

To develop classical machine learning classification models, data samples need to be described to the algorithm using proper set of features. Identifying a suitable feature representation is the key for developing effective classical supervised classification models. A good descriptive feature, or combination of features, should distinguish the major

distinctions between different classes, while representing the instances of the same class with the highest similarity [168]. The previous study on the use of MRF residuals for characterising tissue microstructure in the human brain cortex suggested normalised autocorrelations of the residuals as an appropriate statistical characterisation measure for identifying microstructural variations in three cortical areas: areas 2, 4a and 6 (Chapter 2 and Chapter 3). Accordingly, in this work we took the normalised autocorrelation values (ranging from -1 to +1) of the MRF residual signals to form a feature vector per voxel of interest.

We opted for two different approaches to form the feature vectors of each voxel.

Single voxel approach

In the single voxel approach, we took the normalised autocorrelation of the MRF residuals from the voxel of interest, creating a 999-point (i.e. autocorrelations for all lags other than 0) feature vector per voxel.

Volume-based approach

Partial volume effect has been shown to affect MRF signals [10]. As a consequence of this, using MRF residual signals of the single voxels for parcellation of some cortical areas might be ineffective. We proposed a volume-based approach to a) account for the possible partial volume effect on the MRF residual analysis in this work, and b) to provide the classification algorithms with more descriptive representation of each voxel. We created the feature vector for each voxel by calculating the autocorrelations of the average MRF residuals of a 3×3×3 voxel neighbourhood, centred at the target voxel. This feature representation method characterises each voxel by its neighbourhood features in addition to its own features. It should be noted that for each 3×3×3 patch, only the voxels that belong to the individual's gray matter tissue were included in the residual averaging.

Classical supervised classification algorithms

We employed the following well-established classical supervised classification methods: Linear Support Vector Machine (L-SVM), Radial Basis Function kernel SVM (RBF-SVM) and Random Forest (RF), K-Nearest Neighbours (KNN). We used *scikit-learn* (v0.21.3) [169], which provides an open-source machine learning library for Python (v3.5), to implement these classifiers. We performed model selection, as detailed later, to tune the set of model parameters that control each of these classification algorithms.

Support Vector Machine (SVM)

Generally, in a high-dimensional feature space, SVM aims to find a separating hyperplane (i.e. decision boundary) to split the data samples into distinct classes, such that the distance from the hyperplane to the data samples is maximal [170]. We selected SVM-based classifiers for this study because they have been shown to be effective when dealing with high-dimensional feature spaces.

The tuning of key parameters of the SVM model is explained below.

Regularisation parameter (C)

The regularisation parameter defines the amount of penalty that should be applied to a misclassificatied data sample, when the SVM algorithm is searching for the optimal decision boundary. More regularisation (i.e. smaller values of *C*) will create smoother decision boundaries, leading to more tolerance to the noise or outliers in the data samples.

Kernel function

The similarity of data samples in the feature space is measured based on a distance function called the SVM *kernel*. In this work, we opted to use linear (Linear-SVM) and a non-linear (RBF-SVM) kernel to perform SVM classification of the data. Linear-SVM looks for a linear decision boundary between the data samples in the feature space, while kernel-based SVM models transform the data samples into a new feature space, in which a linear decision boundary may be found. The linear decision boundary in the new feature space corresponds to a non-linear decision boundary in the original feature space. The kernel function of the RBF-SVM algorithm is defined as follows:

$$K(x_1, x_2) = e^{-\gamma . \|x_1 - x_2\|^2} \quad (2)$$

, where x_1, x_2 and $\|x_1 - x_2\|^2$ represent the feature vectors of two data samples and the distance between the two samples in the original feature space, respectively.

The choice of the RBF kernel function was due to i) the better prediction performance, and ii) more time-efficient training, as widely reported in the literature for high-dimensional data classification, when compared to other types of SVM kernels (e.g. polynomial) [171].

Gamma parameter (γ)

The gamma parameter is specific to the kernel-based SVM models and specifies the similarity radius of the kernel function. As seen in equation (2), the similarity between two

data samples in the transformed feature space (*K*) is a function of their distance in the original feature space. The smaller the γ parameter, the slower the value of the exponential distance function decays. In other words, a smaller value of the gamma leads to a larger similarity radius around the sample data points. Consequently, smaller values of γ consider the samples at greater distances as similar as each other, thus creating smoother decision boundaries.

Random Forest (RF)

A Random Forest algorithm creates an ensemble of decision tree predictors, each of which is built on a random number of training data samples and uses a random subset of features at each splitting node [172]. The majority voting method is used to predict the class of the unseen data samples, preventing the overfitting that commonly occurs with single decision tree models [173]. Additionally, RF models are robust against noise and can handle multi-class classification problems efficiently [173] and are thus theoretically an appropriate choice for the current study.

The key RF algorithm parameters that we tuned through a model selection process are as follows. Note that we used bootstrapping, so that each tree in the model will only be trained on a random number of data samples.

n-estimators

This parameter identifies the total number of decision trees in the RF model. A very large value of this parameter may lead to overfitting, while a small value may cause underfitting.

max-depth

This parameter controls the maximum depth, up to which, each individual decision tree is allowed to continue growing (i.e. splitting further). If not specified, or if set too high, it may lead to full-grown trees where all the leaf nodes are pure. In such a case, all the data samples in the leaf nodes would belong to a single class, causing overfitting to the training data.

max-features

This parameter specifies the maximum number of features that could randomly be selected at each node of the tree to find the best split (i.e. the split that will create more pure child nodes).

criterion

This is an impurity measure that is used to decide the features that create the best split. We evaluated the use of *entropy* and *Gini* index, which are calculated as follows:

$$Entropy = -\sum_{j} p_j \log_2 p_j \quad \textbf{(3)}$$

$$Gini = 1 - \sum_{j} p_j^2 \quad \textbf{(4)}$$

, where p_j is the probability of class *j* in the child node.

K-Nearest Neighbours (KNN)

The KNN algorithm classifies each data sample according to the class of its *K* nearest samples in the feature space [174]. This is a simple and effective classification algorithm, which usually performs well in a wide range of applications dealing with low-dimensional data sets [174]. However, it has also shown a competitive prediction performance for high-dimensional data, when combined with Neighbourhood Component Analysis (NCA) as a distance metric learning algorithm [175]. Additionally, KNN has demonstrated good prediction performance in data sets with the presence of irregular decision boundaries [174].

Our model selection process for this algorithm involved tuning the following parameters:

n-neighbours (K)

This denotes the number of nearest neighbours to consider. *K* influences the smoothness of the decision boundaries (i.e. model complexity). Small *K* values usually create less smooth decision boundaries, leading to higher chance of model overfitting.

weights

This defines a weighting function to weight the distance between a data sample and its *K* nearest neighbours. We evaluated *uniform* weighting in which all *K* neighbours are equally weighted *distance* weighting, in which the weights of neighbours is inversely proportional to their distance from the data sample.

Data preparation

Our data preparation pipeline is illustrated in Figure 4-3.

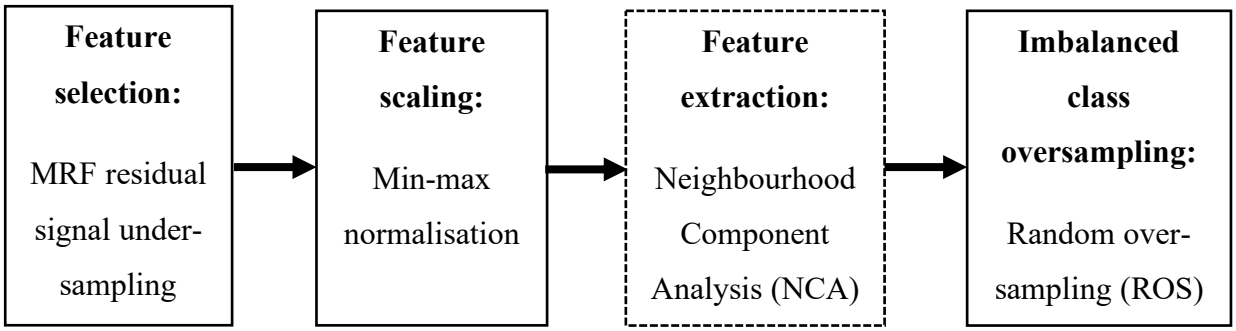

Figure 4-3 The data preparation pipeline performed in this study. Note that the feature extraction step was not applied to all classification algorithms.

Feature preprocessing

Feature scaling

To give the values at all autocorrelation lags equal importance in terms of descriptive information provided to the classification models, we performed min-max feature normalisation on autocorrelation profiles using:

$$X_i' = \frac{(X_i - X_{min})}{(X_{max} - X_{min})} \quad (5)$$

where X_i' and X_i are the new and original values of the feature X of the data sample i, respectively and X_{max} and X_{min} denote the maximum and minimum values of feature X across all data samples. Equation (5) scales the values of each feature (i.e. the autocorrelation values at each lag number) to values ranging from 0 to 1 in all data samples. The scaling prevents the distance measures from being biased towards feature values of higher magnitude but maintains the relationship between the original data [173].

To avoid information leakage to the model being trained [176], we only considered the training samples for calculating the X_{max} and X_{min} values, and then applied these values for scaling the validation and test data samples. It is critical to note that if the scaling is performed on the whole data samples, practically some information about the validation samples, which the model is not supposed to see, would leak to the model training process. The resultant model will then perform well on the validation data samples, demonstrating large evaluation scores which would be misleading for model selection.

Dimensionality reduction

Using the autocorrelations of the MRF residual signals as the feature vectors results in a feature space of 999 dimensions. High-dimensional feature space may not always benefit classification algorithms [177] because training and prediction time increase and sometimes prediction accuracy drops [177]. Feature reduction is usually performed to find the most effective subset of features for the classification problem at hand. Performing feature reduction would be especially important in case of dealing with a small sample size while having high-dimensional feature vectors in the training set (i.e. when the number of features is large relative to the number of samples available in the training set). In such a case, it is particularly important to avoid providing classification algorithms with the features that do not contribute much to the data sample discrimination in the training set. This may be achieved by feature reduction.

To avoid the potential drawbacks of high-dimensional feature space, we performed dimensionality reduction using:

Feature selection

Feature selection is the process of eliminating the features that contribute little towards the separability of different classes [168]. We employed the MRF residual signal subsampling scheme proposed in Chapter 3, as a feature selection method. The advantage of using this approach might be two-fold here: reducing the overall MRI data acquisition time, and improving the efficiency of model training and prediction.

Feature extraction

In contrast to feature selection, feature extraction methods use all the information provided in the original feature space to transform the data into a new lower-dimensional feature space. In most feature extraction methods, each feature in the new space would be the combination of the most discriminative features from the original [168].

For the KNN algorithm examined in this work, it was essential to perform feature extraction in addition to the feature selection mentioned above. One of the main challenges in developing effective KNN models is defining the best distance metric, especially for a high-dimensional feature space. As suggested by Goldberger, et al. [178], we exploited neighbourhood component analysis (NCA), aiming for increasing the efficiency and predictive performance of our KNN classifier. Basically, NCA is a supervised Mahalanobis distance metric learning algorithm that aims to maximise the prediction performance of KNN

through transforming the data samples into a new feature space, where there would be a higher certainty that the instances of the same class demonstrate higher similarity [178]. The main advantage of NCA, which motivated us to select this method over other feature extraction methods, is that it preserves all the information during the dimensionality reduction process [179]. We then used Euclidean distance to measure the similarity of data samples in the transformed space.

Additionally, NCA has also been shown to improve the efficiency and performance of other classification algorithms like Random Forests and SVM [179]. Accordingly, we also used NCA as a feature extraction method to train our Random Forests classifier. However, as SVM models have demonstrated the power of dealing with high-dimensional data effectively, we did not apply NCA to SVM classifiers in our study.

Imbalanced class oversampling

The selected cortical areas in this study are different in size, which means the binary masks of different areas contain different number of voxels. Consequently, the total number of instances (data samples) of each class is different in the training dataset. This leads to the class imbalance problem, which could affect the classifiers' performance if not treated appropriately. One method of dealing with the imbalanced datasets is to perform class oversampling, increasing the number of the minority class instances [180]. We performed random over-sampling (ROS) on all classes except for the majority class (i.e. area BA17). ROS randomly replicates data samples of the minority class. While being computationally cheaper than more complex oversampling methods, ROS has shown competitively high effectiveness in many applications [180].

Model selection and evaluation

For each classification algorithm, we performed grid search to evaluate the predictive ability of the models built using different combinations of the specified model parameter values [181]. The set of parameter values that resulted in the model with the best prediction performance (i.e. with the highest evaluation score) on the unseen testing data samples was selected as the best parameter set, and the resultant model as the best classifier. Grid search model selection has demonstrated efficient applications in medium-sized parameter spaces [181], as is the case in this study.

Evaluation metric

We used the area under the Receiver Operating Characteristic (ROC) curve (ROC-AUC) [182] to evaluate the classifiers' prediction performance. The advantage of using AUC-ROC is two-fold: identifying the best probability threshold for each classifier, and selecting the best model when comparing different classifiers.

Classification algorithms often return the probability of each data sample being from the positive class in a 2-class classification problem. A probability threshold will then define the class of the data sample. The proper discrimination threshold for a classifier could vary in applications. The ROC curve could help us identifying the best threshold by plotting the True Positive Rate (TPR), against the False Positive Rate (FPR) of predictions at different prediction probability thresholds. As a result, ROC curve provides a means of cost-benefit analysis, representing how much sensitivity (i.e. TPR) could be gained at each threshold at the cost of some level of decline in specificity (i.e. 1 - FPR) [182].

Additionally, for model selection on our imbalanced dataset, as suggested by Tang, et al. [183] we needed a single metric, using which we could consider a combination of sensitivity and specificity measures when comparing the effectiveness of different models. AUC of ROC is a reliable performance measure for imbalanced datasets [184], and indicates the probability of all the data samples being classified correctly. AUC of 1 represents a model that could always distinguish all the data samples correctly, while AUC of 0.5 could be observed when a classifier randomly guesses the class of the samples (i.e. there would be an equal chance of classifying a sample into either of the classes).

It should be noted that we used macro-average of the evaluation metrics in this study, to give equal importance to accurate classification of all classes. Macro-averaging takes the average of the evaluation score across all classes, as opposed to micro-averaging that averages the evaluation measure over all voxels.

K-fold cross validation

We performed 5-fold cross validation [185] on each set of model parameter values in the grid search procedure to avoid overfitting the classifiers to the limited data samples. This method randomly subsampled the whole dataset into five mutually exclusive folds and repeated the grid search five times for each set of model parameters. At each repetition, four partitions of the data samples were used as the actual training set and one partition was held out as the validation set. The validation set was then used for evaluating the model

performance on unseen data, to ensure that the model was reliably generalised. The average of the evaluation metric over the five repetitions of the grid search was then taken as the overall performance score of the classifier for the model parameters of interest. It is to be noted that to follow the paired experimental design approach for comparing the performance of different models, we ensured use of the same randomly subsampled data partitions for all classifiers.

Additionally, as we had a multi-class problem, we used a stratified method for dividing the data samples into 5 folds, keeping the portion of data samples of each class in each fold the same as in the initial dataset.

Out-of-sample validation

We used a leave-one-subject-out model validation approach. We held out the data from one participant as the *test* set for the final model evaluation, and only used the data samples from the other five participants for the 5-fold cross validation explained above (i.e. *training* and *validation* sets). A separate test set is essential to improve model generalisation power. It minimises the risk of information leakage [176] to the model training process.

4.4 RESULTS

4.4.1 Feature and Model Selection

Single-voxel feature representation

The results of feature selection and model selection for the single voxel approach are represented in Figure 4-4. The steps of the horizontal axis represent the feature subset that was included in the model selection process. RBF-SVM (C=1000 and γ=0.001) was found to perform best, with macro-average a ROC-AUC of 0.79 for class predictions for the test set.

RBF-SVM also outperformed the other three algorithms when different subsets of feature vectors were selected. When including every third feature value in the feature vector (i.e. sampling the MRF residual at every 3rd timepoint) the macro-average ROC-AUC for RBF-SVM was 0.77 (with C=100 and γ=0.01). However, in return for a 2% drop in ROC-AUC, we could gain a 63% reduction both in the model fitting time and prediction time. Additionally, this would allow us to reduce the total MRF data acquisition from about 42 minutes to about 13 minutes.

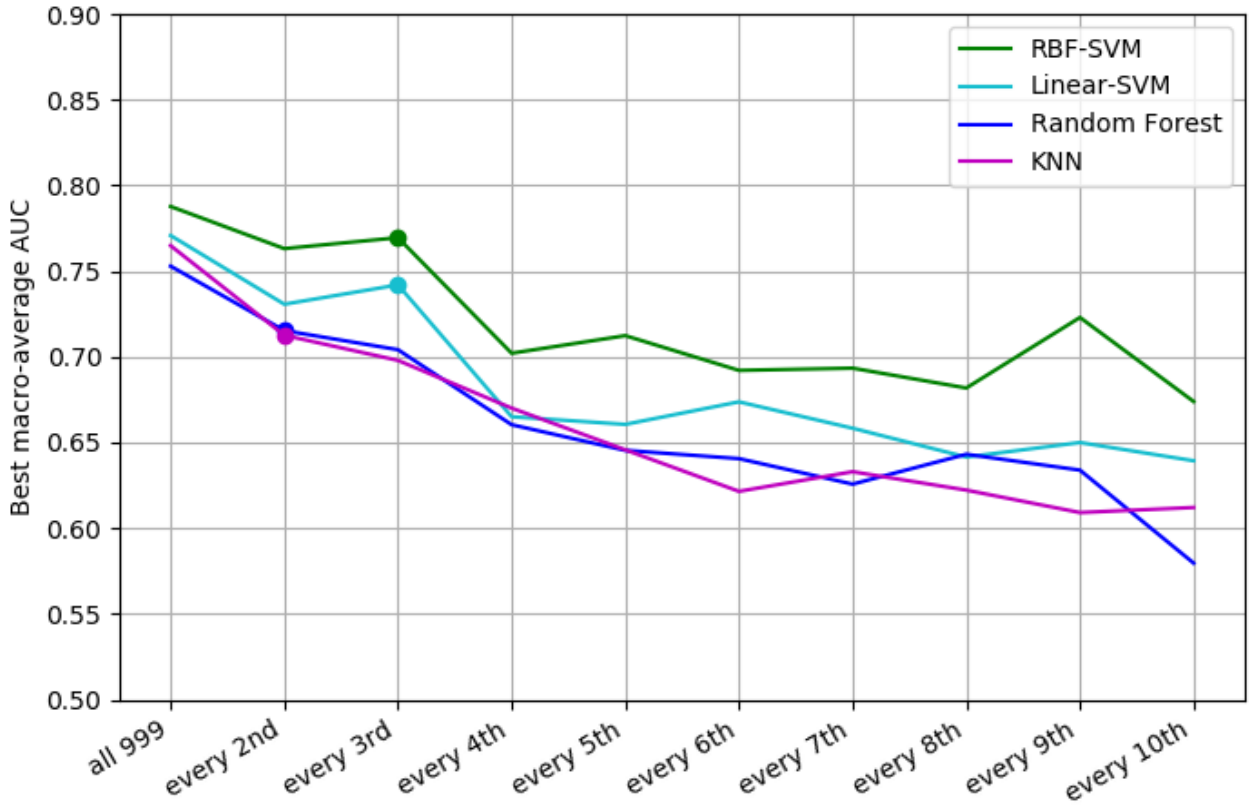

Figure 4-4 The best macro-average ROC-AUC scores of four supervised classification algorithms are compared when trained with different subset of autocorrelation values as the feature vectors. The classification methods used here are Linear-SVM (Linear Support Vector Machine), RBF-SVM (Radial Basis Function kernel SVM), RF (Random Forests) and KNN (K-Nearest Neighbours). The solid circle on each plot represents the subset of autocorrelations at which that model showed its best performance, compared to the initial case of including the whole 999 autocorrelation values.

Volume-based feature representation

The results of model selection process using the volume-based feature representation approach are detailed in Table 4.1. The RBF-SVM model (with C=10000 and γ=0.001) outperformed all other models investigated in this study, with macro-average ROC-AUC=0.83 (sensitivity=0.71, specificity=0.95).

Table 4.1 The ROC-AUC scores of four supervised classification methods are compared, when the volume-based approach was used for feature representation of each voxel.

Classification algorithm	Best macro-average ROC-AUC	Best performer parameters
RBF-SVM	**0.83**	C = 10000, γ = 0.001
L-SVM	0.80	C = 100
KNN	0.75	n-neighbours = 25, weights: distance, distance metric: Euclidean distance on 6 NCA components
Random Forest	0.74	n-estimators = 350, criterion = entropy, max-depth = 20, max-features = 6 NCA components

4.4.2 Volume-based Feature Representation Outperforms

In Figure 4-5, the normalised confusion matrices of the best performer of both feature representation approaches are represented. We found the ROC-AUC of predictions on the held-out test set to improve by using the volume-based feature representation (ROC-AUC increases to 0.83 from 0.79).

The prediction sensitivity scores for the seven cortical areas of interest are represented along the diagonal of the matrices. Comparing these scores between the two matrices shows an overall increase in the sensitivity values by using the volume-based feature representation, for all the seven areas. For three areas (areas BA1, BA45 and BA17) the sensitivity of predictions rose by about 10%. For three other areas (areas BA2, BA4a and BA18) we observed an increase of about 8%, and for area BA6 the sensitivity improved by about 3%.

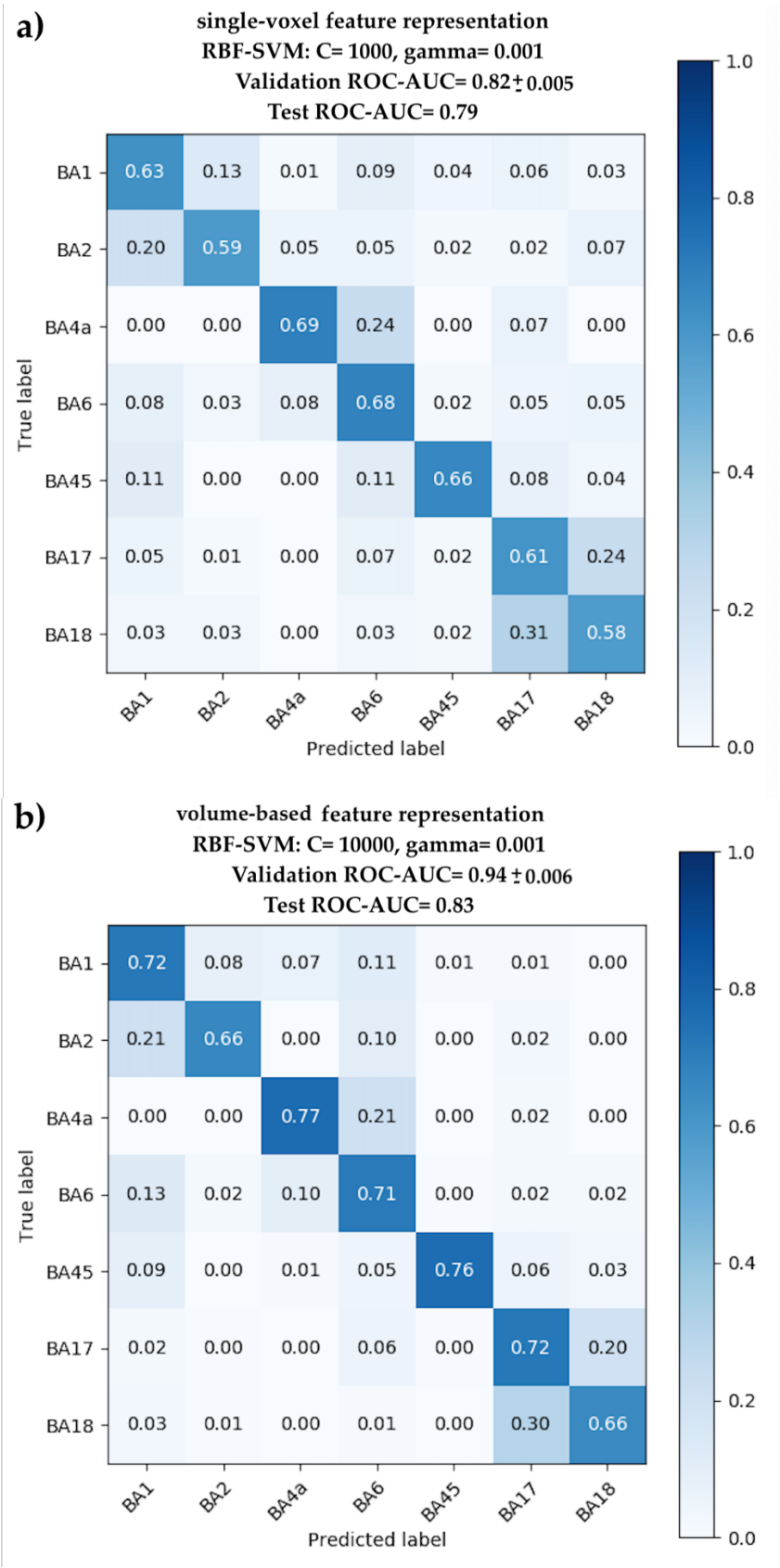

Figure 4-5 Normalised confusion matrices for the best performer (i.e. RBF-SVM classifier) trained with a) the single-voxel feature representation, and b) the volume-based feature representation. The model parameters, the validation and the test ROC-AUC scores of the best classifier are stated at the top. Cell values along the diagonal represent the sensitivity of the model predictions on the held-out test set. The values were rounded up to two decimal places.

4.4.3 Evaluation of the Best Volume-based Classifier

Figure 4-6, Figure 4-7 and Figure 4-8 depict a representative distribution of the true class (top panels) versus the predicted labels (bottom panels) for the unseen data samples of the held-out participant, using the selected RFB-SVM classifier trained with the volume-based feature vectors (the confusion matrix of these predictions is presented in Figure 4-5b). The class labels are overlaid on the MP2RAGE T1-weighted anatomical image of the participant.

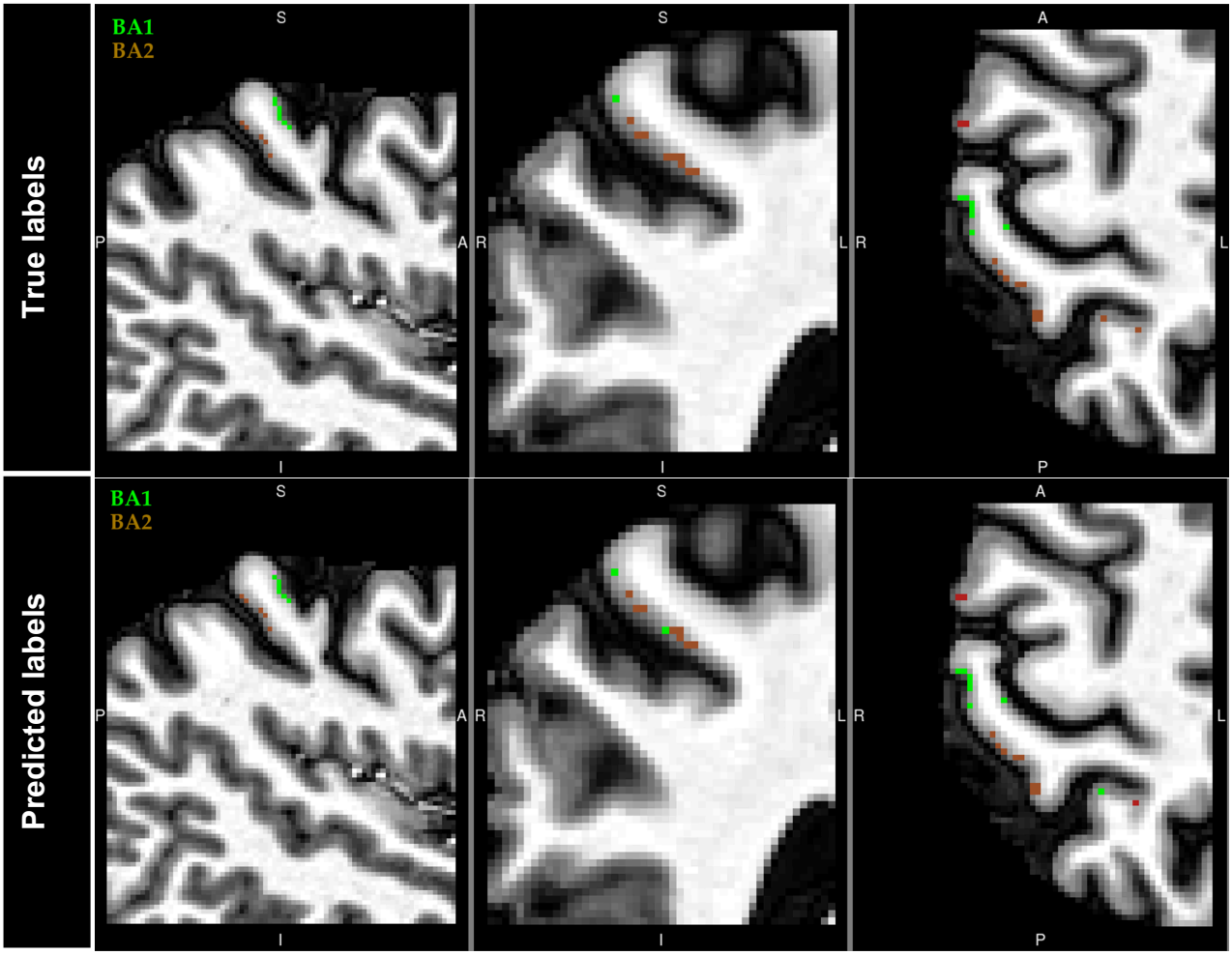

Figure 4-6 True class labels (top) versus the predicted class labels (bottom) for primary somatosensory cortex areas BA1 and BA2 of the held-out participant, using the RBF-SVM classifier trained with the volume-based feature representation.

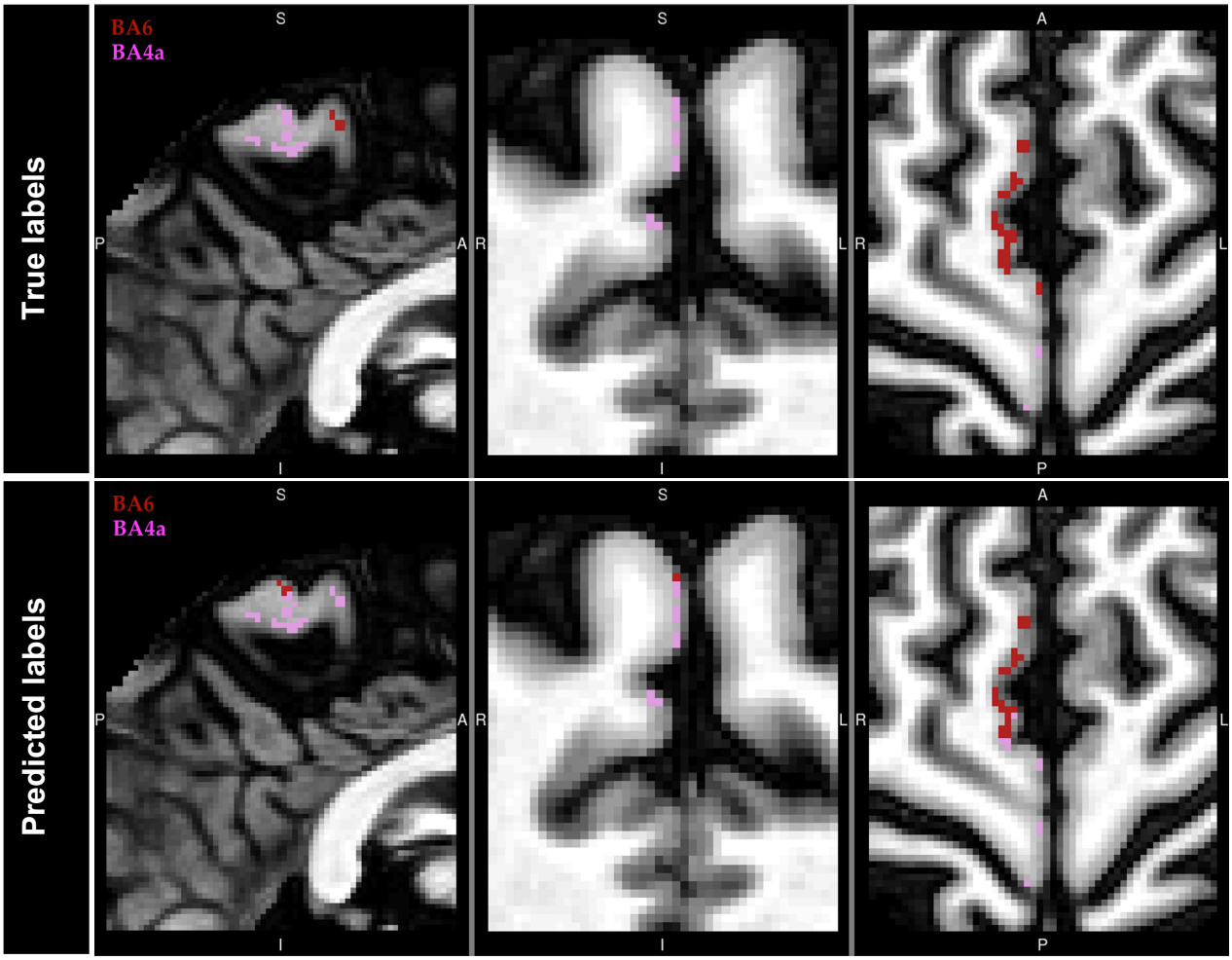

Figure 4-7 True class labels (top) versus the predicted class labels (bottom) for premotor cortex area BA6 and primary motor cortex area BA4a of the held-out participant, using the RBF-SVM classifier trained with the patch-based feature representation.

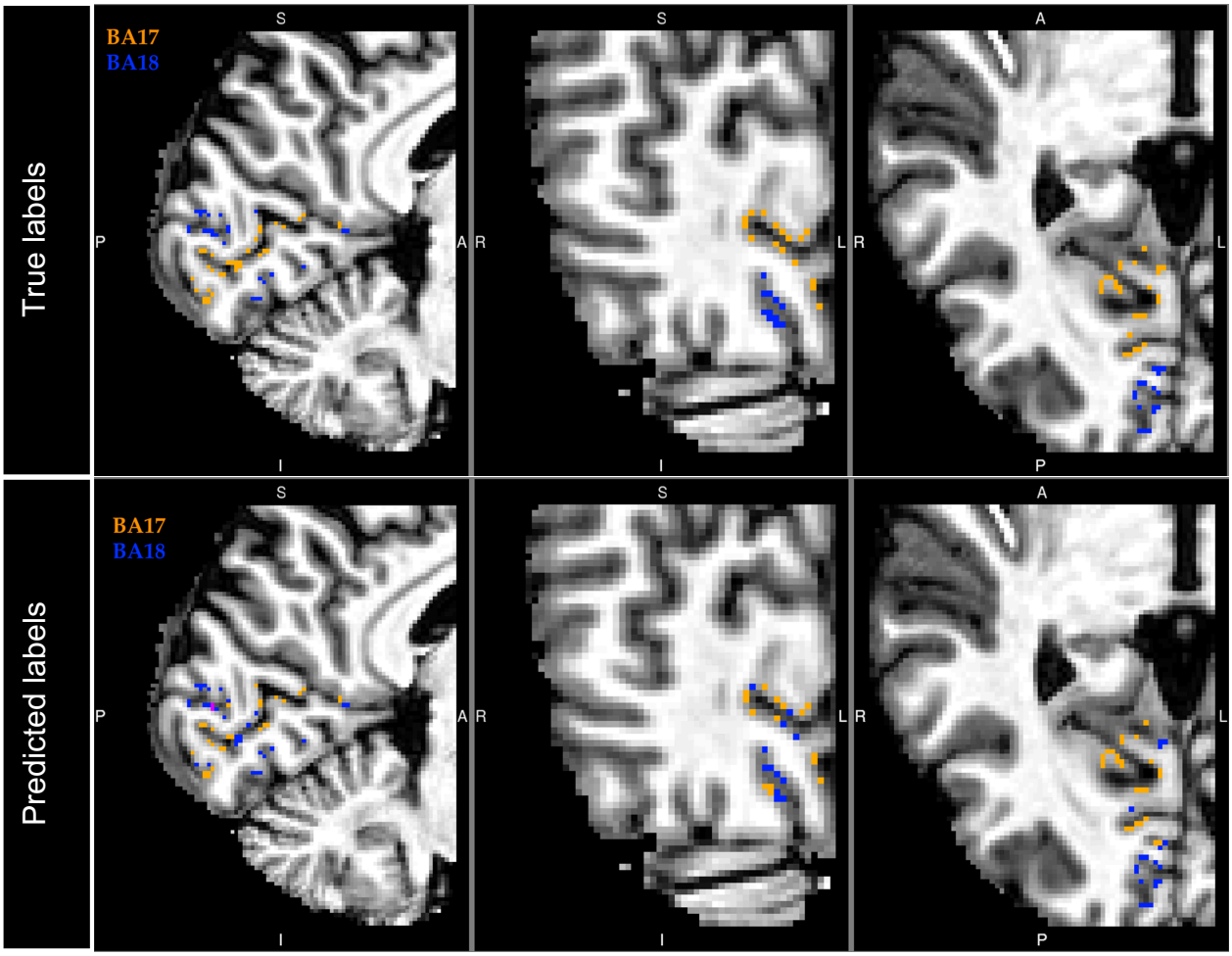

Figure 4-8 True class labels (top) versus the predicted class labels (bottom) for visual cortex areas BA17 and BA18 of the held-out participant, using the RBF-SVM classifier trained with the volume-based feature representation.

4.5 DISCUSSION

Achieving the average prediction score of ROC-AUC=0.83 (by a RBF-SVM classifier using the volume-based feature representation) in voxel-wise parcellation of seven cortical areas demonstrated the feasibility of developing an automated *in vivo* method of voxel-wise cortical parcellation, using a combination of MRF residual signals and supervised machine learning.

The present voxel-wise cortical parcellation method aimed at improving the parcellation performance based on the microstructural tissue properties. In contrast, the previous ML-based cortical parcellation methods mostly utilise multiple neurobiological properties (i.e. functional, connectional and topographical features) [107, 165]. Those studies claim the applicability of their voxel-wise ML-based parcellation methodology to other lesion segmentation applications (e.g. multiple sclerosis). Nevertheless, they note that the

extended applicability would require preparation of proper training dataset [165]. Therefore, identifying and extracting suitable feature representations might be the key challenge towards employing the multi-neurobiological methods in other microstructure-based segmentation applications. Accordingly, an important advantage of the parcellation framework presented here could be seen in its efficient method of data acquisition and subsequent feature extraction. As discussed in Chapter 2, the microstructural characterisation of each voxel in the present study would not require acquisition of separate complementary MR modalities (e.g. phase data of MR signals), as opposed to the conventional multi-modal MRI microarchitectural mapping methods. Moreover, here, the feature extraction process involves computationally cheap calculation of the MRF residuals and autocorrelation of the residuals, and there would be no need for complex data integration from multiple modalities. Consequently, the efficient microstructural feature extraction method of the present study facilitates the application of our ML-based voxel-wise parcellation method in tissue segmentation applications such as classification of brain tumour types.

We found the feature representation approach based on a volume of neighbouring voxels led to higher prediction accuracy in comparison to the single voxel approach (Figure 4-5). The volume-based feature representation in this study could be seen as a combined local-global brain partitioning method. In a sole local parcellation method, each position along the cortex is only compared with its neighbouring positions based on a defined set of features (as was performed in Schleicher's [9] observer-independent method to delineate borders of cortical areas). However, in the present machine learning (ML)-based parcellation method, the local features at each position (i.e. from a volume of neighbouring voxels) will be then compared against the features obtained from all other positions within all ROIs. In other words, similar to local partitioning methods, including features from the volume of voxels surrounding the voxel of interest provided the similarity functions of classification algorithms with descriptive information about the voxel neighbourhood. Also, at the global level, the similarity of each volume was measured against all other volumes regardless of their spatial location in the cortex. Hybrid local-global brain partitioning methods have demonstrated improved parcellation performance, compared with local (e.g. classical histological mapping) or global (e.g. connectivity-based parcellation) partitioning approaches [8, 186]. This may suggest that the higher prediction accuracy of volume-based feature representation stems from its hybrid parcellation approach, and is in line with similar improvements observed in other hybrid methods of cortical mapping [186].

The false negative rates (FNR) along each row (excluding the elements on the diagonal) of the confusion matrix of the best classifier (Figure 4-5b) may imply microstructural similarities between the cortical areas of interest. For example, when comparing the similarity of BA2, BA4a and BA6, out of all the data samples of BA2, 10% were predicted as BA6, and none (0%) as BA4a. Also, among the samples of BA4a, 21% misclassified as BA6, and 0% as BA2. Finally, of all the samples of BA6, 10% were incorrectly classified as BA4a, and 2% as BA2. Comparing the FNR values between these three cortical areas may suggest that BA4a and 6 had the highest similarity, causing the classification model to make the least accurate predictions when distinguishing the voxels of these two areas. Additionally, the classifier did not misclassify any of the voxels of BA2 as BA4a, or of BA4a as BA2, suggesting the highest dissimilarity between these two areas, comparing with their similarity to BA6. These findings were in line with the similarity measurements between these three areas as reported in Chapter 3, although here we examined the voxel-wise similarities. Also, as discussed in Chapter 3, the areal similarity between these three areas in the current study were in agreement with the microstructural similarity and dissimilarity of these cortical areas established using histological studies. Therefore, it may be inferred that our feature vectors (i.e. autocorrelation of MRF residuals) could be a representation of the microarchitectonic characteristics of the areas of interest at the voxel level.

Nonetheless, it should be noted that histological studies of cortical microstructure have mostly employed local partitioning methods [8], making further microstructural inferences about the other areas of interest in this study challenging. Further validation of the microstructural similarity findings of the present study would require experiments that compare a combination of microarchitectonic characteristics of areas globally, instead of focusing on the local microarchitectural transitions at the boundaries between adjacent areas.

Our voxel-wise parcellation method may potentially be integrated with the image reconstruction procedure on the MR scanner, towards real-time application of the cortical parcellation. To achieve this, an essential step would be to improve the time efficiency of the parcellation approach. The dimensionality reduction results illustrated in Figure 4 demonstrated the feasibility of increasing time efficiency of our parcellation approach. Including every 3rd feature value (out of all 999 autocorrelation values) resulted in 63% decrease in the model fitting and prediction time for the RBF-SVM classifier. Additionally, it would give us the possibility of lowering the total MRF acquisition time to 13 minutes (from 42 minutes with 1000-timepoint acquisition). The value of this increased time efficiency could

be well realised in real-time applications of cortical parcellation, especially when we aim at whole-cortex parcellation which leads to having more voxels at the time of class prediction. However, the mentioned time optimisation came at the price of 2% drop in the prediction score (ROC-AUC) of the classifier. In the context of voxel-wise cortical parcellation, even a small accuracy sacrifice could lead to critical clinical consequences. Thus, in future applications of the present method, a trade-off between the desired time efficiency and prediction accuracy should be sought. Furthermore, for real-time applications of the method, further investigation would be required in terms of compensating for the prediction accuracy loss, when the proposed dimensionality reduction will be used.

4.5.1 Limitations and Future directions

In supervised machine learning classification, errors in the class labels of the training dataset could affect the resultant model. In this study we set the probability threshold at 80% to extract the areas of interest from the probabilistic Juelich histological atlas masks of cortical areas. Although this was a relatively high probability threshold, it did not provide us with 100% accurate class labels in the training set. In consequence, the classification model presented in this study might have been influenced by inaccurately labelled data samples in the training set. To mitigate this problem in future work, through acquiring data from a greater number of individuals, we would be able to set the probability threshold even higher to increase the probability of preparing more accurately labelled training data samples. Furthermore, one may investigate a method to complement the atlas-based class labelling of the training set with state-of-the-art quantitative *in vivo* multi-model MRI cortical mapping methods. This approach would decrease the efficiency of the present method at the model development phase, due to the additional data acquisition and data preprocessing steps for labelling the training set. However, after the model is trained, we would still be able to benefit from the efficiency of the method at the prediction time.

There are many avenues for improving the accuracy of the present parcellation method in future work. In this study, we only used autocorrelation to statistically characterise the MRF residuals for creating the feature vectors. Adding other statistical measures of time series has shown prediction accuracy enhancement in some machine learning studies [187]. Moreover, deep learning (DL) methods have proved effectiveness in learning features from the time series data [188]. In addition to enhanced efficiency, employing a DL-based classification in our method potentially leads to improved accuracy, as more discriminative features may be extracted from the MRF residual signals.

4.6 CONCLUSIONS

The results achieved in this study show the feasibility of developing a machine learning classification approach based on MRF residual signals, towards automatic in-vivo parcellation of the human brain cortex. Also, we showed that a patch feature extraction style improved the accuracy of predictions. In future work, we expect to improve the accuracy of predictions by a) using more statistical measures to characterise the MRF residual signals and b) collecting a larger training set.

Chapter 5 Conclusions and Future Directions

The primary focus of this thesis was on the study of how, over and above quantitative MR relaxometry, multi-modal quantitative MRI can inform us about the microstructure of the human cerebral cortex. Quantitative multi-contrast MRI methods are invaluable probes for the microstructural characterisation of the human brain [47, 64]. Further, these methods facilitate integration of the resultant microstructural maps with functional MRI data in the same individual, laying the foundation for dissecting structure-function correlations within the human brain [47]. However, the sensitivity of each of the multi-modal MRI microstructural mapping methods developed to date is still limited to only a few microscopic substrates [47], thus neglecting the contribution of other microscopic components on MR parameter values. Incorporating a larger number of MR contrasts to increase sensitivity to a wider range of microstructural characteristics would give rise to additional problems such as lengthy data acquisition, inefficient data integration, and complex data interpretation. These issues face the current multi-modal MRI mapping methods [64] and have hampered the achievement of a comprehensive whole-cortex *in vivo* microstructural mapping method.

In this study, Magnetic Resonance Fingerprinting (MRF) was used to characterise microstructural variations in the human cerebral cortex. The MRF framework is a reasonable choice as a quantitative multi-modal MRI method for the goal of this thesis, as it i) is initially not designed to show higher sensitivity to particular parameters, ii) has mitigated the data acquisition, integration and interpretation challenges facing other multi-modal MRI methods [64]. Despite these advantages, MRF has not been employed as a tool for microstructural characterisation of the cerebral cortex to date.

5.1 SUMMARY OF ACHIEVEMENTS

In Chapter 2, I proposed a novel quantitative framework that employs MRF and statistically characterises the MRF residual signals, after accounting for the effect of relaxometry-based tissue properties (T1 and T^*) on the MR signals. It was shown that MRF residual signals were specific for each microstructurally distinct cortical region investigated. This finding suggested that i) the information provided by the MR relaxometry parameters were not sufficient to fully characterise the microarchitectonic distinctions between the cortical areas, ii) MRF residual signals may contain additional information about the tissue microstructure.

In Chapter 3, first, I demonstrated the applicability of the MRF residual analysis framework to the MRF data acquired from a 3D volumetric MR imaging acquisition, for a number of cortical areas. This established the feasibility of extending the spatial coverage of the MRF

residual analysis method, towards the ultimate goal of whole-cortex microstructural mapping. Second, I demonstrated the feasibility of optimising data acquisition time by subsampling the residual signal. Both these findings suggest that the proposed MRF residual analysis framework may potentially be adaptable and adjustable to new MRF sequences and acquisition schemes.

In Chapter 4, I established the utility of the information provided by the MRF residual analysis framework in developing an automated voxel-wise cortical parcellation method. I developed a machine learning classifier with the prediction accuracy of above 80%, in seven microstructurally distinct cortical areas. These findings further confirm the potential of the MRF residual analysis framework for microstructural characterisation of the human cerebral cortex at the voxel level.

5.2 DISCUSSIONS AND FUTURE DIRECTIONS

The proposed MRF residual analysis framework potentially provides a foundation for investigating the combined effect of all microscopic components on the MR signal. This could be a major improvement on the existing multi-modal MRI microarchitectonic mapping methods, from two standpoints. First, the models used previously by multi-modal methods to infer microstructural information involve assumptions about the presence or absence of the microscopic components in the tissue [47, 116]. This neglects the potential effect of other components that might be present in the tissue being characterised. In contrast, the proposed method makes no assumptions about the type of microscopic tissue components contributing to the MRF residual signal structure, opening the way to detecting the potential effect of all unknown components. This provides the opportunity to characterise i) new cortical areas or subareas, in the context of cortical parcellation, ii) unknown microstructural alterations of the tissue, in the context of neurological disease diagnosis, for example. Consequently, the additional information present in the MRF residuals, and their statistical characterisation by the MRF residual analysis framework, may potentially lead to the development of new biomarkers for both normal (e.g. microstructural changes through brain development, or ageing) and diseased (e.g. myelin integrity alterations in multiple sclerosis) cortical tissue. Second, the combined effect of multiple microscopic components on the MR contrast might be beyond and more complex than just the sum effect of each single component [64]. The proposed MRF residual analysis method provides a suitable framework for further investigation and characterisation of such complex effects.

One of the main challenges in the previous multi-modal MRI microstructural mapping methods is with regard to integration of multiple MR parameters. The ultimate goal of combining these parameters is to obtain new markers such that more accurate tissue microstructure characterisation can be achieved, as compared to the case when individual MR parameters are used. This could be even more challenging when a larger number of modalities needs to be combined. Integrating machine learning classification with the MRF residual analysis framework in this thesis provides an efficient method to solve the more complex problems in such cases, even when more complex patterns and associations are to be distinguished in the multi-modal data. It should be noted, however, classical machine learning classification algorithms may not be adequate for the more complex case of whole-cortex parcellation. In that case, more discriminative features maybe required to be able to detect subtle dissimilarities between some areas at the global level, as opposed to the more commonly used method of local partitioning methods (i.e. on the basis of variations between neighbouring areas of the cortex) for cortical parcellation [8]. Therefore, future work may employ deep learning methods. Deep learning algorithms, as opposed to classical feature-based machine learning classification algorithms, work with the raw data and have been shown to effectively extract more appropriate (i.e. more discriminative) features for the context of the problem in hand. This potentially leads to the ability to identify more complex patterns in the data and to improve prediction accuracy.

Moreover, the generalisability of the classification model developed in the final experimental chapter of this thesis (i.e. Chapter 4) is demonstrated through evaluation of the trained model on the data from the hold out subject (results illustrated in figures 4.5 – 4.8). These results to some extent represented the generalisability power of the classification model developed in this chapter. However, as the studies presented in this thesis were proof of concept studies, further investigation regarding the generalisability of the proposed method on more heterogenous populations should be pursued in future work. In particular, the generalisability of the method to more heterogenous populations might be challenging in terms of extracting the ROIs. In the present study, the ROIs were extracted based on the assumption that the individual MR images can be accurately registered to the standard brain template in the MNI space. However, obtaining accurate image registration in a brain with pathology might be challenging. The effect of microstructural changes resulting from the pathologies should also be investigated.

The adaptability of the MRF residual analysis framework to the 3D volumetric acquisition scheme and the robustness to the subsampling optimisation scheme suggests that the

proposed framework is not limited to a specific MRF sequence or acquisition parameter scheme. These features could be extended in several future developments based on the present study. Future work may involve integrating the MRF residual analysis framework with previous MRF-based clinical applications (e.g. epilepsy [90, 91] and multiple sclerosis [68] diagnosis, characterising age-related microstructural changes [86]), towards the ultimate goal of developing new MRF residual-based biomarkers of disease. Moreover, the feasibility of adding machine learning-based solutions to clinical applications of the proposed framework may improve efficiency when i) developing a classifier which involves identifying complex patterns across large number of different modalities, and ii) making predictions on unseen data.

Further, cortical parcellation through the identification of variations in the laminar patterns of neighbouring areas across the cerebral cortex has been a common approach since the time of the initial classical histological mapping methods [20, 23]. With the development of the observer-independent method for distinguishing the laminar distinctions, reliable and reproducible cortical border delineation was achieved *ex vivo*. Several high resolution MRI-based methods aiming to identify cortical laminar variations *in vivo*, have been since developed [27, 34, 50]. However, a prerequisite for achieving the goal of accurate delineation of intracortical borders *in vivo* is a robust method of quantification and analysis of the lamination patterns on MRI scans. The MRF residual analysis framework proposed in this thesis would make this possible, as it provides a method for statistically characterising voxel-level microstructural variations, reflected in the MRF residual signals. Accordingly, future work may involve further investigations on the utility of MRF residual analysis method in achieving the ultimate goal of accurate intracortical border localisation *in vivo*. It should be noted that to achieve this goal, further improvements of the MRF signal acquisition might be required to increase the MRF image resolution. The partial volume effect resulting from a larger voxel size may cause the MRF signals investigated in this study to be contaminated by the effect of adjacent WM or CSF tissue. Although I tried to mitigate this effect by excluding voxels with GM probability less than 90%, future work should include the application of methods to account for partial volume effects. The contribution of distant cortex on the MRF signal acquired from a large voxel might remain a challenge. In this thesis, I excluded cortical areas with a very small width (e.g. the somatosensory area 3 that is reportedly the thinnest cortical area), and the areas studied, particularly areas 4 and 6, are among the thickest cortical areas. Future work should further investigate the effect of voxel size on the effectiveness and performance of the present cortical mapping method.

Finally, it should be noted that the need for observer-independent microstructural parcellation was one of the main motivations for performing the studies presented in this thesis. However, the analysis pipeline proposed in this thesis was a novel approach to this research problem. As a result, I formulated the problem as a proof of concept study to demonstrate the feasibility of using the proposed analysis framework for cortical tissue characterisation. Accordingly, in the first experimental chapter (Chapter 2) I selected only three areas, such that I could find several histological studies in the literature with robust and concordant data on the degree of microstructural (dis)similarities between the three areas. This strategy allowed me to validate the inter-areal dissimilarity measures from my study with the microstructural similarity measures in the literature. In Chapter 3, again, I targeted the same three cortical areas, because I intended to show that the 3D EPI-MRF sequence, which was developed in-house, could achieve a similar pattern of inter-areal similarity measures as was obtained using the 2D EPI-MRF sequence in Chapter 2. In Chapter 4, however, I investigated the applicability of the proposed method in a larger number of areas (7 areas). However, to examine how the present ML-based cortical parcellation method performs on an even larger number of areas, or even on the whole cortex, future work should acquire data from a larger number of participants to provide the learning algorithms with a larger training set.

5.3 CONCLUSIONS

The work presented in this thesis provides a systematic method for characterisation of the MR-based microstructural information, complementary to those obtained from MR relaxometric properties. Furthermore, the proposed analysis framework introduces an approach for quantifying the similarity between the MR signals, enabling cortical parcellation at the voxel level in individuals. Moreover, the flexibility of the proposed method in terms of adopting different MR acquisition schemes and its integrability with machine learning-based solutions lays the foundation for several possibilities for future improvements and additional new applications.

References

[1] K. Zilles and K. Amunts, "TIMELINE Centenary of Brodmann's map - conception and fate,", *Nature Reviews Neuroscience,* vol. 11, no. 2, pp. 139-145, Feb 2010, doi: 10.1038/nrn2776.

[2] C. J. Honey, J.-P. Thivierge, and O. Sporns, "Can structure predict function in the human brain?," *Neuroimage,* vol. 52, no. 3, pp. 766-776, 2010.

[3] M. Wahl *et al.*, "Microstructural correlations of white matter tracts in the human brain," *Neuroimage,* vol. 51, no. 2, pp. 531-41, Jun 2010, doi: 10.1016/j.neuroimage.2010.02.072.

[4] S. H. Eriksson, E. J. Rugg-Gunn, M. R. Symms, G. J. Barker, and J. S. Duncan, "Diffusion tensor imaging in patients with epilepsy and malformations of cortical development,", *Brain,* vol. 124, pp. 617-626, Mar 2001, doi: DOI 10.1093/brain/124.3.617.

[5] G. Douaud *et al.*, "Brain microstructure reveals early abnormalities more than two years prior to clinical progression from mild cognitive impairment to Alzheimer's disease," *Journal of Neuroscience,* vol. 33, no. 5, pp. 2147-2155, 2013.

[6] E. Widjaja *et al.*, "Subcortical alterations in tissue microstructure adjacent to focal cortical dysplasia: detection at diffusion-tensor MR imaging by using magnetoencephalographic dipole cluster localization," *Radiology,* vol. 251, no. 1, pp. 206-215, 2009.

[7] K. Schmierer *et al.*, "Diffusion tensor imaging of post mortem multiple sclerosis brain,", *Neuroimage,* vol. 35, no. 2, pp. 467-477, Apr 1 2007, doi: 10.1016/j.neuroimage.2006.12.010.

[8] S. B. Eickhoff, B. T. Yeo, and S. Genon, "Imaging-based parcellations of the human brain," *Nature Reviews Neuroscience,* vol. 19, no. 11, pp. 672-686, 2018.

[9] A. Schleicher, K. Amunts, S. Geyer, P. Morosan, and K. Zilles, "Observer-independent method for microstructural parcellation of cerebral cortex: A quantitative approach to cytoarchitectonics," *Neuroimage,* vol. 9, no. 1, pp. 165-77, Jan 1999, doi: 10.1006/nimg.1998.0385.

[10] D. Ma *et al.*, "Magnetic resonance fingerprinting,", *Nature,* vol. 495, no. 7440, pp. 187-192, Mar 14 2013, doi: 10.1038/nature11971.

[11] R. Nieuwenhuys, "The myeloarchitectonic studies on the human cerebral cortex of the Vogt-Vogt school, and their significance for the interpretation of functional neuroimaging data,", *Brain Struct Funct,* vol. 218, no. 2, pp. 303-352, Mar 2013, doi: 10.1007/s00429-012-0460-z.

[12] K. Amunts and K. Zilles, "Architectonic Mapping of the Human Brain beyond Brodmann,", *Neuron,* vol. 88, no. 6, pp. 1086-1107, Dec 2015, doi: 10.1016/j.neuron.2015.12.001.

[13] S. Geyer, *The microstructural border between the motor and the cognitive domain in the human cerebral cortex*. Springer Science & Business Media, 2012.

[14] K. Brodmann, *Brodmann's: Localisation in the cerebral cortex*. Springer Science & Business Media, 2007.

[15] K. Brodmann, *Vergleichende Lokalisationslehre der Grosshirnrinde in ihren Prinzipien dargestellt auf Grund des Zellenbaues*. Barth, 1909.

[16] C. F. von Economo and G. N. Koskinas, *Die cytoarchitektonik der hirnrinde des erwachsenen menschen*. J. Springer, 1925.

[17] S. Sarkisov, I. Filimonoff, and N. Preobrashenskaya, "Cytoarchitecture of the human cortex cerebri," *Moscow: Medgiz,* 1949.

[18] P. Bailey, "The isocortex of man," *Urbana,* vol. 3, 1951.

[19] K. S. Lashley and G. Clark, "The Cytoarchitecture of the Cerebral Cortex of Ateles - a Critical Examination of Architectonic Studies,", *J Comp Neurol,* vol. 85, no. 2, pp. 223-305, 1946, doi: DOI 10.1002/cne.900850207.

[20] K. Brodmann, "Handbuch der neurologie," *Allgemeine Neurologie. Berlin, Germany: Julius Springer. p,* pp. 206-307, 1910.

[21] A. W. Campbell, *Histological studies on the localisation of cerebral function*. University Press, 1905.

[22] G. E. Smith, "A new topographical survey of the human cerebral cortex, being an account of the distribution of the anatomically distinct cortical areas and their relationship to the cerebral sulci," *Journal of anatomy and physiology,* vol. 41, no. Pt 4, p. 237, 1907.

[23] O. Vogt and C. Vogt, "Zur anatomischen Gliederung des Cortex cerebri," *J Psychol Neurol,* vol. 2, pp. 160-180, 1903.

[24] C. Vogt, *Allgemeinere Ergebnisse unserer Hirnforschung: Von Cécile und Oskar Vogt. 1. bis 4. Mitteilung. Mit 141 Textabbildungen und 5 Tafeln. 1. Mitteilung: Ziele und Wege unserer Hirnforschung. 2. Mitteilung: Das Wesen der topischen architektonischen Differenzen des Cortex cerebri. 3. Mitteilung: Die architektonische Rindenfelderung im Lichte unserer neuesten Forschungen. 4. Mitteilung: Die physiologische Bedeutung der architektonischen Rindenfelderung auf Grund neuer Rindenreizungen*. Joh. Ambr. Barth, 1919.

[25] O. Vogt, "Die myeloarchitektonische Felderung des menschlichen Stirnhirns," *J Psychol Neurol,* vol. 15, no. 4/5, pp. 221-232, 1910.

[26] C. Vogt, "Allgemeinere ergebnisse unserer hirnforschung," *J Psychol Neurol (Leipz),* vol. 25, pp. 279-461, 1919.

[27] S. Eickhoff *et al.*, "High-resolution MRI reflects myeloarchitecture and cytoarchitecture of human cerebral cortex," *Hum Brain Mapp,* vol. 24, no. 3, pp. 206-215, 2005.

[28] T. Kaes, *Die Grosshirnrinde des Menschen in ihren Massen und in ihrem Fasergehalt: ein gehirnanatomischer Atlas, mit erläuterndem Text*. Fischer, 1907.

[29] E. Gerhardt, "Die Cytoarchitektonik des Isocortex parietalis beim Menschen," *J Psychol Neurol,* vol. 49, pp. 367-419, 1940.

[30] A. Hopf, "Über die Verteilung myeloarchitektonischer Merkmale in der Stirnhirnrinde beim Menschen," *J Hirnforsch,* vol. 2, no. 4, pp. 311-333, 1956.

[31] O. Vogt, "Die myeloarchitektonik des isocortex parietalis," *J Psychol Neurol,* vol. 18, pp. 379-390, 1911.

[32] R. Nieuwenhuys, C. A. J. Broere, and L. Cerliani, "A new myeloarchitectonic map of the human neocortex based on data from the Vogt-Vogt school (vol 220, pg 2551, 2015),", *Brain Struct Funct,* vol. 220, no. 6, pp. 3753-3755, Nov 2015, doi: 10.1007/s00429-014-0884-8.

[33] C. Grefkes, S. Geyer, T. Schormann, P. Roland, and K. Zilles, "Human somatosensory area 2: Observer-independent cytoarchitectonic mapping, interindividual variability, and population map,", *Neuroimage,* vol. 14, no. 3, pp. 617-631, Sep 2001, doi: 10.1006/nimg.2001.0858.

[34] N. B. Walters *et al.*, "In vivo identification of human cortical areas using high-resolution MRI: an approach to cerebral structure–function correlation," *Proceedings of the National Academy of Sciences,* vol. 100, no. 5, pp. 2981-2986, 2003.

[35] S. Geyer *et al.*, "Two different areas within the primary motor cortex of man,", *Nature,* vol. 382, no. 6594, pp. 805-807, Aug 29 1996, doi: DOI 10.1038/382805a0.

[36] R. Kawashima *et al.*, "Activity in the human primary motor cortex related to arm and finger movements," *Neuroreport,* vol. 6, no. 2, pp. 238-240, 1995.

[37] K. Amunts, A. Schleicher, U. Burgel, H. Mohlberg, H. B. M. Uylings, and K. Zilles, "Broca's region revisited: Cytoarchitecture and intersubject variability,", *J Comp Neurol,* vol. 412, no. 2, pp. 319-341, Sep 20 1999, doi: Doi 10.1002/(Sici)1096-9861(19990920)412:2<319::Aid-Cne10>3.0.Co;2-7.

[38] K. Amunts, A. Malikovic, H. Mohlberg, T. Schormann, and K. Zilles, "Brodmann's areas 17 and 18 brought into stereotaxic space—where and how variable?," *Neuroimage,* vol. 11, no. 1, pp. 66-84, 2000.

[39] S. Geyer, A. Schleicher, and K. Zilles, "Areas 3a, 3b, and 1 of human primary somatosensory cortex," *Neuroimage,* vol. 10, no. 1, pp. 63-83, Jul 1999, doi: 10.1006/nimg.1999.0440.

[40] S. B. Eickhoff, A. Schleicher, K. Zilles, and K. Amunts, "The human parietal operculum. I. Cytoarchitectonic mapping of subdivisions," *Cerebral cortex,* vol. 16, no. 2, pp. 254-267, 2006.

[41] S. B. Eickhoff *et al.*, "A new SPM toolbox for combining probabilistic cytoarchitectonic maps and functional imaging data,", *Neuroimage,* vol. 25, no. 4, pp. 1325-1335, May 1 2005, doi: 10.1016/j.neuroimage.2004.12.034.

[42] K. Amunts, A. Schleicher, and K. Zilles, "Cytoarchitecture of the cerebral cortex—more than localization," *Neuroimage,* vol. 37, no. 4, pp. 1061-1065, 2007.

[43] K. Amunts and K. Zilles, "Atlases of the human brain: tools for functional neuroimaging," in *Neuroanatomical Tract-Tracing 3*: Springer, 2006, pp. 566-603.

[44] I. L. Pykett *et al.*, "Principles of nuclear magnetic resonance imaging," *Radiology,* vol. 143, no. 1, pp. 157-168, 1982.

[45] E. M. Haacke, R. W. Brown, M. R. Thompson, and R. Venkatesan, *Magnetic resonance imaging: physical principles and sequence design*. Wiley-Liss New York: , 1999.

[46] E. M. Haacke, S. Liu, S. Buch, W. Zheng, D. Wu, and Y. Ye, "Quantitative susceptibility mapping: current status and future directions," *Magn Reson Imaging,* vol. 33, no. 1, pp. 1-25, 2015.

[47] L. J. Edwards, E. Kirilina, S. Mohammadi, and N. Weiskopf, "Microstructural imaging of human neocortex in vivo," *Neuroimage,* vol. 182, pp. 184-206, Nov 15 2018, doi: 10.1016/j.neuroimage.2018.02.055.

[48] B. Fischl and A. M. Dale, "Measuring the thickness of the human cerebral cortex from magnetic resonance images," *Proceedings of the National Academy of Sciences,* vol. 97, no. 20, pp. 11050-11055, 2000.

[49] E. Luders, P. M. Thompson, K. Narr, A. W. Toga, L. Jancke, and C. Gaser, "A curvature-based approach to estimate local gyrification on the cortical surface," *Neuroimage,* vol. 29, no. 4, pp. 1224-1230, 2006.

[50] R. Trampel, P.-L. Bazin, K. Pine, and N. Weiskopf, "In-vivo magnetic resonance imaging (MRI) of laminae in the human cortex," *NeuroImage,* vol. 197, pp. 707-715, 2019.

[51] E. Yacoub, N. Harel, and K. Uğurbil, "High-field fMRI unveils orientation columns in humans," *Proceedings of the National Academy of Sciences,* vol. 105, no. 30, pp. 10607-10612, 2008.

[52] S. Nasr, J. R. Polimeni, and R. B. Tootell, "Interdigitated color-and disparity-selective columns within human visual cortical areas V2 and V3," *Journal of Neuroscience,* vol. 36, no. 6, pp. 1841-1857, 2016.

[53] N. Weiskopf, S. Mohammadi, A. Lutti, and M. F. Callaghan, "Advances in MRI-based computational neuroanatomy: from morphometry to in-vivo histology (vol 28, pg 313, 2015),", *Curr Opin Neurol,* vol. 28, no. 5, pp. 547-547, Oct 2015. [Online]. Available: <Go to ISI>://WOS:000369602500016.

[54] W. Kucharczyk, P. Macdonald, G. Stanisz, and R. M. Henkelman, "Relaxivity and magnetization transfer of white matter lipids at MR imaging: importance of cerebrosides and pH," *Radiology,* vol. 192, no. 2, pp. 521-529, 1994.

[55] S. H. Koenig, "Cholesterol of myelin is the determinant of gray-white contrast in MRI of brain," *Magnetic resonance in medicine,* vol. 20, no. 2, pp. 285-291, 1991.

[56] C. Laule *et al.*, "Magnetic resonance imaging of myelin," *Neurotherapeutics,* vol. 4, no. 3, pp. 460-484, 2007.

[57] S. Wharton and R. Bowtell, "Fiber orientation-dependent white matter contrast in gradient echo MRI," *Proceedings of the National Academy of Sciences,* vol. 109, no. 45, pp. 18559-18564, 2012.

[58] A. Mackay, K. Whittall, J. Adler, D. Li, D. Paty, and D. Graeb, "In vivo visualization of myelin water in brain by magnetic resonance," *Magnetic resonance in medicine,* vol. 31, no. 6, pp. 673-677, 1994.

[59] A. MacKay, C. Laule, I. Vavasour, T. Bjarnason, S. Kolind, and B. Mädler, "Insights into brain microstructure from the T2 distribution," *Magn Reson Imaging,* vol. 24, no. 4, pp. 515-525, 2006.

[60] S. C. Deoni, B. K. Rutt, and T. M. Peters, "Rapid combined T1 and T2 mapping using gradient recalled acquisition in the steady state," *Magnetic Resonance in Medicine: An Official Journal of the International Society for Magnetic Resonance in Medicine,* vol. 49, no. 3, pp. 515-526, 2003.

[61] R. Gil, D. Khabipova, M. Zwiers, T. Hilbert, T. Kober, and J. P. Marques, "An in vivo study of the orientation-dependent and independent components of transverse relaxation rates in white matter," *NMR in Biomedicine,* vol. 29, no. 12, pp. 1780-1790, 2016.

[62] J. Cohen-Adad *et al.*, "T2* mapping and B0 orientation-dependence at 7 T reveal cyto-and myeloarchitecture organization of the human cortex," *Neuroimage,* vol. 60, no. 2, pp. 1006-1014, 2012.

[63] S. T. Govindarajan, J. Cohen-Adad, M. P. Sormani, A. P. Fan, C. Louapre, and C. Mainero, "Reproducibility of T2* mapping in the human cerebral cortex in vivo at 7 tesla MRI," *J Magn Reson Imaging,* vol. 42, no. 2, pp. 290-296, 2015.

[64] M. Cercignani and S. Bouyagoub, "Brain microstructure by multi-modal MRI: Is the whole greater than the sum of its parts?," *Neuroimage,* vol. 182, pp. 117-127, Nov 15 2018, doi: 10.1016/j.neuroimage.2017.10.052.

[65] B. Bipin Mehta *et al.*, "Magnetic resonance fingerprinting: a technical review," *Magn Reson Med,* vol. 81, no. 1, pp. 25-46, Jan 2019, doi: 10.1002/mrm.27403.

[66] A. Panda *et al.*, "Magnetic Resonance Fingerprinting-An Overview," *Curr Opin Biomed Eng,* vol. 3, pp. 56-66, Sep 2017, doi: 10.1016/j.cobme.2017.11.001.

[67] Y. Jiang, D. Ma, N. Seiberlich, V. Gulani, and M. A. Griswold, "MR Fingerprinting Using Fast Imaging with Steady State Precession (FISP) with Spiral Readout,", *Magnetic Resonance in Medicine,* vol. 74, no. 6, pp. 1621-1631, Dec 2015, doi: 10.1002/mrm.25559.

[68] B. Rieger *et al.*, "Time efficient whole-brain coverage with MR Fingerprinting using slice-interleaved echo-planar-imaging,", *Sci Rep-Uk,* vol. 8, Apr 27 2018, doi: ARTN 6667

10.1038/s41598-018-24920-z.

[69] B. Rieger, F. Zimmer, J. Zapp, S. Weingartner, and L. R. Schad, "Magnetic Resonance Fingerprinting Using Echo-Planar Imaging: Joint Quantification of T-1 and T-2* Relaxation Times,", *Magnetic Resonance in Medicine,* vol. 78, no. 5, pp. 1724-1733, Nov 2017, doi: 10.1002/mrm.26561.

[70] Y. Jiang *et al.*, "MR Fingerprinting Using the Quick Echo Splitting NMR Imaging Technique,", *Magnetic Resonance in Medicine,* vol. 77, no. 3, pp. 979-988, Mar 2017, doi: 10.1002/mrm.26173.

[71] M. A. Cloos *et al.*, "Multiparametric imaging with heterogeneous radiofrequency fields,", *Nat Commun,* vol. 7, Aug 2016, doi: ARTN 12445

10.1038/ncomms12445.

[72] M. E. Poorman *et al.*, "Magnetic resonance fingerprinting Part 1: Potential uses, current challenges, and recommendations,", *J Magn Reson Imaging,* Jul 2 2019, doi: 10.1002/jmri.26836.

[73] D. Ma *et al.*, "Fast 3D magnetic resonance fingerprinting for a whole-brain coverage,", *Magnetic Resonance in Medicine,* vol. 79, no. 4, pp. 2190-2197, Apr 2018, doi: 10.1002/mrm.26886.

[74] M. Weigel, "Extended Phase Graphs: Dephasing, RF Pulses, and Echoes - Pure and Simple,", *J Magn Reson Imaging,* vol. 41, no. 2, pp. 266-295, Feb 2015, doi: 10.1002/jmri.24619.

[75] Y. Jiang *et al.*, "Use of Pattern Recognition for Unaliasing Simultaneously Acquired Slices in Simultaneous Multislice MR Fingerprinting,", *Magnetic Resonance in Medicine,* vol. 78, no. 5, pp. 1870-1876, Nov 2017, doi: 10.1002/mrm.26572.

[76] D. Ma *et al.*, "Music-Based Magnetic Resonance Fingerprinting to Improve Patient Comfort During MRI Examinations,", *Magnetic Resonance in Medicine,* vol. 75, no. 6, pp. 2303-2314, Jun 2016, doi: 10.1002/mrm.25818.

[77] R. B. Irene Wang , Mark Griswold, Stephen Jones, Dan Ma, "Exploring human cortical microstructure using magnetic resonance fingerprinting at 3T," in *ISMRM*, Montreal, 2019.

[78] C. R. Wyatt, T. B. Smith, M. K. Sammi, W. D. Rooney, and A. R. Guimaraes, "Multi-parametric T2* magnetic resonance fingerprinting using variable echo times," *NMR in Biomedicine,* vol. 31, no. 9, p. e3951, 2018.

[79] G. Buonincontri and S. J. Sawiak, "MR Fingerprinting with Simultaneous B1 Estimation,", *Magnetic Resonance in Medicine,* vol. 76, no. 4, pp. 1127-1135, Oct 2016, doi: 10.1002/mrm.26009.

[80] T. Christen *et al.*, "MR vascular fingerprinting: A new approach to compute cerebral blood volume, mean vessel radius, and oxygenation maps in the human brain,", *Neuroimage,* vol. 89, pp. 262-270, Apr 1 2014, doi: 10.1016/j.neuroimage.2013.11.052.

[81] B. Lemasson *et al.*, "MR Vascular Fingerprinting in Stroke and Brain Tumors Models,", *Sci Rep-Uk,* vol. 6, Nov 24 2016, doi: ARTN 37071

10.1038/srep37071.

[82] P. Su *et al.*, "Multiparametric Estimation of Brain Hemodynamics With MR Fingerprinting ASL,", *Magnetic Resonance in Medicine,* vol. 78, no. 5, pp. 1812-1823, Nov 2017, doi: 10.1002/mrm.26587.

[83] D. F. McGivney *et al.*, "SVD Compression for Magnetic Resonance Fingerprinting in the Time Domain,", *Ieee T Med Imaging,* vol. 33, no. 12, pp. 2311-2322, Dec 2014, doi: 10.1109/Tmi.2014.2337321.

[84] S. F. Cauley *et al.*, "Fast group matching for MR fingerprinting reconstruction,", *Magnetic Resonance in Medicine,* vol. 74, no. 2, pp. 523-528, Aug 2015, doi: 10.1002/mrm.25439.

[85] M. R. Yang *et al.*, "Low rank approximation methods for MR fingerprinting with large scale dictionaries,", *Magnetic Resonance in Medicine,* vol. 79, no. 4, pp. 2392-2400, Apr 2018, doi: 10.1002/mrm.26867.

[86] C. Badve *et al.*, "Simultaneous T1 and T2 brain relaxometry in asymptomatic volunteers using magnetic resonance fingerprinting," *Tomography,* vol. 1, no. 2, p. 136, 2015.

[87] Y. Chen *et al.*, "MR fingerprinting enables quantitative measures of brain tissue relaxation times and myelin water fraction in the first five years of life,", *Neuroimage,* vol. 186, pp. 782-793, Feb 1 2019, doi: 10.1016/j.neuroimage.2018.11.038.

[88] J. I. Hamilton *et al.*, "MR fingerprinting for rapid quantification of myocardial T1 , T2 , and proton spin density," *Magn Reson Med,* vol. 77, no. 4, pp. 1446-1458, Apr 2017, doi: 10.1002/mrm.26216.

[89] C. Badve *et al.*, "MR Fingerprinting of Adult Brain Tumors: Initial Experience,", *Am J Neuroradiol,* vol. 38, no. 3, pp. 492-499, Mar 2017, doi: 10.3174/ajnr.A5035.

[90] D. Ma *et al.*, "Development of high-resolution 3D MR fingerprinting for detection and characterization of epileptic lesions,", *J Magn Reson Imaging,* vol. 49, no. 5, pp. 1333-1346, May 2019, doi: 10.1002/jmri.26319.

[91] C. Liao *et al.*, "Detection of lesions in mesial temporal lobe epilepsy by using MR fingerprinting," *Radiology,* vol. 288, no. 3, pp. 804-812, 2018.

[92] X. Z. Cao *et al.*, "Robust sliding-window reconstruction for Accelerating the acquisition of MR fingerprinting,", *Magnetic Resonance in Medicine,* vol. 78, no. 4, pp. 1579-1588, Oct 2017, doi: 10.1002/mrm.26521.

[93] A. C. Yu *et al.*, "Development of a Combined MR Fingerprinting and Diffusion Examination for Prostate Cancer,", *Radiology,* vol. 283, no. 3, pp. 728-737, Jun 2017, doi: 10.1148/radiol.2017161599.

[94] Y. Chen *et al.*, "Three-dimensional MR Fingerprinting for Quantitative Breast Imaging,", *Radiology,* vol. 290, no. 1, pp. 33-40, Jan 2019, doi: 10.1148/radiol.2018180836.

[95] Y. C. Liu, J. Hamilton, S. Rajagopalan, and N. Seiberlich, "Cardiac Magnetic Resonance Fingerprinting Technical Overview and Initial Results,", *Jacc-Cardiovasc Imag,* vol. 11, no. 12, pp. 1837-1853, Dec 2018, doi: 10.1016/j.jcmg.2018.08.028.

[96] M. A. Cloos *et al.*, "Rapid Radial T1 and T2 Mapping of the Hip Articular Cartilage With Magnetic Resonance Fingerprinting," *J Magn Reson Imaging,* vol. 50, no. 3, pp. 810-815, Sep 2019, doi: 10.1002/jmri.26615.

[97] Y. Chen *et al.*, "MR Fingerprinting for Rapid Quantitative Abdominal Imaging,", *Radiology,* vol. 279, no. 1, pp. 278-286, Apr 2016, doi: 10.1148/radiol.2016152037.

[98] T. Hastie, R. Tibshirani, J. Friedman, and J. Franklin, "The elements of statistical learning: data mining, inference and prediction," *The Mathematical Intelligencer,* vol. 27, no. 2, pp. 83-85, 2005.

[99] D. Ravi, N. Ghavami, D. C. Alexander, and A. Ianus, "Current Applications and Future Promises of Machine Learning in Diffusion MRI,", *Math Vis,* pp. 105-121, 2019, doi: 10.1007/978-3-030-05831-9_9.

[100] G. L. Nedjati-Gilani *et al.*, "Machine learning based compartment models with permeability for white matter microstructure imaging,", *Neuroimage,* vol. 150, pp. 119-135, Apr 15 2017, doi: 10.1016/j.neuroimage.2017.02.013.

[101] A. Criminisil, J. Shotton, and E. Konukoglu, "Decision Forests: A Unified Framework for Classification, Regression, Density Estimation, Manifold Learning and Semi-Supervised Learning,", *Found Trends Comput,* vol. 7, no. 2-3, pp. 81-227, 2011, doi: 10.1501/0000000035.

[102] M. Reisert, E. Kellner, B. Dhital, J. Hennig, and V. G. Kiselev, "Disentangling micro from mesostructure by diffusion MRI: A Bayesian approach,", *Neuroimage,* vol. 147, pp. 964-975, Feb 15 2017, doi: 10.1016/j.neuroimage.2016.09.058.

[103] K. P. Murphy, "Machine Learning: A Probabilistic Perspective,", *Machine Learning: A Probabilistic Perspective,* pp. 1-1067, 2012. [Online]. Available: <Go to ISI>://WOS:000310531500030.

[104] P. F. Neher, M. A. Cote, J. C. Houde, M. Descoteaux, and K. H. Maier-Hein, "Fiber tractography using machine learning,", *Neuroimage,* vol. 158, pp. 417-429, Sep 2017, doi: 10.1016/j.neuroimage.2017.07.028.

[105] X. Shen, X. Papademetris, and R. T. Constable, "Graph-theory based parcellation of functional subunits in the brain from resting-state fMRI data,", *Neuroimage,* vol. 50, no. 3, pp. 1027-1035, Apr 15 2010, doi: 10.1016/j.neuroimage.2009.12.119.

[106] R. C. Craddock, G. A. James, P. E. Holtzheimer, X. P. P. Hu, and H. S. Mayberg, "A whole brain fMRI atlas generated via spatially constrained spectral clustering,", *Hum Brain Mapp,* vol. 33, no. 8, pp. 1914-1928, Aug 2012, doi: 10.1002/hbm.21333.

[107] M. F. Glasser *et al.*, "A multi-modal parcellation of human cerebral cortex,", *Nature,* vol. 536, no. 7615, pp. 171-+, Aug 11 2016, doi: 10.1038/nature18933.

[108] G. P. Winston, C. Micallef, M. R. Symms, D. C. Alexander, J. S. Duncan, and H. Zhang, "Advanced diffusion imaging sequences could aid assessing patients with

focal cortical dysplasia and epilepsy," *Epilepsy research,* vol. 108, no. 2, pp. 336-339, 2014.

[109] P. Morosan, J. Rademacher, A. Schleicher, K. Amunts, T. Schormann, and K. Zilles, "Human primary auditory cortex: cytoarchitectonic subdivisions and mapping into a spatial reference system," *Neuroimage,* vol. 13, no. 4, pp. 684-701, 2001.

[110] J. Dinse *et al.*, "A cytoarchitecture-driven myelin model reveals area-specific signatures in human primary and secondary areas using ultra-high resolution in-vivo brain MRI,", *Neuroimage,* vol. 114, pp. 71-87, Jul 1 2015, doi: 10.1016/j.neuroimage.2015.04.023.

[111] J. Dinse *et al.*, "A Histology-Based Model of Quantitative T1 Contrast for In-vivo Cortical Parcellation of High-Resolution 7 Tesla Brain MR Images,", *Lect Notes Comput Sc,* vol. 8150, pp. 51-58, 2013. [Online]. Available: <Go to ISI>://WOS:000342835100007.

[112] M. D. Does, "Inferring brain tissue composition and microstructure via MR relaxometry,", *Neuroimage,* vol. 182, pp. 136-148, Nov 15 2018, doi: 10.1016/j.neuroimage.2017.12.087.

[113] S. Geyer, M. Weiss, K. Reimann, G. Lohmann, and R. Turner, "Microstructural parcellation of the human cerebral cortex - from Brodmann's post-mortem map to in vivo mapping with high-field magnetic resonance imaging,", *Front Hum Neurosci,* vol. 5, Feb 18 2011, doi: ARTN 19

10.3389/fnhum.2011.00019.

[114] C. L. Tardif, J. Dinse, A. Schäfer, R. Turner, and P.-L. Bazin, "Multi-modal surface-based alignment of cortical areas using intra-cortical T1 contrast," in *International Workshop on Multimodal Brain Image Analysis*, 2013: Springer, pp. 222-232.

[115] C. Stuber *et al.*, "Myelin and iron concentration in the human brain: A quantitative study of MRI contrast,", *Neuroimage,* vol. 93, pp. 95-106, Jun 2014, doi: 10.1016/j.neuroimage.2014.02.026.

[116] J. P. Marques, D. Khabipova, and R. Gruetter, "Studying cyto and myeloarchitecture of the human cortex at ultra-high field with quantitative imaging: R-1, R-2 and magnetic susceptibility,", *Neuroimage,* vol. 147, pp. 152-163, Feb 15 2017, doi: 10.1016/j.neuroimage.2016.12.009.

[117] G. Mangeat, S. T. Govindarajan, C. Maineroc, and J. Cohen-Adad, "Multivariate combination of magnetization transfer, T-2* and B0 orientation to study the myelo-architecture of the in vivo human cortex,", *Neuroimage,* vol. 119, pp. 89-102, Oct 1 2015, doi: 10.1016/j.neuroimage.2015.06.033.

[118] K. M. Hasan, C. Halphen, M. D. Boska, and P. A. Narayana, "Diffusion tensor metrics, T2 relaxation, and volumetry of the naturally aging human caudate nuclei in healthy young and middle-aged adults: possible implications for the neurobiology of human brain aging and disease," *Magn Reson Med,* vol. 59, no. 1, pp. 7-13, Jan 2008, doi: 10.1002/mrm.21434.

[119] P. de Blank *et al.*, "Magnetic Resonance Fingerprinting to Characterize Childhood and Young Adult Brain Tumors,", *Pediatr Neurosurg,* vol. 54, no. 5, pp. 310-318, Oct 2019, doi: 10.1159/000501696.

[120] I. Wang, R. Boyacioglu, M. A. Griswold, S. Jones, and D. Ma, "Exploring human cortical microstructure using magnetic resonance fingerprinting at 3T," in *ISMRM*, Montreal, 2019, p. 4990.

[121] M. F. Glasser and D. C. Van Essen, "Mapping Human Cortical Areas In Vivo Based on Myelin Content as Revealed by T1- and T2-Weighted MRI,", *Journal of Neuroscience,* vol. 31, no. 32, pp. 11597-11616, Aug 10 2011, doi: 10.1523/Jneurosci.2180-11.2011.

[122] Jülich. "Jülich histological (cyto- and myelo-architectonic) atlas references." https://fsl.fmrib.ox.ac.uk/fsl/fslwiki/Atlases/Juelich (accessed 2017).

[123] S. M. Smith *et al.*, "Advances in functional and structural MR image analysis and implementation as FSL,", *Neuroimage,* vol. 23, pp. S208-S219, 2004, doi: 10.1016/j.neuroimage.2004.07.051.

[124] F. Eggenschwiler, T. Kober, A. W. Magill, R. Gruetter, and J. P. Marques, "SA2RAGE: A new sequence for fast B1+-mapping,", *Magnetic Resonance in Medicine,* vol. 67, no. 6, pp. 1609-1619, Jun 2012, doi: 10.1002/mrm.23145.

[125] J. P. Marques, T. Kober, G. Krueger, W. van der Zwaag, P. F. Van de Moortele, and R. Gruetter, "MP2RAGE, a self bias-field corrected sequence for improved segmentation and T-1-mapping at high field,", *Neuroimage,* vol. 49, no. 2, pp. 1271-1281, Jan 15 2010, doi: 10.1016/j.neuroimage.2009.10.002.

[126] P. Mansfield, "Multi-Planar Image-Formation Using Nmr Spin Echoes,", *J Phys C Solid State,* vol. 10, no. 3, pp. L55-L58, 1977, doi: Doi 10.1088/0022-3719/10/3/004.

[127] M. A. Griswold *et al.*, "Generalized Autocalibrating Partially Parallel Acquisitions (GRAPPA),", *Magnetic Resonance in Medicine,* vol. 47, no. 6, pp. 1202-1210, Jun 2002, doi: 10.1002/mrm.10171.

[128] K. Perlin, "An image synthesizer," *ACM Siggraph Computer Graphics,* vol. 19, no. 3, pp. 287-296, 1985.

[129] S. M. Smith, "Fast robust automated brain extraction,", *Hum Brain Mapp,* vol. 17, no. 3, pp. 143-155, Nov 2002, doi: 10.1002/hbm.10062.

[130] M. Jenkinson, P. Bannister, M. Brady, and S. Smith, "Improved optimization for the robust and accurate linear registration and motion correction of brain images,", *Neuroimage,* vol. 17, no. 2, pp. 825-841, Oct 2002, doi: 10.1006/nimg.2002.1132.

[131] M. Jenkinson and S. Smith, "A global optimisation method for robust affine registration of brain images,", *Med Image Anal,* vol. 5, no. 2, pp. 143-156, Jun 2001, doi: Doi 10.1016/S1361-8415(01)00036-6.

[132] J. L. Andersson, M. Jenkinson, and S. Smith, "Non-linear registration aka Spatial normalisation FMRIB Technial Report TR07JA2," *FMRIB Analysis Group of the University of Oxford,* 2007.

[133] W. D. Penny, K. J. Friston, J. T. Ashburner, S. J. Kiebel, and T. E. Nichols, *Statistical parametric mapping: the analysis of functional brain images*. Elsevier, 2011.

[134] C. Z. Wang and X. S. Wang, "Supporting content-based searches on time series via approximation,", *12th International Conference on Scientific and Statistical Database Management, Proceedings,* pp. 69-81, 2000, doi: Doi 10.1109/Ssdm.2000.869779.

[135] A. Wald and J. Wolfowitz, "On a test whether two samples are from the same population,", *Ann Math Stat,* vol. 11, pp. 147-162, 1940, doi: DOI 10.1214/aoms/1177731909.

[136] R. C. Geary, "Relative Efficiency of Count of Sign Changes for Assessing Residual Autoregression in Least Squares Regression,", *Biometrika,* vol. 57, no. 1, pp. 123-&, 1970, doi: DOI 10.1093/biomet/57.1.123.

[137] M. Hollander, D. A. Wolfe, and E. Chicken, *Nonparametric statistical methods*. John Wiley & Sons, 2013.

[138] S. Geyer, A. Schleicher, and K. Zilles, "The somatosensory cortex of human: Cytoarchitecture and regional distributions of receptor-binding sites,", *Neuroimage,* vol. 6, no. 1, pp. 27-45, Jul 1997, doi: DOI 10.1006/nimg.1997.0271.

[139] A. Hopf, "Registration of the myeloarchitecture of the human frontal lobe with an extinction method," *J Hirnforsch,* vol. 10, no. 3, pp. 259-69, 1968. [Online]. Available: https://www.ncbi.nlm.nih.gov/pubmed/4895364.

[140] A. Hopf, "Photometric studies on the myeloarchitecture of the human parietal lobe. II. Postcentral region," *J Hirnforsch,* vol. 12, no. 1, pp. 135-41, 1970. [Online]. Available: https://www.ncbi.nlm.nih.gov/pubmed/5499693.

[141] W. W. Chen *et al.*, "Intracranial Calcifications and Hemorrhages: Characterization with Quantitative Susceptibility Mapping,", *Radiology,* vol. 270, no. 2, pp. 496-505, Feb 2014, doi: 10.1148/radiol.13122640.

[142] R. Turner, D. Lebihan, J. Maier, R. Vavrek, L. K. Hedges, and J. Pekar, "Echo-Planar Imaging of Intravoxel Incoherent Motion,", *Radiology,* vol. 177, no. 2, pp. 407-414, Nov 1990, doi: DOI 10.1148/radiology.177.2.2217777.

[143] C. F. von Economo, G. N. Koskinas, and L. C. Triarhou, "Atlas of cytoarchitectonics of the adult human cerebral cortex," 2008.

[144] B. A. Poser, P. J. Koopmans, T. Witzel, L. L. Wald, and M. Barth, "Three dimensional echo-planar imaging at 7 Tesla,", *Neuroimage,* vol. 51, no. 1, pp. 261-266, May 15 2010, doi: 10.1016/j.neuroimage.2010.01.108.

[145] P. Jezzard and R. S. Balaban, "Correction for geometric distortion in echo planar images from B0 field variations," *Magn Reson Med,* vol. 34, no. 1, pp. 65-73, Jul 1995, doi: 10.1002/mrm.1910340111.

[146] K. T. Block and J. Frahm, "Spiral imaging: a critical appraisal," *J Magn Reson Imaging,* vol. 21, no. 6, pp. 657-68, Jun 2005, doi: 10.1002/jmri.20320.

[147] T. Amthor, M. Doneva, P. Koken, K. Sommer, J. Meineke, and P. Bornert, "Magnetic Resonance Fingerprinting with short relaxation intervals,", *Magn Reson Imaging,* vol. 41, pp. 22-28, Sep 2017, doi: 10.1016/j.mri.2017.06.014.

[148] M. Barth, F. Breuer, P. J. Koopmans, D. G. Norris, and B. A. Poser, "Simultaneous Multislice (SMS) Imaging Techniques,", *Magnetic Resonance in Medicine,* vol. 75, no. 1, pp. 63-81, Jan 2016, doi: 10.1002/mrm.25897.

[149] H. H. Ye *et al.*, "Simultaneous multislice magnetic resonance fingerprinting (SMS-MRF) with direct-spiral slice-GRAPPA (ds-SG) reconstruction,", *Magnetic Resonance in Medicine,* vol. 77, no. 5, pp. 1966-1974, May 2017, doi: 10.1002/mrm.26271.

[150] B. B. Mehta *et al.*, "Magnetic resonance fingerprinting: a technical review,", *Magnetic Resonance in Medicine,* vol. 81, no. 1, pp. 25-46, Jan 2019, doi: 10.1002/mrm.27403.

[151] C. Y. Liao *et al.*, "3D MR fingerprinting with accelerated stack-of-spirals and hybrid sliding-window and GRAPPA reconstruction,", *Neuroimage,* vol. 162, pp. 13-22, Nov 15 2017, doi: 10.1016/j.neuroimage.2017.08.030.

[152] R. R. Edelman, P. Wielopolski, and F. Schmitt, "Echo-planar MR imaging," *Radiology,* vol. 192, no. 3, pp. 600-12, Sep 1994, doi: 10.1148/radiology.192.3.8058920.

[153] G. Buonincontri, R. F. Schulte, M. Cosottini, and M. Tosetti, "Spiral MR fingerprinting at 7 T with simultaneous B1 estimation,", *Magn Reson Imaging,* vol. 41, pp. 1-6, Sep 2017, doi: 10.1016/j.mri.2017.04.003.

[154] D. Ma *et al.*, "Slice profile and B1 corrections in 2D magnetic resonance fingerprinting," *Magn Reson Med,* vol. 78, no. 5, pp. 1781-1789, Nov 2017, doi: 10.1002/mrm.26580.

[155] FSL. "fsl_anat." https://fsl.fmrib.ox.ac.uk/fsl/fslwiki/fsl_anat (accessed 2019).

[156] H. R. Zeng and R. T. Constable, "Image distortion correction in EPI: Comparison of field mapping with point spread function mapping,", *Magnetic Resonance in Medicine,* vol. 48, no. 1, pp. 137-146, Jul 2002, doi: 10.1002/mrm.10200.

[157] H. Duffau, "Lessons from brain mapping in surgery for low-grade glioma: insights into associations between tumour and brain plasticity," *Lancet Neurol,* vol. 4, no. 8, pp. 476-86, Aug 2005, doi: 10.1016/S1474-4422(05)70140-X.

[158] A. Magara, R. Buhler, D. Moser, M. Kowalski, P. Pourtehrani, and D. Jeanmonod, "First experience with MR-guided focused ultrasound in the treatment of Parkinson's disease," *J Ther Ultrasound,* vol. 2, p. 11, 2014, doi: 10.1186/2050-5736-2-11.

[159] Z. Y. Guo *et al.*, "Compact Design of a Hydraulic Driving Robot for Intraoperative MRI-Guided Bilateral Stereotactic Neurosurgery,", *Ieee Robot Autom Let,* vol. 3, no. 3, pp. 2515-2522, Jul 2018, doi: 10.1109/Lra.2018.2814637.

[160] K. Usman and K. Rajpoot, "Brain tumor classification from multi-modality MRI using wavelets and machine learning,", *Pattern Anal Appl,* vol. 20, no. 3, pp. 871-881, Aug 2017, doi: 10.1007/s10044-017-0597-8.

[161] N. K. Focke *et al.*, "Individual Voxel-Based Subtype Prediction can Differentiate Progressive Supranuclear Palsy from Idiopathic Parkinson Syndrome and Healthy Controls,", *Hum Brain Mapp,* vol. 32, no. 11, pp. 1905-1915, Nov 2011, doi: 10.1002/hbm.21161.

[162] B. Magnin *et al.*, "Support vector machine-based classification of Alzheimer's disease from whole-brain anatomical MRI,", *Neuroradiology,* vol. 51, no. 2, pp. 73-83, Feb 2009, doi: 10.1007/s00234-008-0463-x.

[163] G. Orru, W. Pettersson-Yeo, A. F. Marquand, G. Sartori, and A. Mechelli, "Using Support Vector Machine to identify imaging biomarkers of neurological and psychiatric disease: A critical review,", *Neurosci Biobehav R,* vol. 36, no. 4, pp. 1140-1152, Apr 2012, doi: 10.1016/j.neubiorev.2012.01.004.

[164] M. D. Sacchet, G. Prasad, L. C. Foland-Ross, P. M. Thompson, and I. H. Gotlib, "Support vector machine classification of major depressive disorder using diffusion-weighted neuroimaging and graph theory,", *Front Psychiatry,* vol. 6, Feb 18 2015, doi: ARTN 21

10.3389/fpsyt.2015.00021.

[165] G. Cucurull *et al.*, "Convolutional neural networks for mesh-based parcellation of the cerebral cortex," 2018.

[166] J. Weston and C. Watkins, "Multi-class support vector machines," Citeseer, 1998.

[167] A. Géron, *Hands-On Machine Learning with Scikit-Learn, Keras, and TensorFlow: Concepts, Tools, and Techniques to Build Intelligent Systems*. O'Reilly Media, 2019.

[168] A. Meyer-Baese and V. J. Schmid, *Pattern recognition and signal analysis in medical imaging*. Elsevier, 2014.

[169] F. Pedregosa *et al.*, "Scikit-learn: Machine Learning in Python,", *J Mach Learn Res,* vol. 12, pp. 2825-2830, Oct 2011. [Online]. Available: <Go to ISI>://WOS:000298103200003.

[170] B. E. Boser, I. M. Guyon, and V. N. Vapnik, "A training algorithm for optimal margin classifiers," in *Proceedings of the fifth annual workshop on Computational learning theory*, 1992: ACM, pp. 144-152.

[171] B. Yekkehkhany, A. Safari, S. Homayouni, and M. Hasanlou, "A comparison study of different kernel functions for SVM-based classification of multi-temporal polarimetry SAR data," *The International Archives of Photogrammetry, Remote Sensing and Spatial Information Sciences,* vol. 40, no. 2, p. 281, 2014.

[172] L. Breiman, "Random forests,", *Mach Learn,* vol. 45, no. 1, pp. 5-32, Oct 2001, doi: Doi 10.1023/A:1010933404324.

[173] J. Han, M. Kamber, and J. Pei, "Data Mining: Concepts and Techniques, 3rd Edition,", *Mor Kauf D,* pp. 1-703, 2012. [Online]. Available: <Go to ISI>://WOS:000317122900017.

[174] P. Cunningham and S. J. Delany, "k-Nearest neighbour classifiers," *Multiple Classifier Systems,* vol. 34, no. 8, pp. 1-17, 2007.

[175] T. Cover and P. Hart, "Nearest neighbor pattern classification," *IEEE transactions on information theory,* vol. 13, no. 1, pp. 21-27, 1967.

[176] S. Kaufman, S. Rosset, C. Perlich, and O. Stitelman, "Leakage in Data Mining: Formulation, Detection, and Avoidance,", *Acm T Knowl Discov D,* vol. 6, no. 4, Dec 2012, doi: Artn 15

10.1145/2382577.2382579.

[177] A. K. Jain, R. P. W. Duin, and J. Mao, "Statistical pattern recognition: A review," *IEEE Transactions on pattern analysis and machine intelligence,* vol. 22, no. 1, pp. 4-37, 2000.

[178] J. Goldberger, G. E. Hinton, S. T. Roweis, and R. R. Salakhutdinov, "Neighbourhood components analysis," in *Advances in neural information processing systems*, 2005, pp. 513-520.

[179] S. Raghu and N. Sriraam, "Classification of focal and non-focal EEG signals using neighborhood component analysis and machine learning algorithms,", *Expert Syst Appl,* vol. 113, pp. 18-32, Dec 15 2018, doi: 10.1016/j.eswa.2018.06.031.

[180] G. E. Batista, R. C. Prati, and M. C. Monard, "A study of the behavior of several methods for balancing machine learning training data," *ACM SIGKDD explorations newsletter,* vol. 6, no. 1, pp. 20-29, 2004.

[181] C.-W. Hsu, C.-C. Chang, and C.-J. Lin, "A practical guide to support vector classification," 2003.

[182] A. P. Bradley, "The use of the area under the roc curve in the evaluation of machine learning algorithms,", *Pattern Recogn,* vol. 30, no. 7, pp. 1145-1159, Jul 1997, doi: Doi 10.1016/S0031-3203(96)00142-2.

[183] Y. C. Tang, Y. Q. Zhang, N. V. Chawla, and S. Krasser, "SVMs Modeling for Highly Imbalanced Classification,", *Ieee T Syst Man Cy B,* vol. 39, no. 1, pp. 281-288, Feb 2009, doi: 10.1109/Tsmcb.2008.2002909.

[184] F. J. Provost and T. Fawcett, "Analysis and visualization of classifier performance: Comparison under imprecise class and cost distributions," in *KDD*, 1997, vol. 97, pp. 43-48.

[185] T.-T. Wong, "Performance evaluation of classification algorithms by k-fold and leave-one-out cross validation," *Pattern Recogn,* vol. 48, no. 9, pp. 2839-2846, 2015.

[186] A. Schaefer *et al.*, "Local-Global Parcellation of the Human Cerebral Cortex from Intrinsic Functional Connectivity MRI," *Cereb Cortex,* vol. 28, no. 9, pp. 3095-3114, Sep 1 2018, doi: 10.1093/cercor/bhx179.

[187] X. Z. Wang, K. Smith, and R. Hyndman, "Characteristic-based clustering for time series data,", *Data Min Knowl Disc,* vol. 13, no. 3, pp. 335-364, Nov 2006, doi: 10.1007/s10618-005-0039-x.

[188] M. Langkvist, L. Karlsson, and A. Loutfi, "A review of unsupervised feature learning and deep learning for time-series modeling,", *Pattern Recogn Lett,* vol. 42, pp. 11-24, Jun 1 2014, doi: 10.1016/j.patrec.2014.01.008.

Appendix A

Shahrzad Moeiniyan Bagheri, Viktor Vegh, David Reutens, “Towards in-vivo voxel-wise parcellation of human brain cortex”. *International Society for Magnetic Resonance in Medicine (ISMRM)*, Montreal, Canada, 2019.

The content of this appendix was presented in the poster session for the International Society for Magnetic Resonance in Medicine (ISMRM) 2019 (Montreal, Canada) meeting.

I have made a substantive contribution to the authorship of the abstract:

- Conception and design of the project.
- Analysis and interpretation of the data on which the abstract is based.
- Drafting significant parts of the abstract and critically reviewing it so as to contribute to the interpretation.

As the first author, I have participated in conceptualisation, experiment design, MR sequence development and testing, implementation of the data analysis scripts, implementation of the machine learning algorithms and techniques, data acquisition, data analysis and interpretation.

A note to the reader:

In this appendix I present the proposed method for performing an automated voxel-wise parcellation of the cerebral cortex (as detailed in Chapter 4). The content of this appendix, however, contains the above ISMRM abstract that I presented in Montreal (May 2019). The data for this conference abstract is from the 2D single-slice EPI-MRF acquisitions (as detailed in Chapter 2). Note that in contrast to the data used in this appendix, the data used in Chapter 4 is from the 3D volumetric EPI-MRF acquisitions (detailed in Chapter 3).

A.1 SYNOPSIS

The research aims to establish the feasibility of developing an automated method for *in vivo* voxel-wise parcellation of the human brain cortex. We combined our previously proposed residual analysis Magnetic Resonance Fingerprinting (MRF) approach with supervised classification. We show that extraction of a feature vector from a patch of voxels about a voxel of interest improves the overall prediction accuracy by about 6%, as measured using the Area Under the Curve (AUC) metric. The patch-based analysis leads to 10% increase in the prediction accuracy rate for the primary somatosensory cortex (BA2), suggesting that this approach could be especially advantageous for increasing the parcellation accuracy for areas with interindividual microstructural variability.

A.2 INTRODUCTION

The importance of developing accurate anatomical maps of the human brain has been highlighted in a multitude of studies. Such maps can have significant impact in, for example, neurosurgical decision-making processes [1, 2]. Despite this critical need, a method has not been developed to date which works with MRI human brain *in vivo* data. Here, we further develop our previous work [3] on using Magnetic Resonance Fingerprinting (MRF) [4] for distinguishing microstructural variations between different cortical areas, with the goal of voxel-level classification of the human brain cortex.

A.3 METHODS

We acquired data from 6 healthy participants using a 7T whole-body MRI research scanner (Siemens Healthcare, Erlangen, Germany), as described previously [3]. We applied the following classification methods: K-Nearest Neighbours (KNN), Linear Support Vector

Machine (L-SVM), Radial Basis Function kernel SVM (RBF-SVM) and Random Forests (RF). We opted to classify the following cortical areas: BA2 (primary somatosensory cortex), BA4 (primary motor cortex) and BA6 (premotor cortex). We used the Area Under the Curve (AUC) metric to evaluate model performance instead of accuracy, since the latter can misrepresent when dealing with unbalanced training sets [5].

We have previously shown the autocorrelation values of the residual MRF signals to be able to differentiate the microstructural differences between three cortical areas: BA2, BA4 and BA6 [3]. To calculate autocorrelations, we normalised the residual MRF signals, resulting in normalised autocorrelations (ranging between -1 and +1). Using this notion, we formed feature vectors for voxels of 1000 MRF repetitions (1000 feature vector elements for each voxel, each element being the autocorrelation of the residual signal at a specific lag number).

The importance of selecting and extracting a proper feature set has been studied in a variety of machine learning applications [6]. To satisfy this need, we implemented two different approaches. Firstly, we simply extracted the features (i.e. autocorrelation of the residual signal) associated with a single voxel under consideration as a sample in the training set. Secondly, we investigated the additional use of a patch of surrounding voxels (3x3 voxels) and, a feature vector for a voxel was generated by sequential concatenation of the first 500 autocorrelations from the voxel neighbourhood and the voxel itself.

Through a feature selection process, we subsequently reduced the number of features to the set that showed the highest contribution towards improving the classifier's performance. We then performed model selection, as we also did for the single voxel approach, using 5-fold cross-validation method and by considering AUC as the evaluation score. We should note that class labels for all samples have been derived from the binary masks of the three cortical areas available in the Juelich histological atlas of the human brain [7, 8], after transformation from the MNI space [9] to the native MRF space.

A.4 RESULTS AND DISCUSSION

Fig. Appx.A. 1 provides the single-voxel feature selection and model selection results. RBF-SVM was found to perform best, with average AUC=0.76 (regularisation parameter C=118, kernel width parameter gamma=0.3). For all models the autocorrelations beyond 500 lags do not provide marked improvements in performance, suggesting that the first 500 lags might have the highest influence. This number of autocorrelation lags is taken from all

neighbourhood voxels of the target voxel in the patch-based analysis to form a feature vector of length 4500 (9 × 500).

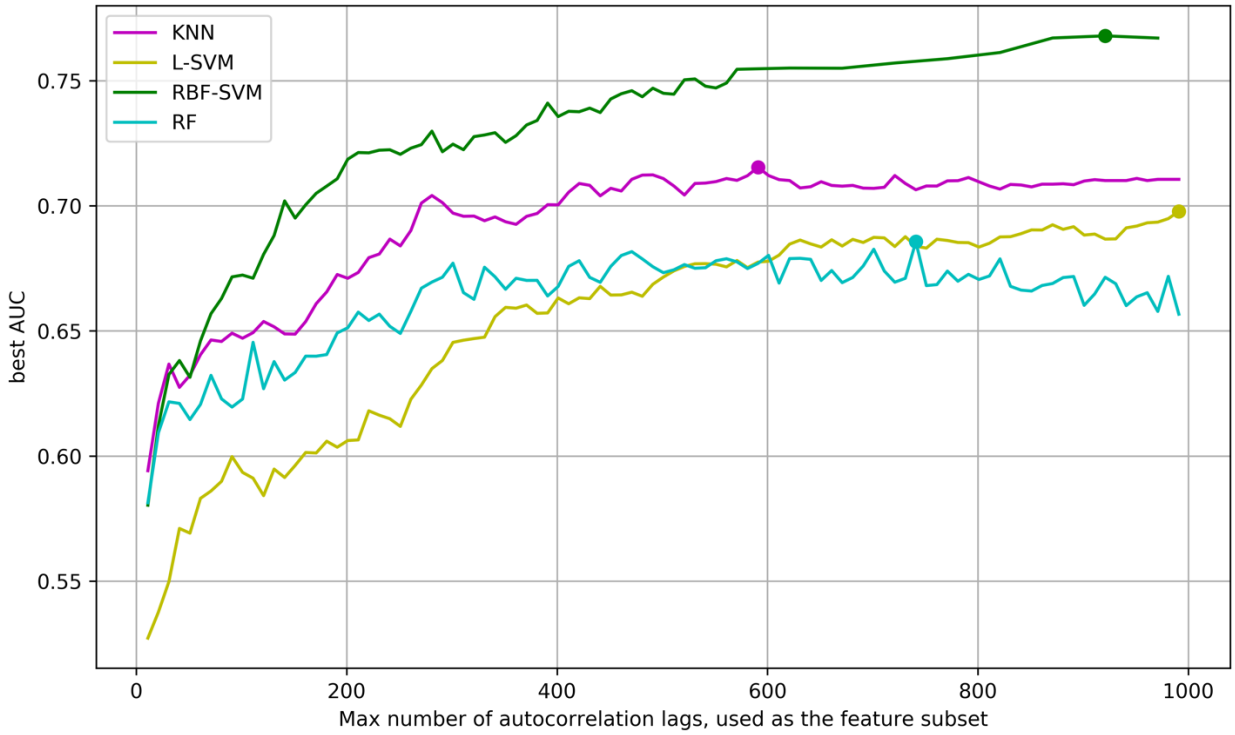

Fig. Appx.A. 1 The best AUC scores of four supervised classification algorithms are compared when trained with different subset of autocorrelation values as feature vectors using the four classification methods: KNN, L-SVM, RBF-SVM and RF. The solid circle on each plot represents the subset of autocorrelations at which that model showed its best performance.

The patch-based results are provided in Table. Appx.A. 1, where the RBF-SVM model outperformed all other models investigated in this study (AUC=0.81; regularisation parameter C=28 and kernel width γ =0.1).

Table. Appx.A. 1 The AUC of the three supervised classification methods using the patch approach.

Classification algorithm	Best AUC	Best performer parameters
KNN	0.76	k-neighbours = 3
RF	0.72	max_features = 118 n-estimators = 10
RBF-SVM	**0.81**	C = 28 γ = 0.1

Confusion matrices for the RBF-SVM approach are provided in Fig. Appx.A. 2 for single-voxel and patch-based feature selection.

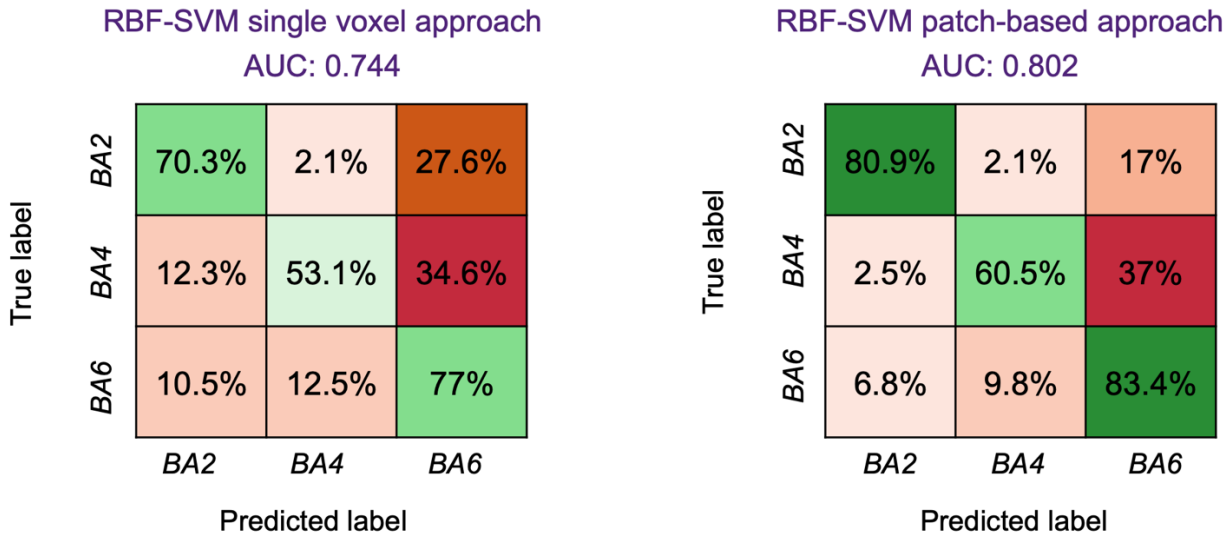

Fig. Appx.A. 2 Confusion matrices for RBF-SVM with patch features (on the right) and the single voxel features (on the left). The AUC score of each classifier is stated at the top.

We found the TPR (True Positive Rate) of predictions (indicated by green) to improve by using patch features (e.g. BA2 increase to 80.9% from 70.3%). This finding is particularly important, as BA2 has higher interindividual microarchitectonic variability than the other two areas, which makes accurate parcellation of this area challenging [10].

Additionally, the FPR (False Positive Rate) for each area (indicated by non-green) is consistent with the microstructural similarity and dissimilarity of these areas established using other microstructural mapping studies [11, 12]. For example, for the case when the true class is BA4, the FPR for BA6 is much larger than for BA2, which suggests that BA4 is microarchitectonically more similar to BA6 than to BA2.

To further validate our approach, we tested the patch-based RBF-SVM classifier on a new set of samples (i.e. unseen by the classifier during the training) from MRF images of a participant. Fig. Appx.A. 3 depicts the distribution of the predicted class labels versus the true class labels (i.e. extracted from the Juelich histological brain atlas).

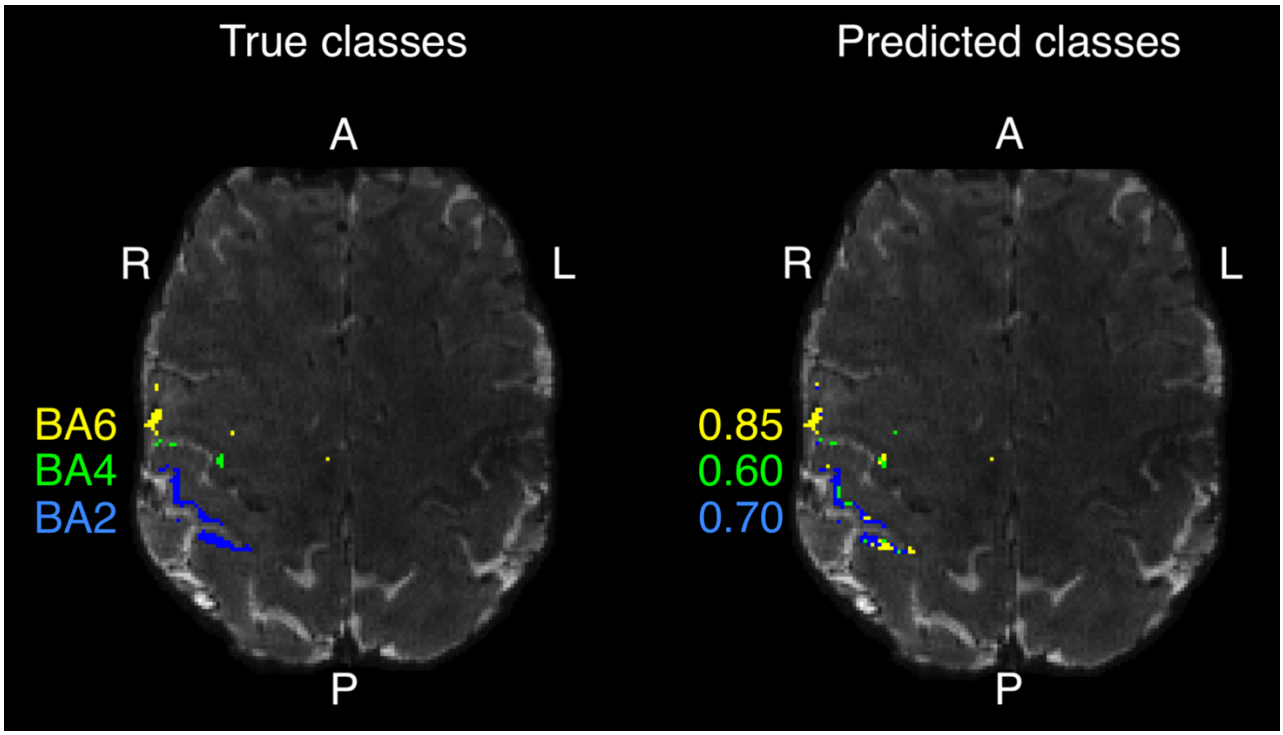

Fig. Appx.A. 3 Using RBF-SVM and the patch approach, the voxels from one slice of a MRF scan (this participant was excluded from the training) are classified into BA2 (blue), BA4 (green) and BA6 (yellow). The TPR of predictions for each class are represented by the same colours as their class labels. On the left, the true classes extracted from the Juelich histological brain atlas are provided for reference.

A.5 CONCLUSIONS

We showed the feasibility of developing a machine learning classification approach based on residual MRF signals for the purpose of automatic voxel-wise parcellation of the human brain cortex *in vivo*. We found features based on a patch of voxels led to higher prediction accuracy in comparison to a single voxel approach.

A.6 WORKS CITED

Chawla, N., Japkowicz, N., & Kotcz, A. (2004). Special issue on learning from imbalanced data sets. ACM Sigkdd Explorations Newsletter, 6(1), 1-6.

Cohen-Adad, J., Polimeni, J. R., Helmer, K. G., Benner, T., McNab, J. A., Wald, L. L., . . . Mainero, C. (2012). T2* mapping and B0 orientation-dependence at 7T reveal cyto-and myeloarchitecture organization of the human cortex. Neuroimage, 60(2), 1006--1014.

Duffau, H. (2005). Lessons from brain mapping in surgery for low-grade glioma: insights into associations between tumour and brain plasticity. The Lancet Neurology, 4(8), 476-486.

Eickhoff, S. B., Stephan, K. E., Mohlberg, H., Grefkes, C., Fink, G. R., Amunts, K., & Zilles, K. (2005). A new SPM toolbox for combining probabilistic cytoarchitectonic maps and functional imaging data. Neuroimage, 25(4), 1325--1335.

Grefkes, C., Geyer, S., Schormann, T., Roland, P., & Zilles, K. (2001). Human somatosensory area 2: observer-independent cytoarchitectonic mapping, interindividual variability, and population map. Neuroimage, 14(3), 617--631.

Guillery, R. (2000). Brodmann's ‘Localisation in the Cerebral Cortex. Journal of Anatomy, 196(3), 493-496.

Guyon, I., & Elisseeff, A. (2003). An introduction to variable and feature selection. Journal of machine learning research, 3(Mar), 1157-1182.

Juelich. (2012, August). Jülich histological (cyto- and myelo-architectonic) atlas references. (M. Webster, Ed.) Retrieved from FSL Atlases/Juelich: https://fsl.fmrib.ox.ac.uk/fsl/fslwiki/Atlases/Juelich

Ma, D., Gulani, V., Seiberlich, N., Liu, K., Sunshine, J., Duerk, J., & Griswold, M. (2013). Magnetic resonance fingerprinting. Nature, 495(7440), 187--192.

Magara, A., Buhler, R., Moser, D., Kowalski, M., Pourtehrani, P., & Jeanmonod, D. (2014). First experience with MR-guided focused ultrasound in the treatment of Parkinson's disease. Journal of therapeutic ultrasound, 2(1), 11.

Mazziotta, J., Toga, A., Evans, A., Fox, P., Lancaster, J., Zilles, K., . . . Pike, B. (2001). A four-dimensional probabilistic atlas of the human brain. Journal of the American Medical Informatics Association, 8(5), 401-430.

Moeiniyan Bagheri, S., Vegh, V., & Reutens, D. (2018). Magnetic Resonance Fingerprinting (MRF) can reveal microstructural variations in the brain gray matter. ISMRM. Paris.

Appendix B

THE UNIVERSITY OF QUEENSLAND

Institutional Human Research Ethics Approval

Project Title:	Development of novel MRI sequences and testing of new MRI hardware on healthy control subjects, plus Quality Assurance of existing sequences and hardware – 30/01/2019 AMENDMENT
Chief Investigator:	Professor David Reutens
Supervisor:	None
Co-Investigator(s):	Professor Graham Galloway, Dr Gary Cowin, A/Prof Markus Barth, Ms Gail Durbridge, Mrs Nicole Atcheson, Mr Aiman Al-Najjar
School(s):	Centre for Advanced Imaging, The University of Queensland
Approval Number:	2005000502
Granting Agency/Degree:	None
Duration:	31 December 2020

Comments/Conditions:

Amendment 30/01/2019

- Remove Investigators: Dr Katie McMahon, Dr Daniel Staeb, Dr Jin Jin
- Extend the duration of the project to 31 December 2020
- Amendment form 2005000502 - CAI

Note: if this approval is for amendments to an already approved protocol for which a UQ Clinical Trials Protection/Insurance Form was originally submitted, then the researchers must directly notify the UQ Insurance Office of any changes to that Form and Participant Information Sheets & Consent Forms as a result of the amendments, before action.

Name of responsible Sub-Committee:
University of Queensland Medicine, Low & Negligible Risk Ethics Sub-Committee
This project complies with the provisions contained in the *National Statement on Ethical Conduct in Human Research* and complies with the regulations governing experimentation on humans.

Name of Ethics Sub-Committee representative:
Associate Professor Diann Eley
Chairperson
University of Queensland Medicine, Low & Negligible Risk Ethics Sub-Committee

Signature 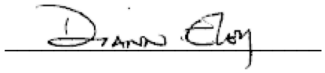 Date **04/02/2019**